UNIVERSITA' DELLA CALABRIA
Dipartimento di FISICA

Scuola di Dottorato ARCHIMEDE

Indirizzo: Scienze e Tecnologie dei Sistemi Complessi

CICLO XXVIII

Study of the electronic and structural properties of tin dioxide and armchair graphene nanoribbons

Settore Scientifico Disciplinare: MAT/07

Direttore: Ch.mo Prof. Pietro Pantano
Firma Pietro Pantano

Supervisori: Ch.mo Prof. Manuela Carini
Firma Manuela Carini

Ch.mo Prof. Arvids Stashans
Firma

Dottorando: Dott. Luis Miguel Villamagua Conza
Firma

Study of the electronic and structural properties of tin dioxide and armchair graphene nanoribbons

Luis Miguel Villamagua Conza, Ph.D.

University of Calabria, 2015

Supervisors: Dr. Manuela Carini
Dr. Arvids Stashans

Abstract:

This dissertation is focused on the study of the electrical and structural properties of two emerging materials, the tin dioxide (SnO_2) and graphene, which have attracted the interest of the semiconductor-device community due to their extraordinary characteristics.

The SnO_2 has been studied by means of *ab initio* simulations (Vienna *ab* initio Simulation Package, VASP). Both n-type and p-type conductivities were investigated. The intrinsic n-type conductivity has been achieved through two schemes: the first one through the combination of oxygen deficiencies and interstitial atoms inside the SnO_2 lattice, whereas in the second one, through the combination of interstitial and/or substitutional hydrogen atoms inside the SnO_2 lattice. On the other hand, the p-type conductivity was achieved by codoping n-type SnO_2 (from earlier configurations) with low concentrations of nitrogen and aluminum impurities. The performed theoretical studies, to a good extent, agree with the experimental results provided by our collaboration group at the National Central University, Jhong-Li (Taiwan). In prospective, these results confirmed that SnO_2 is a promising candidate to replace indium in transparent conductive oxides (TCOs) used in photovoltaic, thin-film transistor, and transparent electronic applications.

The theoretical study of graphene has been conducted by means of a *tight-binding* approach (Atomistic ToolKit simulation package, ATK): the electrical and structural properties of edge-defected armchair graphene nanoribbons (AGNRs) were studied. It was found that Stone-Wales defect (very common in carbon allotropes) placed at the edges of the AGNRs can spark an extra opening of the energy gap in graphene, in addition to that obtained through the quantum confinement of electrons. Moreover, an experimental study on the electrical properties of graphene was carried out at the Tyndall National Institute (Ireland) to understand the influence of multiple cleaning treatments on graphene field-effect transistor (GFET) devices. Debris from residual polymers that appeared during device fabrication was swept off the graphene surface without significantly degrading the electronic properties of the graphene flake. The results suggest that the unusual but extraordinary properties of these graphene allotropes can be considered as a very innovative booster for semiconductor devices, allowing the improvement of the scaling trend beyond that obtained with conventional materials.

Studio delle proprieta elettroniche e strutturali del diossido di stagno e nanostrisce di grafene di tipo armchair

Luis Miguel Villamagua Conza, Ph.D.

Universitá della Calabria, 2015

Relatori: Dr. Manuela Carini
Dr. Arvids Stashans

Riassunto:

Questa tesi si focalizza sullo studio delle proprietà elettriche e strutturali di due materiali emergenti: il diossido di stagno (SnO_2) e il grafene, che hanno attratto l'interesse dei ricercatori nel campo dei dispositivi a semiconduttore grazie alle loro caratteristiche straordinarie.

Il diossido di stagno è stato studiato per mezzo di simulazioni basate su metodi *ab initio* (software: Vienna ab initio Simulation Package, VASP). Entrambe le conduttività di tipo "n" e "p" sono state indagate. La conduttività di tipo "n" è stata ottenuta attraverso due soluzioni: sia attraverso la combinazione di lacune di ossigeno e atomi interstiziali nella rete cristallina di SnO_2, sia attraverso la combinazione di atomi di idrogeno interstiziali e/o sostitutivi nella rete cristallina di SnO_2. D'altra parte, la conduttività di tipo "p" è stata ottenuta attraverso il drogaggio a bassa concentrazione con impurità di azoto e alluminio dei campioni di SnO_2 precedentemente drogato di tipo "n". Gli studi teorici effettuati sono stati in grado di prevedere a grandi linee i risultati sperimentali forniti dal gruppo della National Central University, Jhong-Li (Taiwan), con cui si è collaborato. In prospettiva, questi risultati confermano che il diossido di stagno è un candidato molto promettente per rimpiazzare l'indio in ossidi conduttivi trasparenti (transparent conductive oxides o TCO in inglese) usati per applicazioni di fotovoltaico, transistori a film sottili, ed applicazioni di elettronica trasparente.

Lo studio teorico sul grafene è stato condotto per mezzo del metodo *tight-binding* (software: Atomistic Toolkit, ATK): sono state studiate le proprietà elettriche, strutturali e di trasporto di nanostrisce del tipo *armchair* (armchair graphene nanoribbons o AGNR in inglese). Si è trovato che i difetti Stone-Wales (molto comuni negli allotropi del carbonio) posti ai bordi delle AGNR possono generare un aumento ulteriore della banda energetica proibita del grafene, in aggiunta a quanto ottenibile tramite il confinamento quantistico degli elettroni. Inoltre, uno studio sperimentale sulle proprietà elettriche del grafene è stato effettuato presso l'Istituto Nazionale Tyndall (in Irlanda) per comprendere l'influenza di molteplici trattamenti di pulizia su dispositivi GFT (graphene field effect transistors in inglese). I detriti da polimeri residui, apparsi durante la fabbricazione del dispositivo, sono stati spazzati via dalla superficie di grafene senza degradare significativamente le proprietà elettroniche del fiocco. Questi risultati suggeriscono che le caratteristiche atipiche ma straordinarie di questi allotropi del grafene possono sovralimentare le prestazioni dei dispositivi a semiconduttore, estendendo i miglioramenti legati alla miniaturizzazione delle dimensioni dei dispositivi elettronici al di là di quelli ottenibili con i materiali convenzionali.

Acknowledgements

Writing this dissertation has been fascinating and extremely rewarding. I would like to thank a number of people who have contributed to the final result in many different ways:

First and foremost, I would like to express my special appreciation and thanks to my advisors, Dr. Manuela Carini and Dr. Felice Crupi, at the University of Calabria (Italy) for giving me the opportunity to discover the beauty of research during these three years. Without their vision, technical guidance, patience, and willingness to let me pursue this work, this dissertation would not have been possible.

Special thanks go to Dr. Arvids Stashans at the Technical University of Loja (Ecuador) and Dr. Aidan Quinn at the Tyndall National Institute (Ireland) for allowing me to do my internship and work placement in the groups they lead, “Fisicoquímica de materiales” and “Nanotechnology”, respectively. I greatly appreciated their contributions in time, ideas, funding and feedback on my work.

I am also grateful to all of the staff, students and interns in the groups to which I belonged during my Ph.D. pursuit. In particular, to Leonardo Renteria, Leticia Vaca, Luana Gammetta, Patrizia Notaro, Mara Vigna, Natalia Altomari, Francesco Chiaravalloti, Sebastiano Strangio, Frank Maldonado, Richard Rivera, Freddy Marcillo, Roxane Puicervert, and Daniel Lordan. Many thanks for the time you shared with me at work, and also for supporting me during difficult personal situations.

Special thanks go to Vena Pearl Boñgolan at the University of Philippines (Philippines), and Mark Lans at Radio Esperanza (Ecuador) for their helpful corrections and insightful suggestions made on this manuscript.

Last but not least, I am, and ever will be indebted to my family. Only God knows where I’d be without them. With no right to expect such support, I am deeply appreciative of their continued encouragement. ¡Un millón de gracias!

To all here mentioned, and all that I may have forgotten:

Thanks, Grazie, Gracias, **Yupaychani**, Go raibh maith agat, Salamat.

Luis Miguel Villamagua Conza

“The first obligation of all human beings is to be happy. The second obligation is to make others happy.”

Cantinflas

Dedication

I dedicate this dissertation to God, my parents, brothers and sisters (Maritza, Norman, Lorena, Vanesa, and Wilmer), and to my nephews and nieces (Maria, Jorge, Santiago, Ana, Antonio, Santiago, Ariana, Fernando and the ones on the way).

I realized that by having you by my side, I have always had everything one person needs to be happy and successful in life. Thank you for the encouragement and support that you provided me with in my Ph.D. pursuit.

I love you all dearly

Table of Contents

Abstract: ii

Riassunto: iv

Acknowledgements vi

Dedication ix

Table of Contents x

List of abbreviations xii

List of symbols xiv

Chapter 1. **Introduction** 1

- 1.1. Motivation 1
- 1.2. Scope of the dissertation 3
- 1.3. Dissertation outline 3

Chapter 2: Basics of SnO_2 5

- 2.1. Introduction 5
- 2.2. Crystalline lattice 6
- 2.3. Band structure and density of states 7
- 2.4. Electrical properties 9
- 2.5. Parametrization of SnO_2 into VASP 12

Chapter 3. Basics of carbon allotropes 14

- 3.1. Introduction 14
- 3.2. The direct and reciprocal lattice 15
- 3.3. Tight-binding description of graphene 16
- 3.4. Carbon allotropes 19
- 3.5. Graphene nanoribbons 20
- 3.6. Parametrization of the AGNRs into Atomistic Toolkit 22

Chapter 4. Discussion of results 24

- 4.1. Introduction 24
- 4.2. Origin of the intrinsic n-type conductivity in SnO_2 25
  - 4.2.1. First scheme to achieve n-type conductivity in SnO_2 25
  - 4.2.2. Second scheme to achieve n-type conductivity in SnO_2 29
- 4.3. Transition of the conductivity in SnO_2 from n-type to p-type 34
- 4.4. Electronic properties of defected AGNRs 42

4.5. The influence of multiple cleaning treatments on CVD transferred GFET devices 45
Chapter 5. Summary and conclusions 52
5.1. Summary 52
5.2. Conclusions for SnO_2 54
5.3. Conclusions for graphene and AGNRs 54
References 56
Appendices 70
Appendix A: POSCAR files 71
Appendix B: Fabrication of GFET devices 80
Appendix C: Publications in journals 83
Appendix D: Conference talks 83
Appendix E: Conferences attended 83
Appendix F: Summer schools attended 83
Appendix G: Internships and placements 84

List of abbreviations

AFM	Atomic force microscopy
AGNR	Armchair graphene nanoribbon
BZ	Brillouin zone
CB	Conduction band
CMOS	Complementary metal oxide semiconductor
CNT	Carbon nanotubes
CVD	Chemical vapor deposition
DFT	Density functional theory
DI	Deionized
DOS	Density of states
FET	Field effect transistor
FLG	Few layers graphene
FPD	Flat-panel displays
FTO	Fluorine-doped SnO_2
FWHM	Full-width-at-half-maximum
GNR	Graphene nanoribbons
GGA	General gradient approximation
HOMO	Highest occupied molecular orbital
IR	Infrared
ITO	Indium tin oxide
ITRS	International technology roadmaps for semiconductor
I-V	Current-Voltage
LCD	Liquid-crystal display
LED	Light-emitting diode
LUMO	Lowest unoccupied molecular orbital
NP	Neutrality point
OAA	Optically active area
OLED	Organic light-emitting diode
OPV	Organic photovoltaic
PDOS	Partial density of states
PV	Photovoltaics
QCE	Quantum confinement effect

QED	Quantum electrodynamics
QHE	Quantum Hall effect
RMS	Root-mean-squared
S-W	Stone-Wales defect
TB	Tight-binding
TCO	Transparent conductive oxide
TCE	Transparent conductive electrode
TFT	Thin-film transistor
UV	Ultraviolet
VB	Valence band
ZGNR	Zigzag graphene nanoribbon
0-D	Zero dimensional
1-D	One dimensional
2-D	Two dimensional
2DEG	2D electron gas
3-D	Three dimensional
XRX	X-ray Diffraction
XPS	X-ray photoelectron spectroscopy

List of symbols

Al	Aluminum
cm	Centimeter
cm^3	Cubic centimeter
C	Carbon
°C	Centigrade
eV	Electron-volt
E	Electric field
E_F	Fermi level
E_g	Band gap
F	Fluorine
J	Current density
H	Hydrogen/Hamiltonian operator
H_i	Interstitial hydrogen
H_{sub}	Substitutional hydrogen
I_d	Drain current
I_{OFF}	Off-state current or leakage current
I_{ON}	On-state current or drive current
K	Boltzmann constant
m	Meter
mm	Millimetre
n	Free electron concentration/electron carrier density
N	Nitrogen
N_a	Number of dimer lines of an AGNR
nm	Nano-meter
p	Free hole concentration
R_s	Sheet resistance
Sn	Tin atom
Sn_i	Interstitial Sn atom
SnO_2	Tin dioxide
TiO_2	Titanium dioxide
O	Oxygen
s	Second

Sn_i	Tin interstitial
V_o	Oxygen vacancy
ZnO	Zin oxide
Ω	Ohm
σ	Electrical conductivity
Å	Armstrong
ρ	Electrical resistivity
τ	Mean free path
T	Temperature
μ	Carrier mobility
w	Graphene nanoribbon’s width

Chapter 1. Introduction

1.1. Motivation

Materials that possess both optical transparency and good electrical conductivity (Villamagua, Stashans et al. 2015) form the basis of numerous important applications in contemporary and emerging technologies (Hoel, Mason et al. 2010, Stadler 2012). To name a few, photovoltaics (PV), flat-panel display (FPD), thin-film transistor (TFT) and light-emitting diode (LED) applications in energy and information technologies (Hoel, Mason et al. 2010, Ellmer 2012). This peculiar form of conductivity is usually possible in *4d* metal oxides (SnO_2, In_2O_3, CdO (Facchetti and Marks 2010)) which are widely known as transparent conductive oxides (TCOs) (Minami 2005, Minami 2008).

In particular, Sn-doped In_2O_3 thin films [$In_{2-x}Sn_xO_3$:ITOs] and some of their mixtures have proven to perform better than the other TCOs (Hoel, Mason et al. 2010, Ellmer 2012), exhibiting transparency of greater than 80% in the visible range of the spectrum and metallic conductivity of $\sim 10^{-4}\ \Omega^{-1}cm^{-1}$ at room temperature (Godinho, Walsh et al. 2008, Minami 2008). For this reason, the indium component of the TCOs used in transparent electrodes (TE) employed in the fabrication of liquid-crystal displays (LCDs) constitutes the largest use of this material (Minami 2008, Minami 2008). In addition to this niche, indium has found use in alkaline batteries (Mideen, Ganesan et al. 1989, Glaeser 1993) and thin-film solar cells (Minami 2008, Stadler 2012), notably expanding its current demand. Thus, it is widely believed that a shortage of material may occur in the near future because of the limited nature[1] of world indium reserves (Minami 2008).

As a consequence of this foreseen shortage, the price of this material has been enduring a considerable increase in the last decade (Minami 2008, Hoel, Mason et al. 2010). For instance, the price of indium metal was steady at \$72/kg before 1960 when its major usage was in solder alloys (Hoel, Mason et al. 2010). After 1970 the price fluctuated erratically and eventually rose to \$946/kg by 2005 followed by a decline to \$685/kg for 2008. The current price for indium is roughly \$800/kg (RotoMetals 2015). The search for novel indium-free materials with excellent TCO characteristics is therefore a crucial goal in future optoelectronic and electronics applications (Wang, Zhi et al. 2008).

Motivated by these requirements of transparent conductive and flexible technologies, the scientific community has been envisioning new solutions to eliminate or (in the worst-case scenario) reduce the use of indium in TCOs (Minami 2008). Reduced-indium TCOs such as ZnO-In_2O_3, ITO-$In_4Sn_3O_{12}$, and ZnIn-Sn-O multicomponent oxides are attractive candidates to reduce the use of indium by approximately half (Minami 2008, Minami 2008). The best solution, however, should be the improvement of current indium-free TCOs, for example throughout the use of SnO_2:x, ZnO:x, TiO_2:x semiconductors or through the use of new materials, such as graphene and some of its allotropes[2] (Ellmer 2012, Torres, Roche et al. 2014).

---

[1] The worldwide production in 2005 was 500t, which composes approximately 8% of the total estimated reserve base Hoel, C. A., T. O. Mason, J.-F. o. Gaillard and K. R. Poeppelmeier (2010). "Transparent Conducting Oxides in the ZnO-In2O3-SnO2System." Chemistry of Materials **22**(12): 3569-3579..

[2] Graphene, graphene nanoribbon, graphene nanotubes, bulkyballs, nanohorns, schwarzite crystals etc Torres, L. E. F., S. Roche and J.-C. Charlier (2014). Introduction to graphene-based nanomaterials: from electronic structure to quantum transport, Cambridge University Press.

1.2. Scope of the dissertation

The scope of this dissertation is to investigate the electrical, electronic, structural and/or transport properties of two emerging materials, tin dioxide (SnO_2) and graphene. With the help of the collected data in this work, obtained through quantum-mechanical simulations (density functional theory (DFT) and tight-binding theory (TBT)) and experimental measurements (Raman, X-ray photoelectron spectroscopy (XPS), atomic force microscopy (AFM), among others, provided by our collaboration group in Taiwan and Ireland), some current issues of these materials have been studied. Namely: (i) the origin of the n-type conductivity in SnO_2, (ii) the n-to-p conductivity transition in SnO_2, and (iii) band gap engineering (opening) of graphene.

The n-type conductivity in SnO_2 was achieved throughout two solutions: the first one through the combination of oxygen deficiencies and interstitial atoms inside the SnO_2 lattice, whereas in the second one, through the combination of interstitial and/or substitutional hydrogen atoms inside the SnO_2 lattice. The p-type conductivity was achieved by codoping n-type SnO_2 (from earlier configurations) with low concentrations of nitrogen and aluminum impurities. On the other hand, Stone-Wales (SW) defects placed at the borders of the GNRs are studied in order to understand the way in which the bandgap and therefore conductivity of graphene can be opened. The influence of multiple cleaning treatments on CVD (chemical vapor deposition) transferred GFET (a field-effect transistor (FET) using graphene as the channel material) devices was also investigated.

Based on the trend and results obtained in this work, the author strongly believes that these two materials in combination with enhancements of current recycling techniques can be the ultimate solution to indium scarcity problem, opening new frontiers in electronics and optoelectronics (Wager 2003, Georgiou, Jalil et al. 2013).

1.3. Dissertation outline

This dissertation is organized as follows:

Chapter 2 covers the basic theory of the SnO_2 crystal. Therein, the electrical and structural properties of this material will be reviewed. At the end of the chapter, the DFT parametrization in VASP will also be described. Then, chapter 3 will elaborate the fundamental theory of graphene and the other sp^2 allotropes, with focus on the structural and electronic properties of graphene nanoribbons (GNRs). The TB parametrization in ATK will be detailed at the end of this chapter. Moving on, in chapter 4, a thorough description and analysis of the results obtained for the two herein studied materials will be reported. Finally, chapter 5 ties together and synthesizes the various issues raised in the discussion sections, and based on the evidence accumulated until then, the conclusions will be drawn. Direction and areas for future research also will be provided in this chapter.

Chapter 2: Basics of SnO_2

2.1. Introduction

In recent years, great interest has been focused on SnO_2 owing to its importance in gas sensing, catalysis, and solar cells applications, at both the industrial and research level (Jarzebski and Marton 1976, Villamagua, Stashans et al. 2015). SnO_2 is a TCO material, which exhibits contradictory properties of high metallic conductivity (due to native point defects) with nearly complete, insulator-like transparency in the visible range (due to its ~3.6 eV wide-band-gap) (Jarzebski and Marton 1976, Hossain, Jennings et al. 2011). In addition to these properties, SnO_2 is non-toxic and displays excellent chemical- and thermal stability (Edwards, Porch et al. 2004). Therefore, the scientific community is currently considering SnO_2 as the prototype transparent conductor material to replace expensive ITOs (Gordon 2000, Fortunato, Ginley et al. 2007). A better understanding and control of both n- and p-type conductivity in SnO_2 would enhance its performance in existing applications and enable new ones, such as optoelectronics and transparent electronics.

In the first part of this chapter, it will be elaborated the basic theory of SnO_2 crystal. Following, it will provide a survey of its electrical and structural properties. Then, a review of the origin of the n-type conductivity and the possibility to achieve stable p-type conductivity in SnO_2 will be presented. The chapter concludes with a description of the computational method employed in the present study.

2.2. Crystalline lattice

Tin dioxide is an anisotropic polar crystal, which exhibits the tetragonal rutile structure with space group $\mathrm{D}_{4\mathrm{h}}^{14}$ or – in another notation – $\mathrm{P4_2/mnm}$ (Wyckoff and Wyckoff 1960, Svane and Antoncik 1987). Its unit cell contains six atoms, two tins (cations Sn^{4+}) and four oxygens (anions O^{2-}), whose atomic positions are determined by the *c/a* ratio and the internal parameter u. The cations are located at positions (0,0,0) and (½; ½; ½), while the anions at $\pm(u, u, o)$ or $\pm(½ + u, ½ - u, ½)$. Each cation has two anions at a distance of $\sqrt{2}ua$ (2.053 Å) and four anions at $[2(½ - \mathrm{u})^2 + 2(\mathrm{c}/2\mathrm{a})^2]^{1/2}$ (2.597 Å). The lattice parameters are $a = 4.737$ Å and $c = 3.185$ Å (*c/a* ratio is 0.673), while the internal parameter $u = [1 + 1/2(c/a)^2](\sim 0.307)$ (Svane and Antoncik 1987). The ionic radii for O^{2-} and Sn^{4+} are 1.40 and 0.71Å, respectively (Jarzebski and Marton 1976).

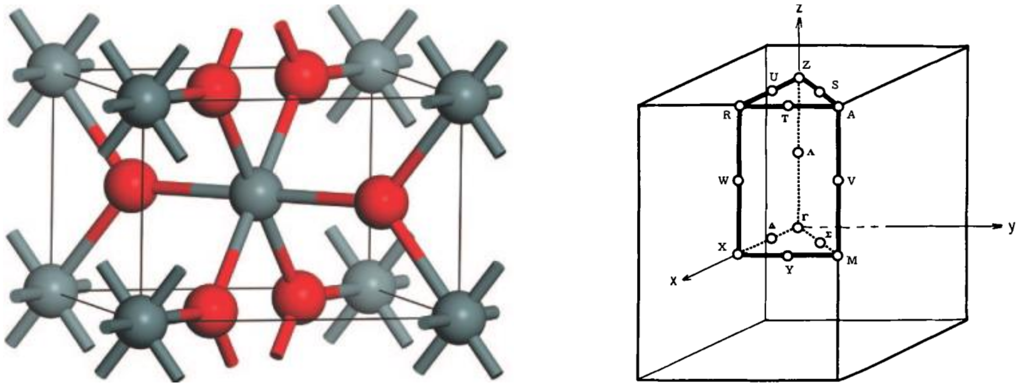

(a) (b)

Figure 2.1. (a) Unit cell of rutile SnO_2 (taken from (Godinho, Walsh et al. 2008)) and (b) its reduced lattice in the BZ (taken from (Arlinghaus 1974)). Red atoms are oxygen and gray atoms are tins, respectively.

Following this convention, each tin atom is at the centre of six oxygen atoms placed approximately at the corner of a regular (slightly deformed) octahedron. Every oxygen atom is surrounded by three tin atoms placed approximately at the corner of an equilateral triangle. Thus, the structure is said to have a 6:3 coordination. The structure of SnO_2 and its corresponding Brillouin zone (BZ) are depicted in Figure 2.1.

2.3. Band structure and density of states

The energy band structure calculated by Mishra et al. in (Mishra, Johnson et al. 1995) for the pure SnO_2 is depicted in Figure 2.2 as a plot of the energy levels along the lines of high symmetry in the BZ. Due to the large number of valence electrons in its unit cell, the band structure turn out to be very complicated.

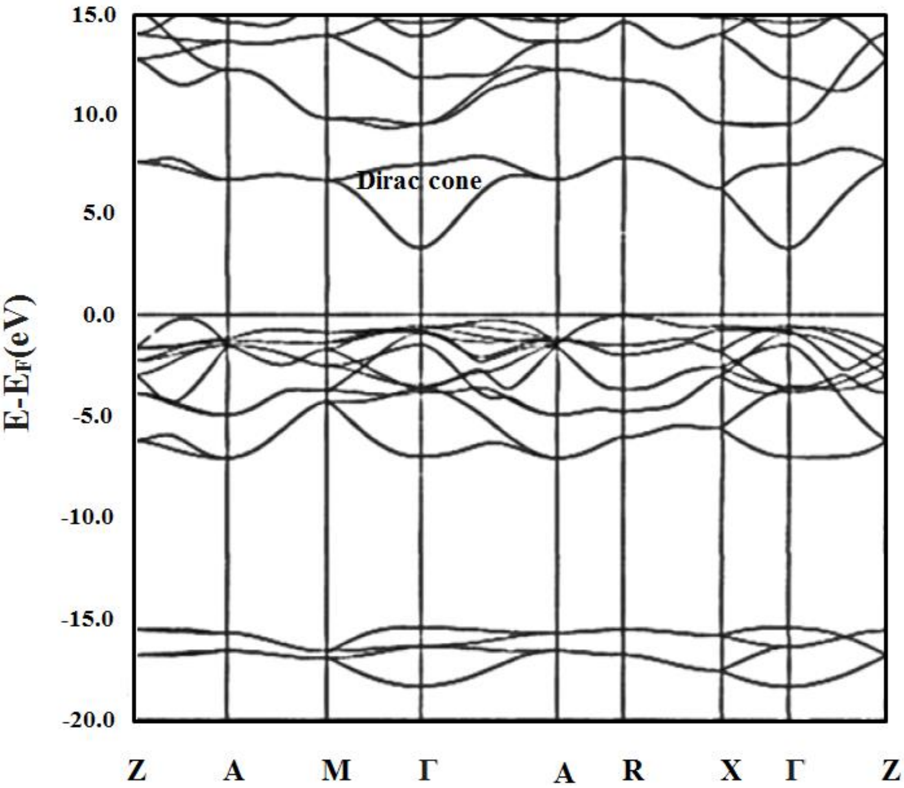

Figure 2.2. The energy band structure of SnO_2 is depicted as a plot of the energy levels along the lines of high symmetry in the BZ. The Fermi level is at the zero of the energy scale. Taken and adapted from (Mishra, Johnson et al. 1995).

One important feature to notice is that the maximum of the valence band (VB) is located at the R point on the BZ whereas the minimum of the conduction band (CB) is at the Γ point. The lowest-energy interband transition is a Γ→ Γ transition (3.7 eV). The theoretical results from Mishra *et al*, which displays similar features to those reported in (Svane and Antoncik 1987, áLe Blevennec 1997), are inconsistent with some experimental results where the minimum direct band gap is believed to correspond to a dipole-forbidden transition at the Γ-point. The experimental minimum band-gap magnitude varies from 2.25 to 4.4 eV depending on the sample purity (áLe Blevennec 1997). Another important feature to notice is that the CB exhibits significant free-electron-like character in the Γ→Z and Γ→X directions[3].

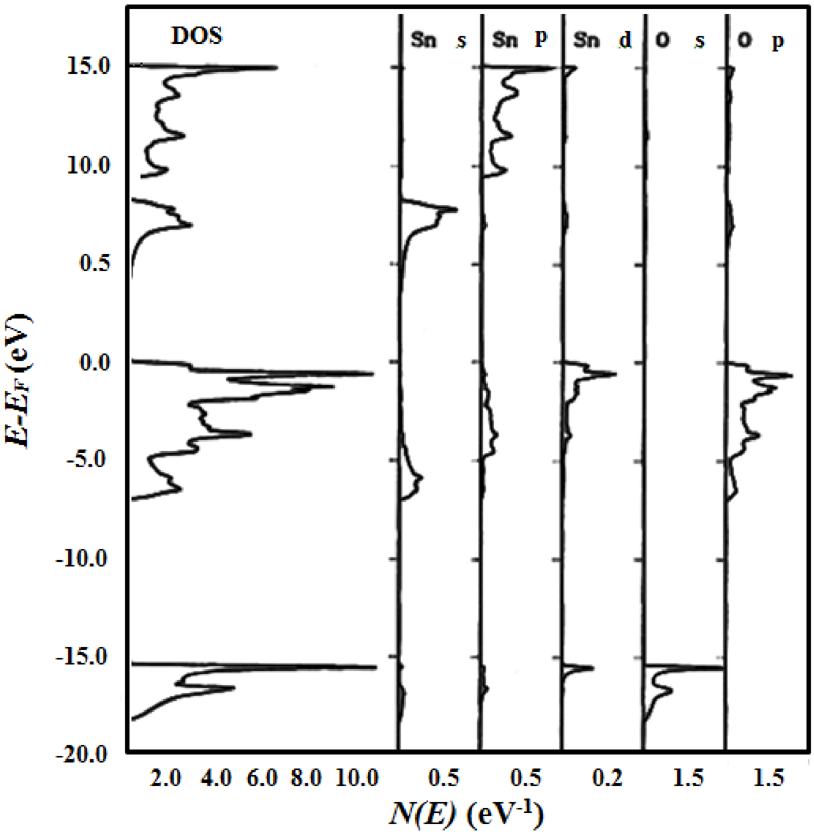

Figure 2.3. DOS of pure SnO_2. The first column shows the total density of states. The following columns contain the partial densities and consecutively, the s-, p-, and d-like partial DOS of Sn and the s- and p-like DOS of O. Taken from (Mishra, Johnson et al. 1995).

---

[3] Cone-like shape (also known as Dirac cone) in the band structure of materials implies that charge carriers behave as massless fermions. More information will be provided in chapter 3.

The partial density of states (PDOS) pattern of SnO_2 (**Figure 2.3**) indicates that a large contribution of Sn(s)-states is found at the bottom of the valence band between -7 and -5 eV. From -5eV to the top of the valence band, the Sn(p)-states contribution decreases while the Sn(d)-states contribution increases. A large and extended contribution of the O(p)-states is also found in the valence band. Clearly, bonding between the Sn and O is dominated by the p-states of the latter.

The CB shows a predominant contribution of Sn(s)-states up to 8 eV. For energies larger than 8 eV a contribution of Sn(p)-states is found to be large. The extended O(p) contribution is minimum. More information on the band structure of SnO_2 can be found in (Svane and Antoncik 1987, áLe Blevennec 1997) and references therein.

2.4. Electrical properties

Research on SnO_2 has been going on since 1910 (Chen, Pan et al. 2014) from both experimental and theoretical standpoint (Godinho, Walsh et al. 2008, Borges, Scolfaro et al. 2010). Consequently, many of its electrical, optical, magnetic, and structural properties are widely comprehended (Jarzebski and Marton 1976, Jarzebski and Marton 1976). For example, it is known that SnO_2 in its stoichiometric form (perfect crystallographic form) manifests an insulator behaviour (Varea 2007, Godinho, Walsh et al. 2008). It is also known that nominally pure[4] SnO_2 (or as grown SnO_2) is an n-type wide-band-gap (3.6–4.2 eV) (Oviedo and Gillan 2000, Ji, Zhang et al. 2013) semiconductor with optical transparency of up to 97% in the visible range (Ji, Zhang et al. 2013). The resistivity of this material (10^{-4} - 10^{6} $\Omega\cdot$cm (Manifacier, De Murcia et al. 1977, woo Lee, Kim et al. 2001)) is considerably lower than that of most semiconductors (10^{-3}-10^{9} $\Omega\cdot$cm) (Kılıç and Zunger 2002). Furthermore, nominally pure SnO_2 has a carrier density (n) of up to 10^{20} cm^{-3} (Jagadish and Pearton 2011) which is comparable to that of semimetals (10^{17}–10^{20} cm^{-3}) (Kılıç and Zunger 2002). This peculiar conducting-transparent behaviour occurs in just a few systems (Chen, Bagnall et al. 1998) such as the 4*d* metal oxides (SnO_2 and In_2O_3, CdO), being thus the rarest form of conductivity.

---

[4] Primitive material without any post modification.

The causes for the presence of the high unintentional conductivity in nominally pure SnO_2 are still unclear (Singh, Janotti et al. 2008, Ji, Zhang et al. 2013). On the one hand, the intrinsic ability of this material to conduct electrons has been often attributed to the presence of unintentionally created donor centres, usually identified as metallic interstitial (Sn_i) or oxygen vacancies (V_o) that produce shallow donor levels near the CB edge (Figure 2.4a) (Coutts, Mason et al. 1999, Ji, Zhang et al. 2013). These energy levels, which are located at around 30 and 150 meV below the CB, create only far-infrared (Drude-like) absorption, leaving the fundamental, across-the-gap absorption intact, i.e., the material remains optically transparent (Samson and Fonstad 1973, Kılıç and Zunger 2002). This stoichiometric deviation scenario (SnO_{2-x}) is in agreement with some experimental results, where: (i) high-purity samples display high resistivity (Gordon 2000) and (ii) the conductivity of the samples vary inversely with the oxygen partial pressure (Nagasawa and Shionoya 1971, Singh, Janotti et al. 2008).

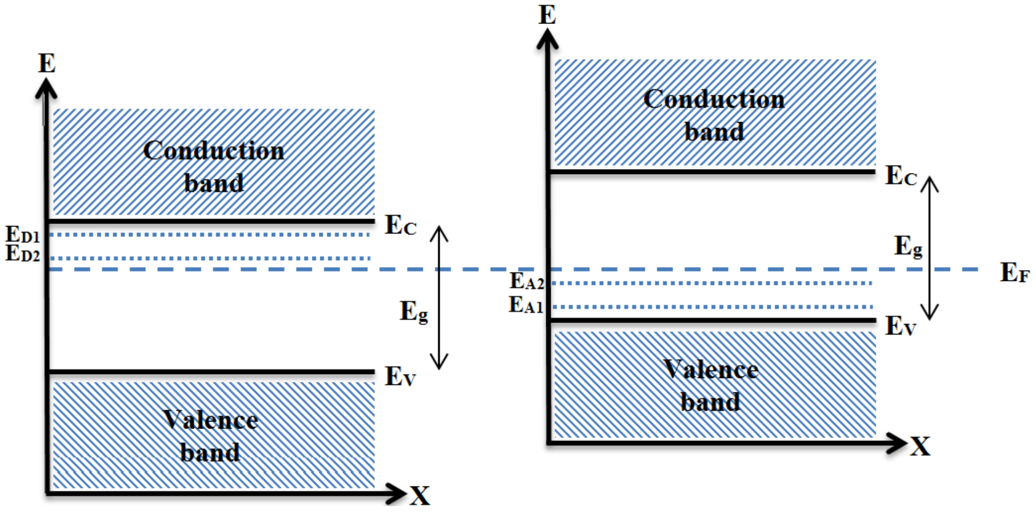

(a) (b)

Figure 2.4. A schematic band diagram of the SnO_2 endowed of n/p-type conductivity. Donor/acceptor levels (E_{D1} and E_{D2} /E_{A1} and E_{A2}) are located below/above the CB/VB.

However, as widespread as this oxygen vacancy scenario is, this model raises the following question: given that vacancies usually form deep (nonconductive) levels in the band gap of both insulators (alkali halides, SiO_2) and semiconductors (Si and GaAs) then how could oxygen vacancies in SnO_2 form shallow (conductive) levels? Recently

Singh *et al.* (Singh, Janotti et al. 2008) have put forward a new scenario to answer this question. According to their article, hydrogen atom (H), which is commonly present in (and difficult to exclude from) the various growth and processing environments, is a likely cause of the intrinsic conductivity exhibited in nominally pure SnO_2.

Native electrical properties of SnO_2 is usually enhanced through extrinsic aliovalent doping (Godinho, Walsh et al. 2008), e.g., with fluorine (F) (woo Lee, Kim et al. 2001, Wu, Liu et al. 2015) and antimony (woo Lee, Kim et al. 2001, Ji, Zhang et al. 2013) at anion and cation sites, respectively. F dopant has also been used, in fact this element has been particularly preferred to antimony because it produces the highest transparency and conductivity (Gamard, Jousseaume et al. 1999). Accordingly, thin films of F-doped SnO_2 (FTO) are within the most used TCO materials nowadays (Gamard, Jousseaume et al. 1999). Other dopants, such as tantalum, niobium, platinum, etc., are under investigation as well.

Moreover, despite the increasing attention put on the field of transparent electronics by the scientific and industrial communities (Singh, Janotti et al. 2008), its success depends on the ability to change the intrinsic n-type conductivity into p-type. This transition of conductivity in one single material will, in turn, bring about the long-sought transparent n-p junction (Villamagua, Stashans et al. 2015, Wu, Liu et al. 2015). The ambipolar behaviour in SnO_2 could lead to applications such as ultra violet (UV)-solar cells (Wu, Yoo et al. 1999, Liu, Hsieh et al. 2012), new generation display technologies (UV solid-state light emitting diodes (Leem, Song et al. 2004, Hossain, Jennings et al. 2011)), and ‘‘functional’’ windows, which transmit in the visible portion of the solar spectrum, yet generating electricity by absorbing in the UV region (Ni, Zhao et al. 2009).

Research on p-type conductivity in SnO_2 has begun only recently (Liu, Hsieh et al. 2012, Villamagua, Stashans et al. 2015) such that achieving reproducible high quality p-type material through doping (produce energy levels just above the top of the valence band by introducing acceptor defects into the n-doped SnO_2 lattice (shown in Figure 2.5b)) still poses challenges (Singh, Janotti et al. 2008). For instance, the doping level required to convert native n-type samples into *p*-type ones is very high (>15%) (Liu, Hsieh et al. 2012, Wu, Liu et al. 2015). Various cation dopants, such as Ga, Al, Sb, In, Zn, Fe, Co, and Li have been investigated in the last years (Liu, Hsieh et al. 2012).

These studies reveal that high doping concentrations (10^{21} - 10^{23} cm^{-3}) produce low hole concentration (10^{15} - 10^{19} cm^{-3}) (Ji, He et al. 2003, Huang, Ji et al. 2007).

Many research groups claim that the difficulty of changing the SnO_2 conductivity from n-type to p-type resides in the high concentrations of dopants required for the change to take place (Kawazoe, Yanagi et al. 2000, Liu, Hsieh et al. 2012). In case of the In-doped SnO_2, at least 20 mol% impurity concentration is required to achieve *p*-type electrical conductivity (Ji, Zhao et al. 2006). High impurity doping rates do not decrease even in In- and Ga-codoped samples in order to obtain required electrical behaviour, i.e. 20 mol% doping rate has to be maintained for both impurities (Mao, Ji et al. 2010). Li-doped SnO_2 materials obtained by spray pyrolysis technique are claimed to show p-type conductivity at 15 mol% of Li but 25 mol% of Li doping rate is preferred if one to obtain stable and lasting p-type samples (Bagheri-Mohagheghi and Shokooh-Saremi 2004). Investigation on Al-doped tin dioxide even argues that below 12.05 mol% of Al, the SnO_2 materials have n-type electrical conductivity (Ahmed, Khan et al. 2006). Recently carried out advanced DFT computations using hybrid functionals arrive to the conclusion that all p-type impurities considered in the SnO_2 lead to the localized hole polarons being centred on anion sites and as a consequence cannot produce p-type conductivity in SnO_2 (Scanlon and Watson 2012). Generally, very high concentrations of dopants entail instability and loss of the stoichiometry of the crystal, which in turn results in the degradation of its TCO properties.

The author has recently completed theoretical calculations (presented in chapter 4) based on density functional theory (DFT) within the general gradient approximation (GGA) to delve into both the n-type and p-type conductivity in SnO_2. It was studied (i) the origin of the n-type conductivity in SnO_2 from both (abovementioned) approaches and (ii) the conductivity transition from n-type to p-type in SnO_2 by co-doping the material with small quantities of N and Al.

2.5. Parametrization of SnO_2 into VASP

The numerical simulations were carried out by means of VASP (Kresse and Furthmüller 1996). The code allows to implement first-principles DFT calculations within the generalized gradient approximation (GGA) using the exchange–correlation term according to Perdew–Burke–Ernzerhof (Perdew, Burke et al. 1996). The interaction between the core electrons and the valence electrons was schemed through the projector augmented wave (PAW) pseudo-potential method proposed by Blöch (Blöchl 1994) and adapted by Kresse and Joubert (Kresse and Joubert 1999). The following valence configurations have been exploited here: $4d^{10}5s^25p^2$ for Sn, $2s^22p^4$ for O, $2s^22p^3$ for N, $3s^23p^1$ for Al, and $1s^1$ for H atoms, respectively.

Any technique based on the DFT-GGA experiences considerable difficulties when trying to achieve a correct description of the E_g for highly correlated materials, such as the case of SnO_2. One way to minimize this error is by including an intra-atomic interaction term for the strongly correlated electrons by an unrestricted Hartree–Fock (UHF) approximation, resulting in the so-called DFT + U approximation. By means of this additional U-term we widen the band-gap width by shifting the valence band (VB) downwards and the conduction band (CB) upwards. The U value and the lattice parameters, a and c, used throughout this work are 4.0 eV, 4.73 Å and 3.16 Å, respectively. These values were computed by our group previously and are detailed elsewhere (Stashans, Puchaicela et al. 2014).

A cut-off kinetic energy of 480 eV was used by converging the total energy to less than 1 meV/atom. The Γ-centred Monkhorst–Pack (MP) grid scheme with a 0.035 $Å^{-1}$ separation was applied which corresponds to a k-point mesh of 6 x 6 x 8 for the 6-atom primitive unit cell. These parameters, also detailed in (Stashans, Puchaicela et al. 2014), were obtained through the atomic relaxation until all the forces were <0.008 eV/Å and equilibrium state of the system was achieved.

The 6-atom primitive unit cell was expanded sixteen times (2 x 2 x 4 extension), which resulted in a 96-atom supercell and a corresponding k-point mesh of 3 x 3 x 2 was adopted to maintain the same MP grid with a 0.035 $Å^{-1}$ separation in the reciprocal space. All simulations were done using the 96-atom periodic supercell model.

Chapter 3. Basics of carbon allotropes

3.1. Introduction

A great interest has aroused in both scientists and technologists toward carbon allotropes since 2004 due to their extraordinary characteristics (Wang, Zhi et al. 2008). That year, Andre Geim and Kostya Novoselov at University of Manchester isolated graphene (single-atom-thick crystallites from bulk graphite) for the first time and studied the field-effect properties of the samples (Novoselov, Geim et al. 2004). Research on graphene has shown that this material possesses: induced superconductivity (Uchoa and Neto 2007, Profeta, Calandra et al. 2012), anomalous quantum Hall effect (Greiner 1985, Zhang, Tan et al. 2005), ultrahigh electron mobility (10^4 $cm^2V^{-1}s^{-1}$ at room temperature) (Chauhan and Guo 2010, Schwierz 2010, Deepak, Manoharan et al. 2011) and high transparency (>97% at room temperature). These characteristics have postulated the allotropes as promising materials for a wide range of nanoscience and nanotechnology applications (Geim and Novoselov 2007), such as gas sensors (Cheng, Li et al. 2010, Deepak, Manoharan et al. 2011), photovoltaics, and high-performance transistors (Chauhan and Guo 2010, Schwierz 2010). In particular, graphene-based transistors have developed quickly and are now considered an option for post-silicon electronics (Schwierz 2010).

In this chapter it will be elaborated the fundamental theory of graphene and the sp^2 allotropes, mainly focusing on the structural, electronic and transport properties of graphene and graphene nanoribbons (GNRs). At the end of this chapter, a description of the computational method employed in the present study will be provided as well.

3.2. The direct and reciprocal lattice

Graphene is a two-dimensional (2D) allotropic form made of sp^2-hybridized carbon atoms (Novoselov, Geim et al. 2004, Dubois, Zanolli et al. 2009), periodically arranged in an infinite hexagonal —often known as the honeycomb— network (Figure 3.1a) (Bruce, O'Hare et al. 2011, Wong and Akinwande 2011). Carbon atoms are located at the vertices of the hexagons in the graphene plane (Torres, Roche et al. 2014) and its structure belongs to one of the five 2D Bravais lattices called the hexagonal (triangular) lattice (Terrones, Botello-Méndez et al. 2010). Graphene structure can be described with a basis of two non-equivalent C atoms (A and B in Figure 3.1a) per unit cell. The primitive unit cell of the underlying Bravais lattice can be considered an equilateral parallelogram (shaded gray in Figure 3.1b) with side $a = \sqrt{3}a_{\mathrm{C-C}} = 2.46$ Å. The carbon-carbon bond length ($a_{\mathrm{C-C}}$) is equal to 1,42Å.

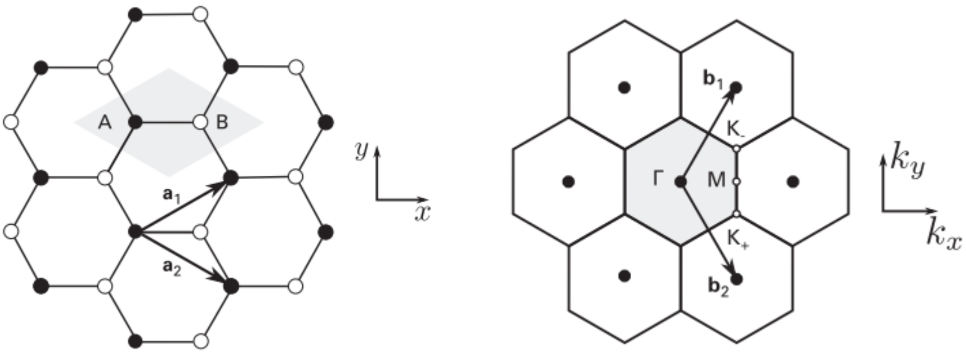

(a) (b)

Figure 3.1. Basis vectors in the hexagonal lattice of graphene (a) and its corresponding Brillouin zone (b). Taken from (Torres, Roche et al. 2014)

The primitive unit vectors ($\mathbf{a_1}$, $\mathbf{a_2}$), as defined in Figure 3.1a, are:

$$\mathbf{a_1} = a\left(\frac{\sqrt{3}}{2},\frac{1}{2}\right), \text{ and } \mathbf{a_2} = a\left(\frac{\sqrt{3}}{2},-\frac{1}{2}\right),$$

It is important to note that each A- or B-type atom is surrounded by three atoms of the opposite type (Semenoff 1984).

By using the condition $\mathbf{a_i}.\mathbf{b_j} = 2\pi\delta_{ij}$, the reciprocal lattice vectors ($\mathbf{b_1}$, $\mathbf{b_2}$), shown in Figure 3.1b, can be obtained through:

$$\mathbf{b}_1 = b\left(\frac{1}{2},\frac{\sqrt{3}}{2}\right), \mathbf{b}_2 = b\left(\frac{1}{2},-\frac{\sqrt{3}}{2}\right)$$

with $b = 4\pi/3a_{cc} = 4\pi/a\sqrt{3}$. The first BZ in the reciprocal space is shown in Figure 3.1b (shaded gray). Out of its six corners, two of them are inequivalent (the others can be written as one of these two plus a reciprocal lattice vector). These two special points are denoted with K_+ and K_-. The other high symmetry point is the one labeled with M. These symmetry points, widely known as the Dirac points, can be chosen as (Dubois, Zanolli et al. 2009, Pati, Enoki et al. 2011):

$$\mathbf{K}_+ = \frac{4\pi}{3a}\left(\frac{\sqrt{3}}{2},-\frac{1}{2}\right), \mathbf{K}_- = \left(\frac{\sqrt{3}}{2},\frac{1}{2}\right), \mathbf{M} = \frac{2\pi}{\sqrt{3}a}(1,0)$$

These points play an important role when studying the electronic properties of graphene (Cooper, D’Anjou et al. 2012).

3.3. Tight-binding description of graphene

The electronic structure of carbon allotropes fully engages to the hybridization (sp_1, sp_2, sp_3) of the constituting atoms and their arrangement within the lattice (Dubois, Zanolli et al. 2009, Cooper, D’Anjou et al. 2012). In graphene (sp^2-hybridized carbon), among the four valence orbitals of carbon (the 2s, $2p_x$, $2p_y$ and $2p_z$ orbitals), the s, p_x, and p_y orbitals combine to form the in-plane σ (occupied) and σ∗ (unoccupied) orbitals (Dubois, Zanolli et al. 2009). Such orbitals are even with respect to planar symmetry (Figure 3.2a). The σ bonds are strong covalent bonds, responsible for the elastic properties of graphene (and the other allotropes) (Dubois, Zanolli et al. 2009, Wolf 2014). The remaining p_z orbital, pointing out of the graphene plane, is odd with respect to the planar symmetry (Torres, Roche et al. 2014) (Figure 3.2a). This orthogonal p_z orbital overlaps with neighbouring p_z orbitals to form delocalized π (bonding) and π^* (anti-bonding) orbitals (Charlier, Blase et al. 2007).

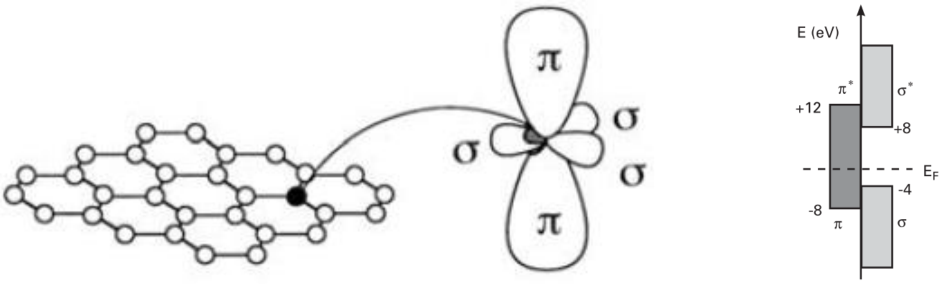

(a) (b)

Figure 3.2. Orbital configuration of a C atom in the honeycomb. The three sp^2 hybrid orbitals are in the same plane and form σ bonds. The single orthogonal p_z orbital overlaps with neighbouring p_z orbitals to form π bonds. Taken from (Dubois, Zanolli et al. 2009).

Since, the bonding and antibonding σ bands are strongly separated in energy (> 12 eV at Γ, as shown in Figure 3.2b), their contribution to electronic properties is commonly disregarded (Geim and Novoselov 2007, Fujita and Suzuki 2013). Therefore, the VB and CB, generated by the bonding π and antibonding $\pi*$ orbitals, completely describe the low-energy electronic excitations in graphene (Neto, Guinea et al. 2009).The electronic properties of graphene can be described using a simple nearest-neighbor TB model in which, as already mentioned, the p_z electrons are treated independently of other valence electrons (Reich, Maultzsch et al. 2002). The TB calculations that account only for interactions between nearest neighbours lead to an energy dispersion (shown in Figure 3.3) of the form (Neto, Guinea et al. 2009).

$$E_{\pm}(\mathbf{K}) = \pm\gamma_0|\alpha(\mathbf{K})|$$

$$E(\mathbf{K}) = \pm\gamma_0\sqrt{3 + 2\cos(\mathbf{k}.\mathbf{a_1}) + 2\cos(\mathbf{k}.\mathbf{a_2}) + 2\cos(\mathbf{k}.(\mathbf{a_2} - \mathbf{a_1}))}$$

The wavevectors $\mathbf{k} = (k_x, k_y)$ are chosen within the first BZ. Clearly, the zeros of $\propto(\mathbf{K})$ correspond to the crossing of the bands with the + and − signs. One can verify that $\propto(\mathbf{k} = \mathbf{K}_+) = \propto(\mathbf{k} = \mathbf{K}_-) = 0$ and therefore the crossings occur at the points $\mathbf{K}_+$

and $\mathbf{K}_{-}$. Furthermore, with a single p_z electron per atom in the π-$\pi*$ model, the (−) band is fully occupied, while the (+) branch is empty, at least for electrically neutral graphene. Graphene displays a metallic (zero-gap) character. However, as the Fermi surface is of zero dimension (since it is reduced to a discrete and finite set of points), the term semi-metal or zero-gap semiconductor is usually employed (Torres, Roche et al. 2014).

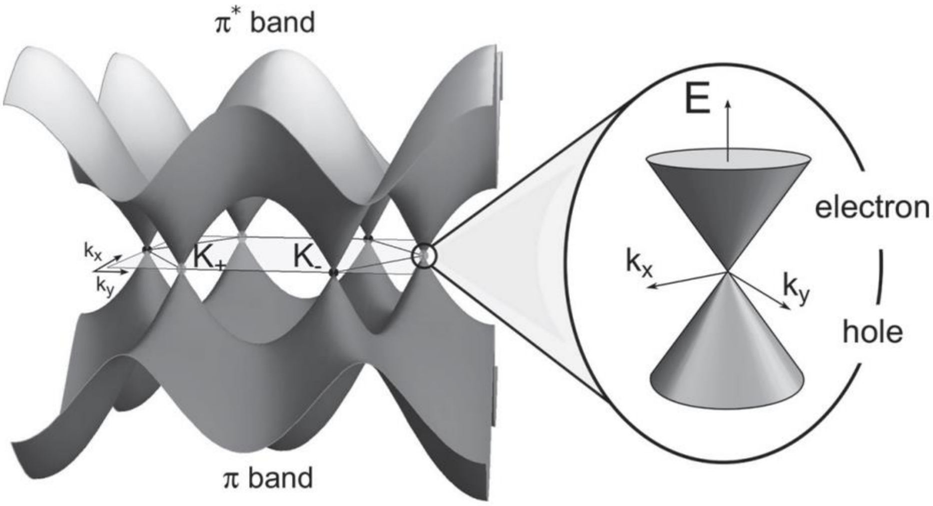

Figure 3.3. Energy bands of graphene. The Dirac-like features are the linear energy dispersions, present near the neutral points K, K’. Taken from (Torres, Roche et al. 2014)

Expanding the equation above for $\mathbf{k}$ in the vicinity of K_{+}(or K_{-}), $\mathbf{k} = \mathbf{K}_{+} + \delta\mathbf{k}(\mathbf{k} = \mathbf{K}_{-} + \delta\mathbf{k})$, yields the linear dispersion[5] ,for the π and $\pi*$ bands near these six corners of the 2D hexagonal BZ,

$$E_{\pm}(\delta\mathbf{k}) = \pm\hbar\nu_F|\delta\mathbf{k}|,$$

where

$$\nu_F = \frac{\sqrt{3}\gamma_0 a}{2\hbar} = 3ta/2\hbar \cong 10^6\mathrm{m/s}$$

is the Fermi velocity (Obeng and Srinivasan 2011). This energy relation corresponds to massless relativistic particles in which the charge carriers have speeds 300 times less than the speed of light (Neto, Guinea et al. 2009, Sagar 2011). That is, charge carriers

---

[5] In conventional semiconductors, the energy-momentum relation obeyed by electrons is quadratic.

travel through graphene as if they were massless Fermions obeying a Dirac equation (Wallace 1947, Obeng and Srinivasan 2011) (Castro, Novoselov et al. 2007).

3.4. Carbon allotropes

Graphene has been envisioned as the building block of all other sp^2-hybridized carbon allotrope forms (Figure 3.4) (Novoselov, Geim et al. 2004, Allen, Tung et al. 2009), including fullerenes, graphite, and GNRs (Wallace 1947). Interestingly though, graphene was the last allotrope to be (experimentally) discovered as it was presumed not to exist as a free standing material due to the unstable nature of 2D materials (Landau 1937, Obeng and Srinivasan 2011). Prior to 2004, graphene was known to exist only as a constituent part of graphite (Obeng and Srinivasan 2011, Torres, Roche et al. 2014). That year, however, scientists from Manchester University, Andrei Geim and Kostya Novoselev, isolated graphene for the first time and studied its ambipolar field-effect of their samples (Novoselov, Geim et al. 2004, Allen, Tung et al. 2009). This subsequently resulted in the popularisation of the material, especially amongst condensed-matter physicists and recently for the electron-device community (Deepak, Manoharan et al. 2011, Cao, Chen et al. 2012). Gem and Novoselev's pioneering efforts were bagged with the Nobel Prize in Physics in 2010 (Dresselhaus and Araujo 2010, Hancock 2011). In the following sections it will be provided a brief review of each carbon allotrope.

Fullerenes are carbon molecules in which the atoms arrange in hollow shapes (sphere, ellipsoid, tube) (Hirsch 1994). The scientific community has focused research mainly in spherical fullerenes (also called buckminsterfullerene or buckyball) and cylindrical fullerenes (also called carbon nanotubes (CNTs) or buckytubes) (Hirsch 2009, Dumlich and Reich 2010). Buckyballs can be found in small quantities in soot, making them the most common fullerene found in nature (Lusk and Carr 2008). Fullerenes are similar in structure to graphite, but they may also contain pentagonal (or sometimes heptagonal) rings that make the planar structure to wrap.

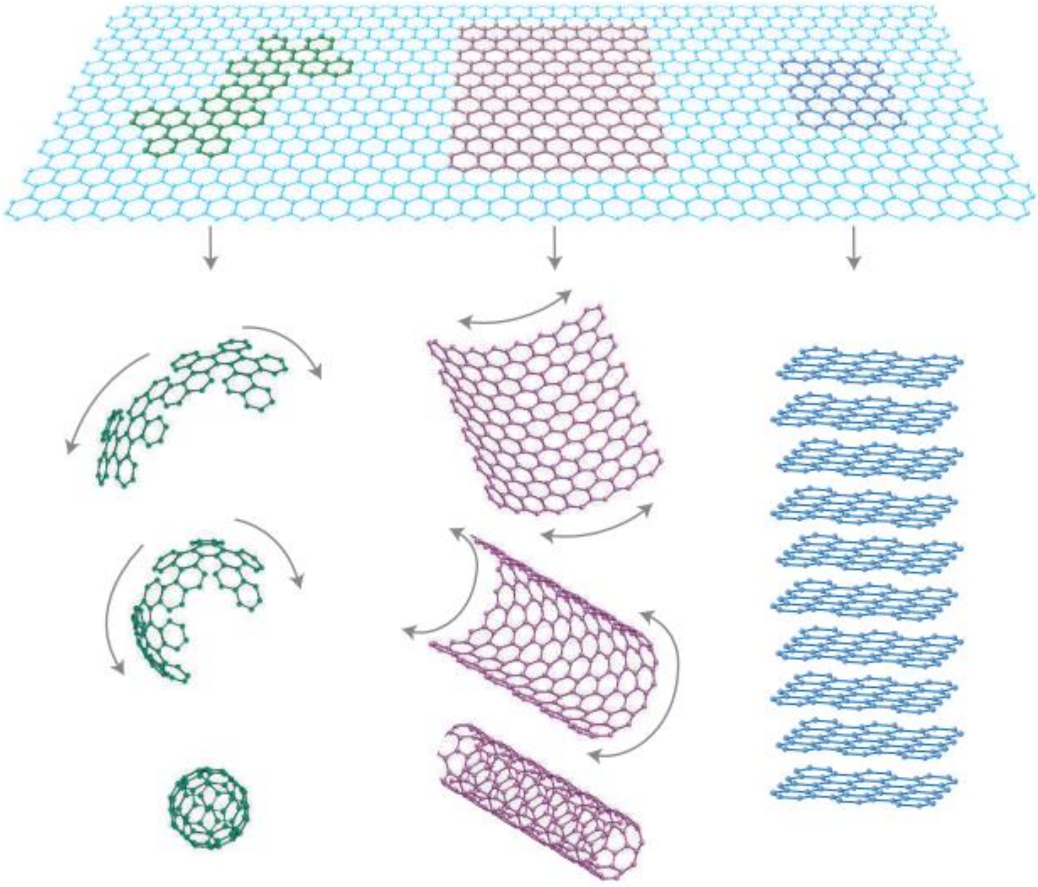

Figure 3.4. The planar hexagonal structure of graphene can be considered as the building material for all other sp^2-allotropes. i.e., it can be wrapped up into 0D buckyballs, rolled into 1D nanotubes or stacked into 3D graphite. Taken from (Geim and Novoselov 2007).

CNT exhibit a wide range of novel mechanical and electronic properties that could be applied in many fields, such as nanoelectronics, nanosensors, photonics, nanomechanical devices, among others (Jorio, Dresselhaus et al. 2007, Ismail, Ahmadi et al. 2012). However, the difficulty to synthesize them (Harris, Zhou et al. 2001, Liang 2008) and their incompatibility with planar technologies has led to the search of a successor material (Samadi and Faez 2013). GNRs fulfil those requirements, displaying similar electronic/magnetic properties to CNTs, being also compatibility with planar technologies (Chauhan and Guo 2010). This could solve large-scale integration hurdles of CNTs (Han, Özyilmaz et al. 2007, Samadi and Faez 2013).

3.5. Graphene nanoribbons

GNRs are basically elongated strips of single layered graphene with a finite width (typically less than 10 nm (Li, Wang et al. 2008, Wang, Ouyang et al. 2008)) that can be obtained by cutting a graphene sheet along a certain crystallographic orientation (angle or chirality) (Barone, Hod et al. 2006, Dubois, Zanolli et al. 2009) (Figure 3.5). The microscopic structure of GNRs is closely related to that of graphene, and so their properties. However, due to the quantum confinement effect (QCE) (Torres, Roche et al. 2014) experienced by the electrons inside these quasi-one-dimensional (1D) structures, additional properties beyond that of graphene can be observed, e.g., opening of E_g (Han, Özyilmaz et al. 2007, Kan, Yang et al. 2011).

There are an infinite number of ways (chiralities) of cutting a sheet into a ribbon (Dutta and Pati 2010). Within the most studied GNRs are armchair (AGNRs) and zigzag (ZGNRs) edged nanoribbons, which show different charters: semiconducting and metallic, respectively (Han, Özyilmaz et al. 2007, Dutta and Pati 2010). Recent experimental studies reveal that ZGNRs possess localized edge states with energies near the E_F (Nakada, Fujita et al. 1996, Kobayashi, Fukui et al. 2005). These edge states correspond to the non-bonding molecular orbitals (Nakada, Fujita et al. 1996), and are responsible for the magnetism (Nakada, Fujita et al. 1996, Dutta and Pati 2010). Edge states are completely absent for AGNRs (Dutta and Pati 2010).

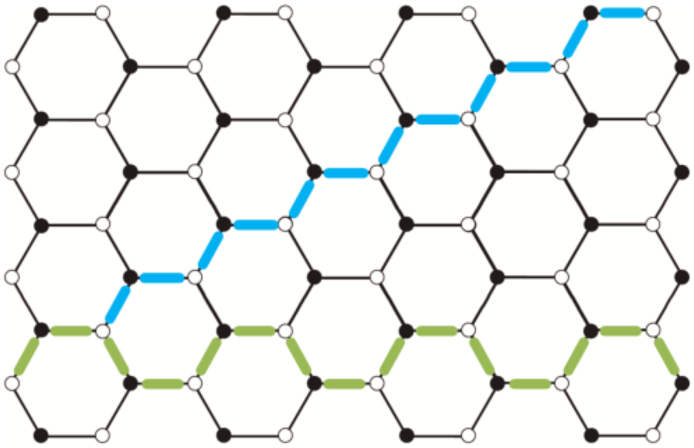

Figure 3.5. Honeycomb lattice of graphene with both zigzag (light blue) and the armchair (green).

In addition to QCE and chirality, the electrical properties of GNRs are strongly dependent on their widths (w) and distortions at their edges. On the one hand, GNRs have shown to be semiconductors with band gaps that scale inversely against the nanoribbon width (Hancock, Uppstu et al. 2010). On the other hand, edge distortions modify the edge states of the GNRs as their properties are associated primarily with the geometry rather than the chemistry itself (Chauhan, Srivastava et al. 2013).

Consequently, a deep understanding of the modification on the electronic structure and thermodynamic stability of GNRs is necessary before considering carbon allotropes as building blocks in silicon-based CMOS and related technologies (Dubois, Zanolli et al. 2009, Cao, Chen et al. 2012). In chapter 4, it is presented the results obtained from TB simulations of defected GNRs. The results put forward the way in which E_g can be engineered (opened) through the insertion of defects at the edges of the GNRs.

3.6. Parametrization of the AGNRs into Atomistic Toolkit

Geometry optimization of AGNRs was carried out by DFT using a plane-wave basis set and PAW pseudopotentials for the description of the electron–ion interaction. Periodic boundary conditions perpendicular to the ribbon and the unit cell padding distance is set to 10 Å to reduce any residual electrostatic interactions with the periodic images of the ribbon. An energy cut-off value of 150 Ry was selected to ensure accurate results. The Brillouin zone k-point sampling was done by using the Monkhorst–Pack algorithm, and 1x1x100 k-points were chosen for the fully self-consistent calculations. The geometry for each AGNR studied was fully relaxed until the force on each of the atoms was less than 0.01 eV Å^{-1}. To describe the electronic properties of the nanoribbon, it was found more suitable to use the TB approximation for the π electron as described in (Faez and Barami 2013, Uppstu 2014). A TB Hamiltonian (H) with modified hopping parameters was used to describe the band structure of the AGNRs. The one-orbital first-neighbor tight-binding model including the Hubbard term as follows:

$$H = \sum_{i,j} t_{i,j} c_{i,\sigma}^{t} c_{j,\sigma} + U \sum_{i} (n_{i,\uparrow}\langle n_{i,\downarrow}\rangle + n_{i,\downarrow}\langle n_{i,\uparrow}\rangle$$

With $c_{i,\sigma}^{t}$ and $c_{j,\sigma}$ being the creation and annihilation operators, respectively, for an electron of spin σ in the π orbital of the ith carbon atom, and $n_{i,\sigma}$the corresponding number operator. Here it was chosen t=-2.74 eV and U=-2t. The TB model is a very simple model for electronic structure calculations. Its advantage over ab initio methods is its low computational cost, which enables simulating systems that are large enough to contain even millions of atoms (Uppstu 2014). Despite the simplicity of the model, it is relatively accurate, especially for carbon-based materials such as graphene.

In this work, atomic visualizations were done with Virtual NanoLab (VNL) (Toolkit) while calculations were done using the Atomix Toolkit (ATK) package (Toolkit , Simulator 2012).

Chapter 4. Discussion of results

4.1. Introduction

The present research primarily was dedicated to study the electrical and structural properties of SnO_2 and graphene materials from the theoretical viewpoint. Nonetheless, experimental results, obtained through the collaboration with the Tyndall National Institute (Ireland) and the National Central University, Jhong-Li (Taiwan), were employed to booster the findings of the main line of investigation.

The DOS pattern and the band structure were used to predict the electrical behavior of the materials (e.g., type of conductivity and band gap width). The Bader population analysis along with a close examination of the spatial positions of the defect-nearby atoms shed light on their structural changes.

The resistivity, carrier mobility and the carrier concentrations of the TFT devices were conducted by Hall measurement. The crystalline parameters were investigated by XRD, while the dopant concentrations were examined by XPS. The carrier type and carrier mobility of the GFET devices was carried out by field-effect measurements. The surface morphology was investigated in AFM. In addition, Raman spectroscopy was used to develop a qualitative analysis of the graphene flakes inside the FET structure.

4.2. Origin of the intrinsic n-type conductivity in SnO_2

As already mentioned in Chapter 2 (section 2.4), the intrinsic ability of SnO_2 to conduct electrons has been often attributed to the presence of unintentionally created donor centers, usually identified as metallic interstitials or oxygen vacancies that produce shallow donor states near the CB edge (Varea 2007, Choi, Hwang et al. 2008). However, recently Singh et. al. (Singh, Janotti et al. 2008) have put forward an alternative scheme to explain this phenomena: the doping the SnO_2 crystal with interstitial/substitutional H atoms (H_i or H_{sub}). Both schemes were exploited as detailed below.

4.2.1. First scheme to achieve n-type conductivity in SnO_2

In the first scheme, the unintentional n-type conductivity observed in nominally pure SnO_2 samples was reproduced by removing one of the host oxygen atoms (V_O) located in the central part of the supercell and by taking one tin atom from its lowest energy position to an interstitial one; this scheme will be called “the SnO_2+V_O+Sn_i scheme” throughout this dissertation. The equilibrium configuration for this scheme is depicted in Figure 4.1 (the POSCAR file which contains the lattice geometry and the ionic positions of this configuration can be found in appendix A.1).

Only the atoms situated rather close to the point defect, up to 2.06 Å, tend to displace themselves in search for new stable positions (Table 4.1). The Coulomb electrostatic interaction is not the main source of the observed atomic movements with respect to the defect according to analysis of atomic charges obtained by the Bader population analysis implemented in the algorithm explained elsewhere (Henkelman, Arnaldsson et al. 2006). It is clear that atomic charges do not change notably except the charges on three Sn atoms situated close to the vacancy. Sn atoms which surround V_O tend to reduce their initial distances till the vacancy in order to fill the empty space left by the missing atom. Sn(1) and Sn(2) atoms displace by approximately the same amount while

Sn(3) atom shifts less since its charge suffers smaller change; additionally we suppose that Sn(3) might interact electrostatically with the Sn_i. So, the main reason of atomic displacements could be the tendency to fill empty space created by the V_O point defect. Oxygen atoms rearrange themselves around Sn and Sn_i atoms in order to preserve initial Sn–O bond lengths as close as those in the pristine structure of SnO_2 (~2.05 Å).

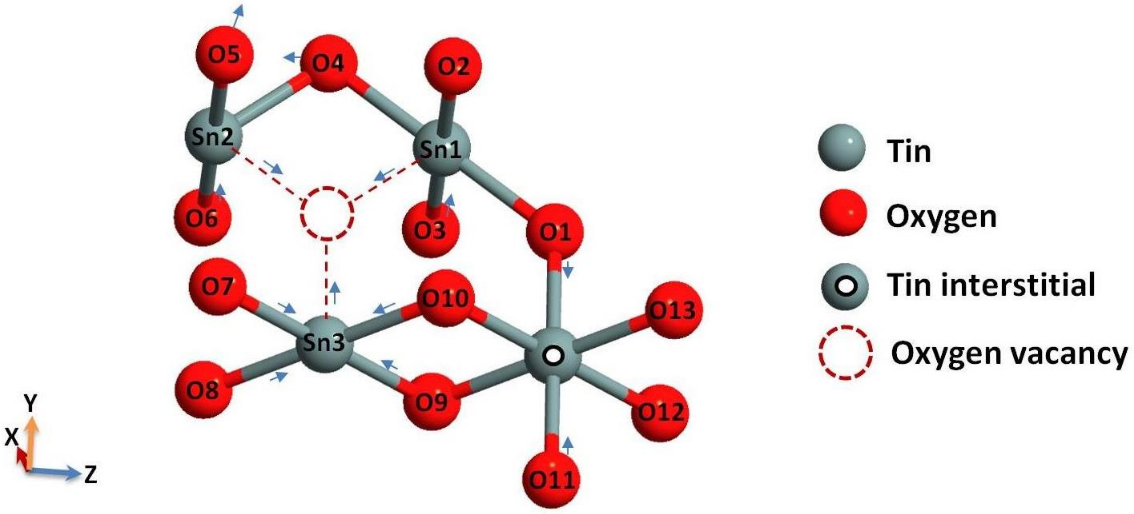

Figure 4.1. Schematic diagram of the atomic displacements in SnO_2 containing V_O and Sn_i intrinsic point defects.

Total DOS, shown in Figure 4.2, was calculated in order to account for the changes of the compound's electronic properties. The position of E_F for the SnO_2 containing the V_O+Sn_i pair is found at the bottom of the CB. That clearly indicates the existence of free electron within the lower part the CB, which in turn ratifies the n-type electrical conductivity in the SnO_2 crystal.

It is important to mention that V_O alone *does not show* any trace of n-type conductivity. Figure 4.3 shows the DOS pattern of a configuration in which only V_O has been included into the SnO_2 lattice. The position of Fermi level, which lies in the middle of the band gap, corroborates this fact. The POSCAR file which contains the lattice geometry and the ionic positions of this configuration can be found in Appendix A.2.

Table 4.1. Charges on atoms obtained by the Bader population analysis for the perfect (Q_1) and n-type undoped (Q_2) SnO_2 crystals. The atomic displacements regarding the point-defect for atoms within the defective region are also shown. Negative atomics displacements stand for the defect-inward shifts. The atomic numeration corresponds to the one indicated in Figure 4.1.

Defect	**Q_1 (e)**	**Q_2 (e)**	**ΔR (Å)**	**Nearby atoms**
V_O	2.41	2.01	-0.06	Sn (1)
	2.41	2.04	-0.05	Sn (2)
	2.42	2.12	-0.02	Sn (3)
	-1.20	-1.20	0.01	O (1)
	-1.21	-1.22	0.00	O (2)
	-1.21	-1.23	-0.02	O (3)
	-1.21	-1.21	0.02	O (4)
	-1.21	-1.22	0.01	O (5)
	-1.21	-1.23	-0.01	O (6)
	-1.21	-1.22	-0.03	O (7)
	-1.21	-1.21	-0.04	O (8)
	-1.21	-1.21	-0.04	O (9)
	-1.21	-1.22	-0.02	O (10)
Sn_i	-1.20	-1.20	-0.01	O (1)
	-1.21	-1.21	0.01	O (9)
	-1.21	-1.22	0.01	O (10)
	-1.21	-1.23	-0.01	O (11)
	-1.21	-1.22	0.00	O (12)
	-1.21	-1.23	0.00	O (13)

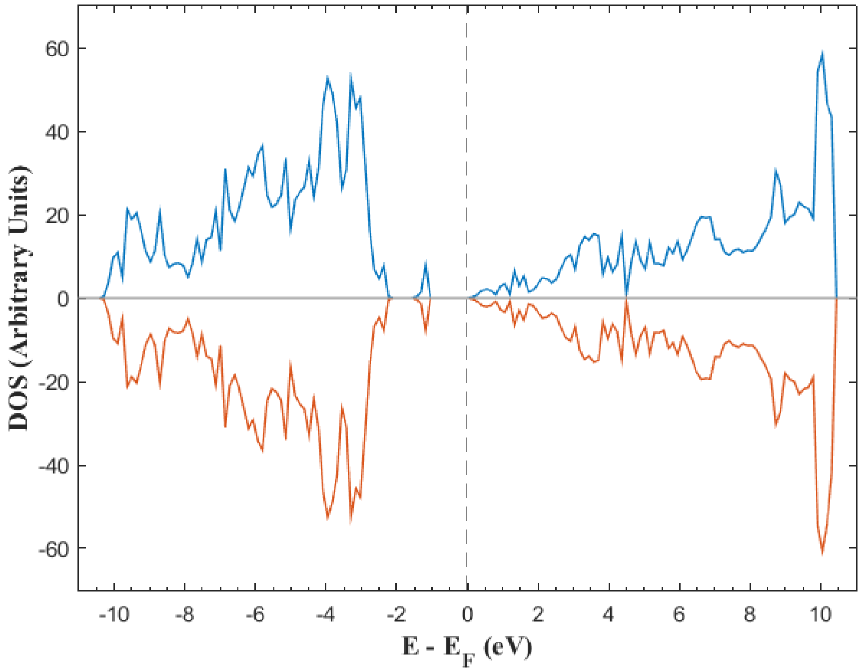

Figure 4.2. Total DOS of SnO_2 endowed with n-type conductivity. The dashed grey line marks the E_F.

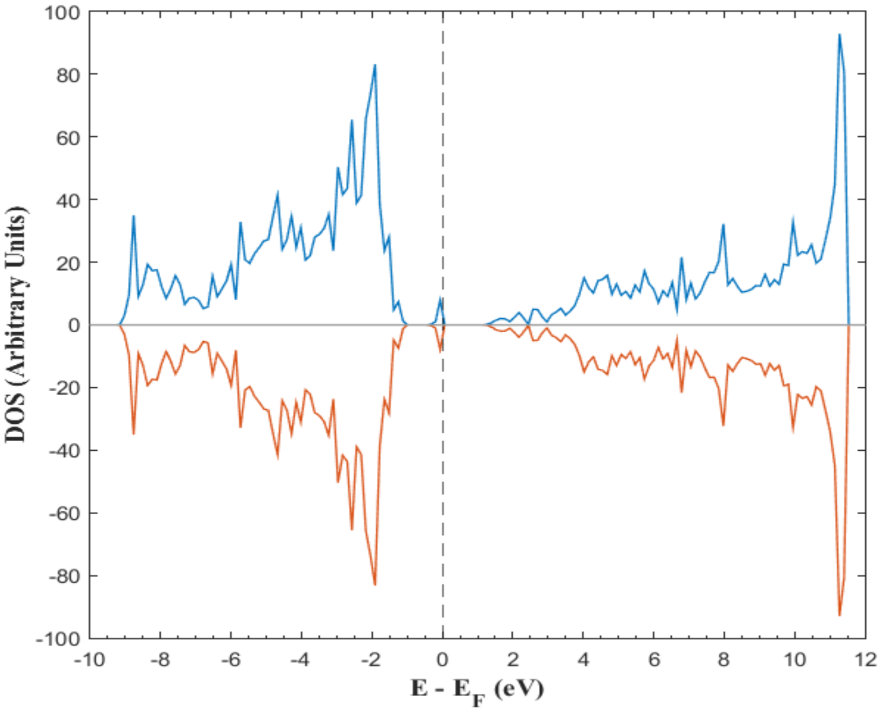

Figure 4.3. Total DOS of SnO_2 when V_O has been added to the crystalline lattice. The Fermi level (dashed gray line) located in the middle of the band-gap suggest that no conductivity has been acquired by the crystal.

4.2.2. Second scheme to achieve n-type conductivity in SnO_2

In the second scheme, the interplaying of H_i, H_{sub} and/or V_O point defects within lattice sparked the alluded n-type conductivity in SnO_2. Data in this section, obtained from nine configurations, has been organized into three main categories (Table 4.2**)** and detailed below.

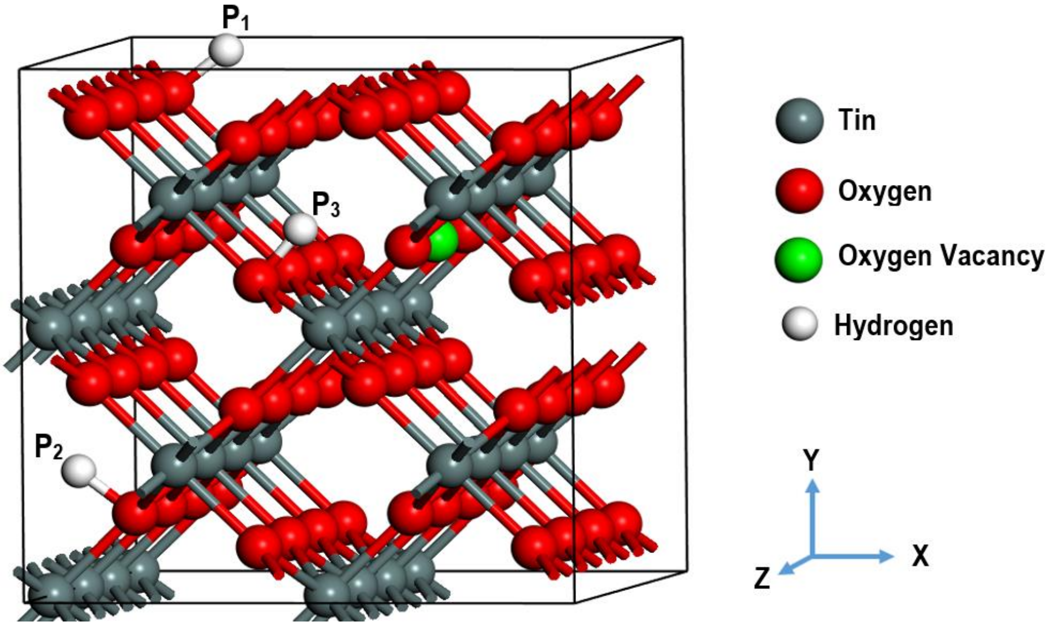

Figure 4.4. Schematic diagram showing considered positions for the V_O and H atom in the pure SnO_2 lattice.

The first group (SnO_2+V_O+H in Table 4.2) describes the cases in which the H atoms were placed inside an oxygen deficient SnO_2 lattice (V_O included). The locations that the H atoms assumed with respect to V_O were P_1 (7.1 Å from V_O), P_2 (6.3 Å from V_O) and P_3 (5.0 Å from V_O) in Figure 4.4. The fourth configuration in SnO_2+V_O+H represents the case in which the H atom was situated at the V_O site, therefore being considered as a substitutional H atom. In the second group (SnO_2+H in Table 4.2) the H atom was placed at P_1, P_2 and P_3 in Figure 4.4. In contrast to the SnO_2+Vo+H group, V_O was not included within the lattice in this group. Modelling of the second group of configurations was carried out in order to determine the contribution of V_O to the n-type conductivity of SnO_2 (if any). Finally, the third group (SnO_2+2H in Table 4.2) describes the case of two H atoms situated at different positions. Simulations for the third group were performed in order to determine development of the n-type conductivity as the concentration of H was increased.

Analysis of the total energies of the configurations in SnO_2+Vo+H indicates that P_1, P_2, and P_3 sites were equally favorable. H_{sub} site was found to be the most stable configuration, displaying a total energy of roughly 0.8 eV lower than that of the other sites. This is in perfect agreement with the work of Singh *et. al.*(Singh, Janotti et al. 2008).

By comparing the DOS patters of the first two groups (Figure 4.5 and Figure 4.7), one can notice that in the presence of V_O there exist a local occupied state situated about 0.98 eV above the upper VB edge. This state can be interpreted as a localized F-center in SnO_2 due to the V_O. Formation of F-center as well as practically equal free-carrier densities with and without V_O (Table 4.2) implies that presence of V_O is not required at all for SnO_2 in order to exhibit n-type electrical conductivity.

Values of free-carrier density, n, calculated in electrons per cubic centimeter (cm^3) for the configurations investigated in this section were in good agreement with the available experimental findings (Goyal, Agashe et al. 1993, Kılıç and Zunger 2002) for nominally undoped SnO_2 crystals. n was calculated by integrating the product of the density of states ($g_C(E)$) with the probability density function ($f(E)$) from the bottom of the CB (labelled E_C) up to the Fermi level (E_F) in the corresponding DOS patterns and is expressed as follows:

$$n = \int_{E_C}^{EF} g_C(E) f(E) dE \qquad 4.1$$

For a deeper description of the method look through reference (Hu 2010).

No big difference could be appreciated between n of the configurations of the first group. Also, n for the first group is similar to those of the SnO_2+H group. These preliminary results lead to the conclusion *that V_O does not contribute to the generation of free carriers in the material* on contrary to the general scientific view on this point.

Table 4.2. Free-carrier density (*n*), O-H bond length, and atomic charges on H are summarized for each one of the configurations depicted in Figure 4.5. The POSCAR file which contains the lattice geometry and the ionic positions of the best configuration can found in Appendix A.3.

Group	Positions of H	*n* (e / supercell)	*n* (e / cm^3)	O-H bond (Å)	Q_H (e)
SnO_2+V_o+H	P_1	1.002	$8.772*10^{20}$	0.998	0.63
	P_2	1.006	$8.825*10^{20}$	0.999	0.62
	P3	0.969	$8.485*10^{20}$	0.999	0.62
	V_o	1.010	$8.877*10^{20}$	–	-0.48
SnO_2+H	P_1	1.022	$8.995*10^{20}$	1.001	0.61
	P_2	1.021	$8.950*10^{20}$	1.000	0.62
	P_3	1.010	$8.846*10^{20}$	1.000	0.62
SnO_2+2H	P_1 & V_0	2.042	$1.778*10^{21}$	1.002	0.64 & -0.47
	P_1 & P_2	2.040	$1.771*10^{21}$	1.000	0.61 & 0.61

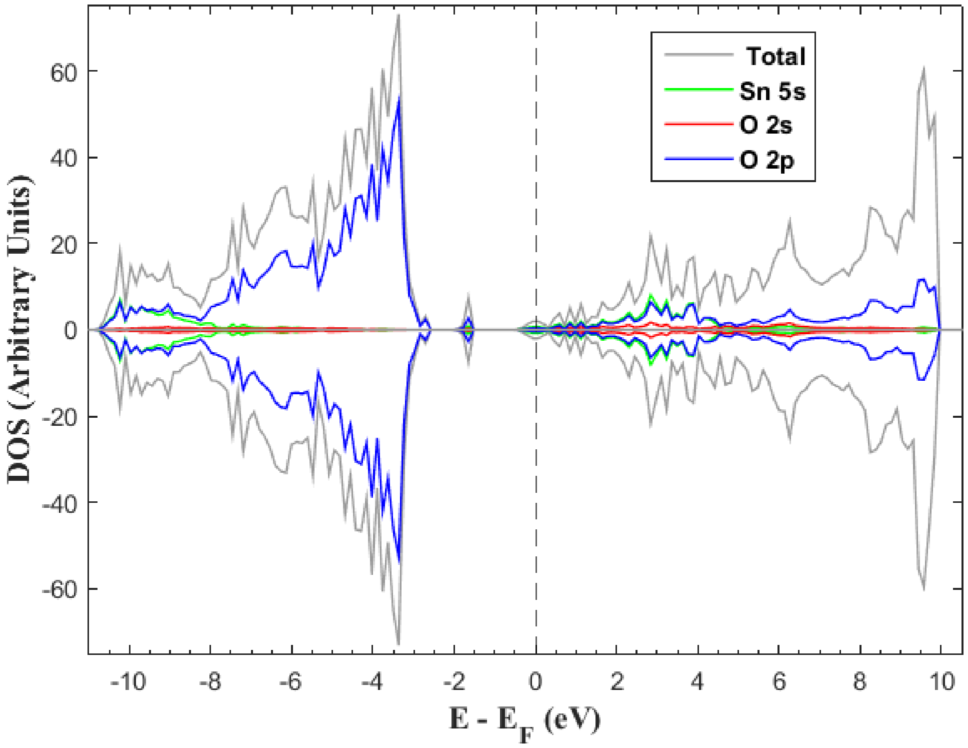

Figure 4.5. DFT+*U* computed total and partial DOS for SnO_2+V_O+H configuration if the H atom is at the site P_1. The dashed gray line marks the E_F. Integration from the bottom of the CB up to E_F represents the value of free-carrier density: *n*. DOS patterns for the rest of the group SnO_2+V_O+H configurations are practically identical.

Addition of H atom and V_O into the SnO_2 crystalline lattice produced perturbation and consecutive shifts for the atoms situated close to the point defects. As one can observe from Figure 4.6, the atomic displacements are predominantly inward with respect to the H impurity for oxygens and mainly outward for Sn atoms. The O-H interatomic distance was found to be ~1.0 Å. Computed atomic charges, using the Bader population analysis show, small increase, about 0.03 *e* on average per atom, when H has been introduced thus implying importance of Coulomb electrostatic interaction in lattice distortion. Positive atomic charges on H (Table 4.2) demonstrate that it loses its only electron after being inserted into the material. Apparently, this electron becomes a free carrier. Negative charge on hydrogen in case of the V_O configuration can be explained by the F-center presence at the V_O site.

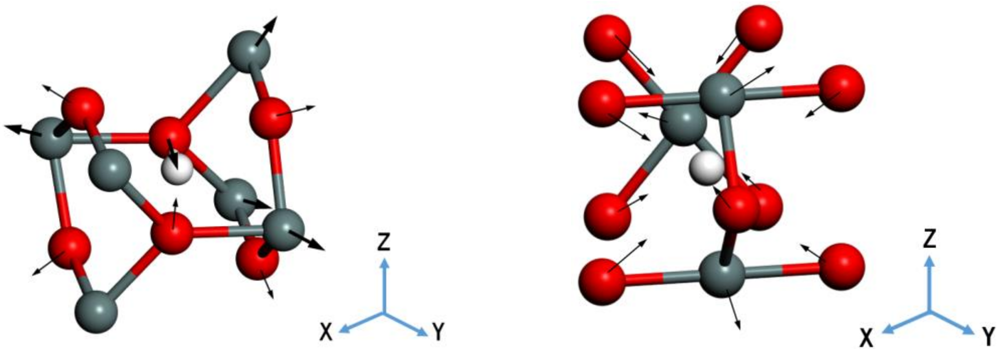

(a) (b)

Figure 4.6. Atomic displacements in SnO_2 crystal if hydrogen atom is situated at (a) the P_1 site and (b) within the oxygen vacancy. The thickness of the arrows give an idea of the magnitude of the displacements. White, red and blue spheres stand for hydrogen, oxygen and tin atoms, respectively.

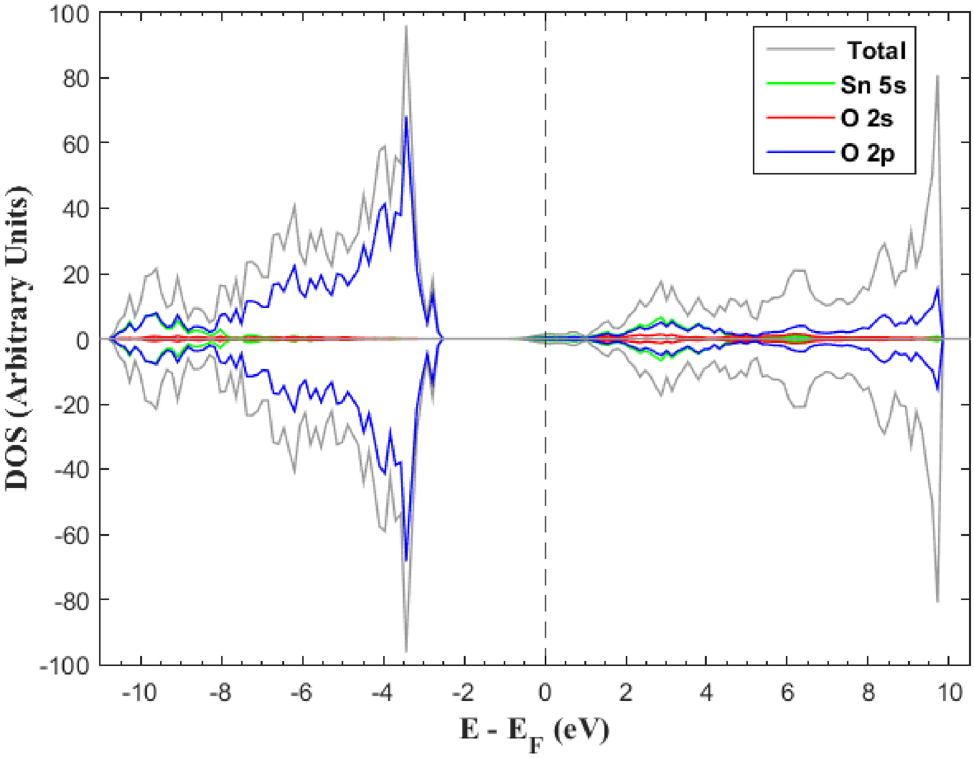

Figure 4.7. DFT+U computed total and partial DOS for SnO2+H configuration if the H atom is at the site P1. The grey dashed line marks the EF. Integration from the bottom of the CB up to EF represents the value of free-carrier density: n. DOS patterns for the rest of the group SnO2+H configurations are practically identical.

4.3. Transition of the conductivity in SnO_2 from n-type to p-type

The p-type electrical conductivity in the SnO_2 was reproduced by codoping[6] the n-doped crystal (from section 4.2.1) with low concentrations of Al and N atoms. The cooping has been achieved by replacing one host O atom by the N impurity and four Sn atoms by four Al impurities, respectively. The computational values for the dopant concentrations, shown in Table 4.3, were kept as close as possible to the corresponding experimental values (X-ray diffraction (XRD) and X-ray photoelectron spectrometer (XPS) measurements detailed below).

Table 4.3. Impurity doping rates used in the computational and experimental procedures.

Dopant	Theoretical (mol%)	Experiment (mol%)
N	1.56	1.94
Al	12.48	14.65

Six different defect configurations have been considered by taking into account various relative positions between the intrinsic defects and dopants. The most stable configuration is shown in Figure 4.8; its POSCAR files can be found in Appendix A.4.

From a microscopic standpoint it can be observed that the incorporation of Al and N atoms into the crystallographic lattice produces a perturbation on the defect-neighbouring atoms situated within a radius of up to 2.96 Å from the corresponding point defect. Bader population analysis (Table 4.4) shows that the charges on Al atoms (Q_1) are bigger than those of the Sn atoms (Q_0), which are replaced in the process of codoping. The charges for O atoms (Table 4.5) before and after codoping differ as well. It is possible to notice that oxygens in vicinity of impurity atoms become more negative. That is why we suggest the augmentation of ionic character in the chemical bonding within the defective region and Coulomb electrostatic origin for the atomic movements, especially between the Al and O atoms. Similar results regarding the atomic shifts have been recently obtained also for the Ga-doped SnO_2 (Stashans, Puchaicela et al. 2014). In case of N impurity (Table 4.5), atomic charge on nitrogen is smaller compared to the charge of the replaced O atom before codoping. This apparently leads to a smaller

---

[6] Simultaneous doping of a material.

Coulombic attraction between the N impurity and its neighbouring atoms resulting in their defect-outward movements.

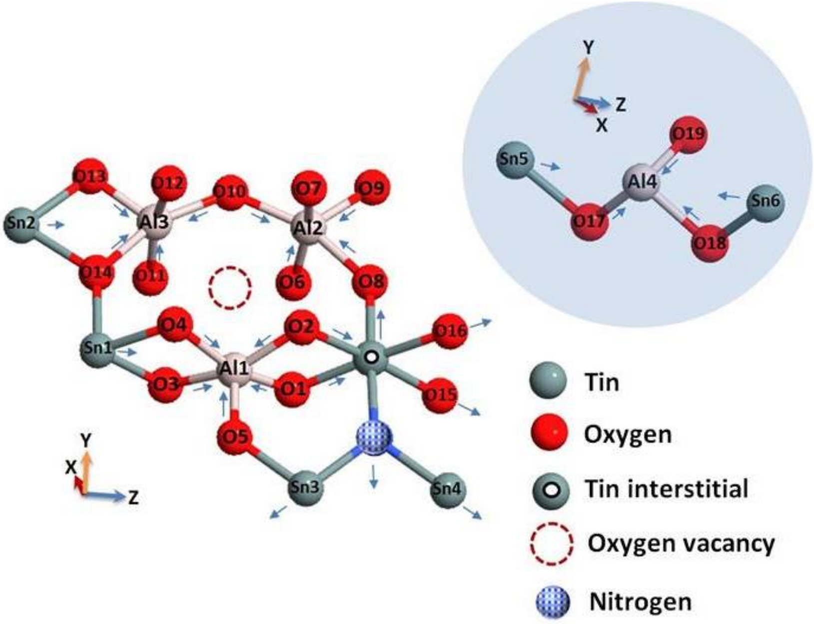

Figure 4.8. Atomic displacements in the SnO_2 crystalline lattice in the neighbourhood of the N and Al dopants. Al-nearest atoms have a tendency to move towards the closest Al impurity. N-nearby atoms tend to move outward with respect to the N atom.

Table 4.4. Difference in atomic charges between n-type crystal (Q_0) containing host Sn and O atoms and p-type crystal (Q_1) containing incorporated impurities of Al (instead of Sn) and N (instead of O) atoms, respectively.

Atom	Q_0 (e)	Q_1 (e)
Al (1)	2.12	2.46
Al (2)	2.01	2.47
Al (3)	2.04	2.46
Al (4)	2.45	2.48
N	-1.23	-1.06

Total DOS for codoped SnO_2 is shown in Figure 4.9. As one can see, codoping generates unoccupied band at the upper VB maximum implying the occurrence of free holes within the upper VB region. Free holes contribute towards the p-type conductivity and the solid can be treated as a polarizable continuum with conduction holes moving through the lattice. Thus the conductivity switch from n-type to p-type occurs in the SnO_2 material.

Table 4.5. Atomic charges obtained by the Bader population analysis for the perfect (Q_1) and p-doped (Q_2) SnO_2 crystals, respectively. The atomic displacements (DR) with respect to the closest impurity atom are also shown. Negative atomics displacements stand for the defect-inward movements. The atomic numeration corresponds to the one indicated in Figure.

Defect	**Q_1 (e)**	**Q_2 (e)**	**ΔR (Å)**	**Nearby atoms**
Al (1)	-1.21	-1.34	-0.14	O (1)
	-1.22	-1.33	-0.14	O (2)
	-1.21	-1.32	-0.13	O (3)
	-1.22	-1.32	-0.13	O (4)
	-1.23	-1.34	-0.26	O (5)
	2.45	2.46	-0.11	Sn (1)
Al (2)	-1.23	-1.31	-0.16	O (6)
	-1.22	-1.31	-0.15	O (7)
	-1.20	-1.32	-0.12	O (8)
	-1.22	-1.35	-0.25	O (9)
	-1.21	-1.42	-0.15	O (10)
Al (3)	-1.21	-1.42	-0.16	O (10)
	-1.23	-1.34	-0.16	O (11)
	-1.22	-1.29	-0.13	O (12)
	-1.24	-1.31	-0.26	O (13)
	-1.21	-1.28	-0.12	O (14)
	2.45	2.46	0.05	Sn (1)
	2.45	2.46	-0.23	Sn (2)
Al (4)	-1.23	-1.28	-0.08	O (17)
	-1.22	-1.28	-0.13	O (18)
	-1.22	-1.25	-0.07	O (19)
	2.46	2.45	-0.06	Sn (5)
	2.45	2.45	-0.11	Sn (6)
Sn_i	-1.21	-1.34	-0.01	O (1)
	-1.22	-1.33	-0.01	O (2)
	-1.20	-1.32	-0.01	O (8)
	-1.22	-1.23	0.04	O (15)
	-1.23	-1.22	0.04	O (16)
	-	-1.06	-	N
N	2.45	2.38	0.05	Sn (3)
	2.46	2.40	0.04	Sn (4)
	2.45	2.41	0.08	Sn_i

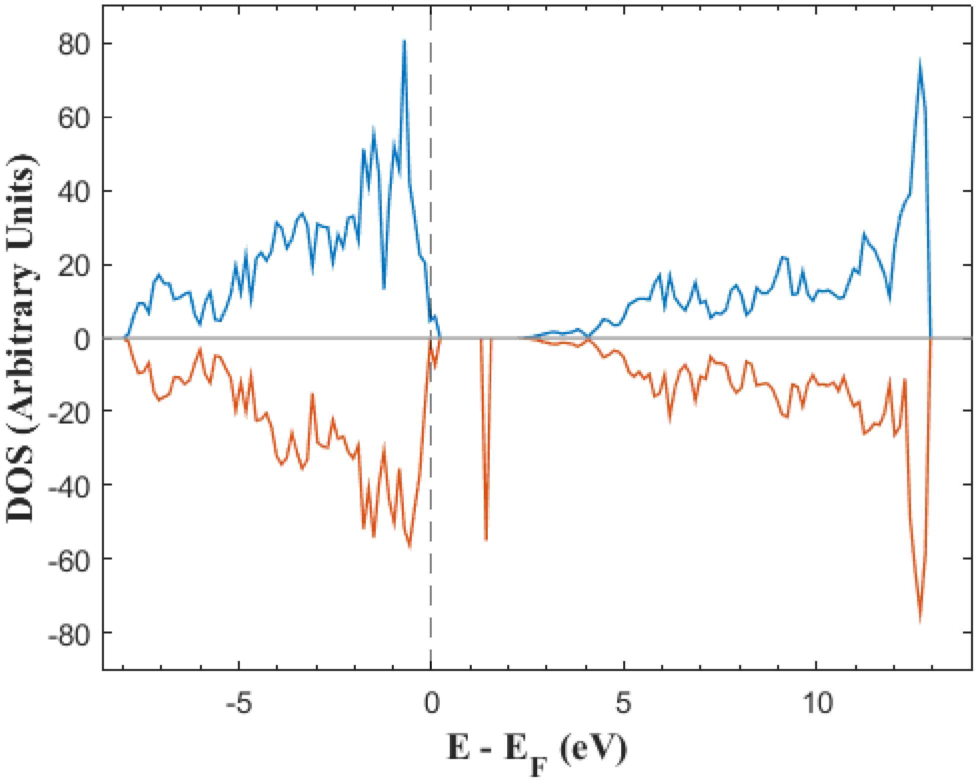

Figure 4.9. Total DOS of SnO_2 endowed with p-type conductivity. The dotted grey line marks the Fermi level (E_F).

In order to fabricate[7] the samples, the targets of 99.99% SnO_2, and 99.95% AlN were used to deposit the undoped SnO_2 and AlN-doped SnO_2 thin films on quartz substrates by sputtering system. A 30 sccm Ar was introduced during the sputtering process with a background pressure of 1.5×10^{-3} Torr. Before sputtering, the targets were pre-sputtered for 10 min. The ultimate thickness of the thin films was fixed to 200 nm. The substrate temperature during sputtering was controlled to be below 50 °C. After the deposition, the as-deposited thin-films were annealed in the N_2 ambient for 30 min at various temperatures. The concentration of Al in Al-doped SnO_2 thin films was examined by the XPS. The XPS spectra analyzed within the present work was at the position of the ion-etching time of 500-s, which is approximate at the middle of the thin films. The crystalline parameters of thin films were investigated by XRD. The resistivity, mobility and the carrier concentrations of the thin films were measured by Hall measurement (Accent HL5500PC).

---

[7] The TFT devices were manufactured by our collaboration team at the National Central University, Jhong-Li in Taiwan.

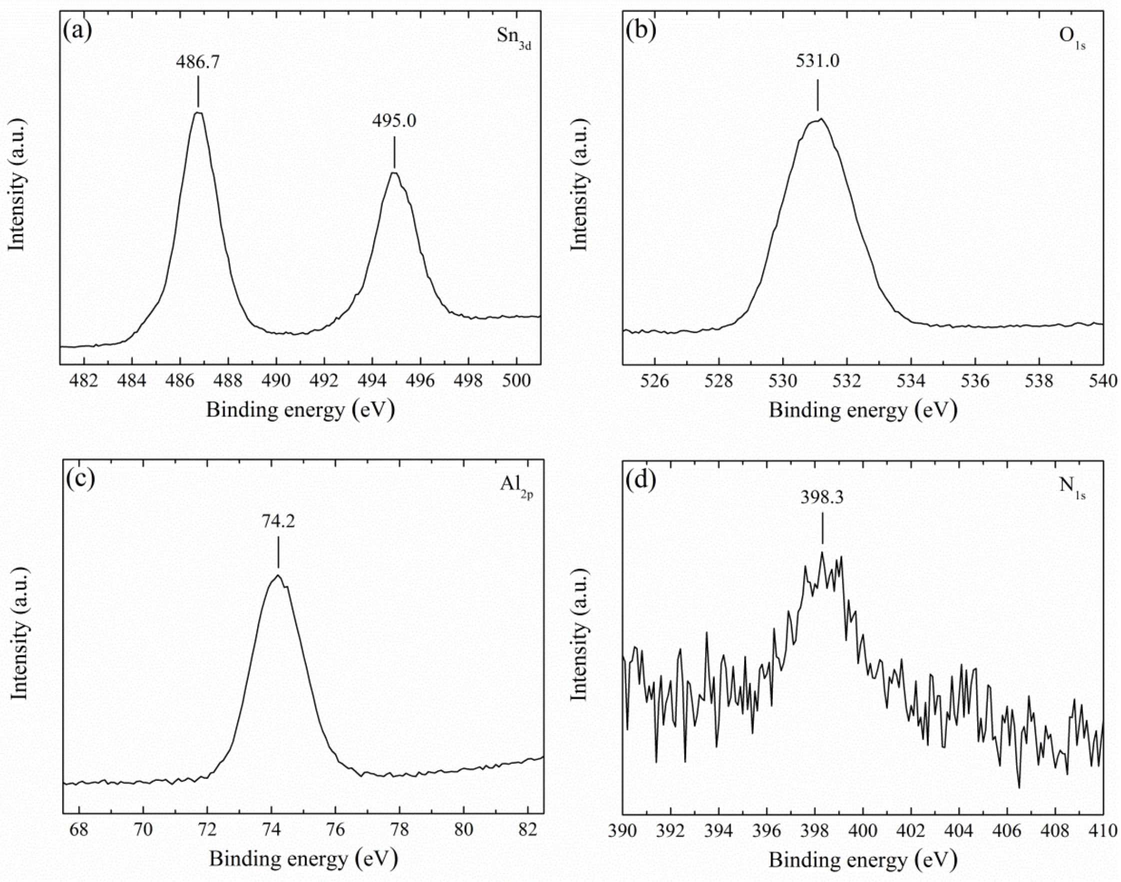

Figure 4.10. XPS spectrum of the (a) Sn 3d, (b) O 1s, (c) Al 2p and (d) N 1s core-level peaks of the AlN-doped SnO_2 (14.65 mol% of Al and 1.94 mol% N) thin films annealed in the N_2 ambient at 450 ºC for 30 min.

Figure 4.10 shows the Sn 3d, O 1s, Al 2p and N 1s core-level peaks of the AlN-doped SnO2 (14.65 mol% of Al and 1.94 mol% of N) thin films annealed in the N_2 ambient at 450 ºC for 30 min. The Sn 3d, O 1s, Al 2p core-level peaks indicate that there is no signal related to the Sn or Al metal, and the Sn and Al cations can be regarded as Sn^{4+} and Al^{3+} oxidation state (Batlle, Hattink et al. 2002) (Rosenberger, Baird et al. 2008, Stefanov, Atanasova et al. 2008). By dividing the peak area by the sensitivity factors for the Sn, O, Al and N, and expressing it as a fraction of the summation of all normalized intensities, the atomic percentage of the elements can be determined. For 450 ºC annealing in the N_2 ambient, we found that only 1.94 mol% of N retain in the SnO_2 thin films, which is far below the atomic percentage of Al, 14.65 mol%. It means that both Al and Sn prefered to bond with O instead of N, and N would outgas during sputtering and annealing process. The unstable Sn–N bond has already been reported by Pan (Pan, Ye et al. 2006). The peak position for the N 1s is located at 398.3 eV. The broad full width at half maximum (FWHM) should be contributed by the formation of N–Sn, Sn–N–Al and N–Al–O chemical bonds (Pan, Ye et al. 2006, Rosenberger, Baird et al. 2008).

Figure 4.11 shows the XRD spectra of the AlN-doped SnO_2 (14.65 mol% of Al and 1.94 mol% of N) thin films annealed in the N_2 ambient at 450 ªC for 30 min. The (110), (101), (207) and (211) peaks of SnO_2 phase with rutile structure could be detected in XRD diffraction patterns without any Al_2O_3 and AlN phase, indicating that the Al and N were incorporated into the tin dioxide lattice.

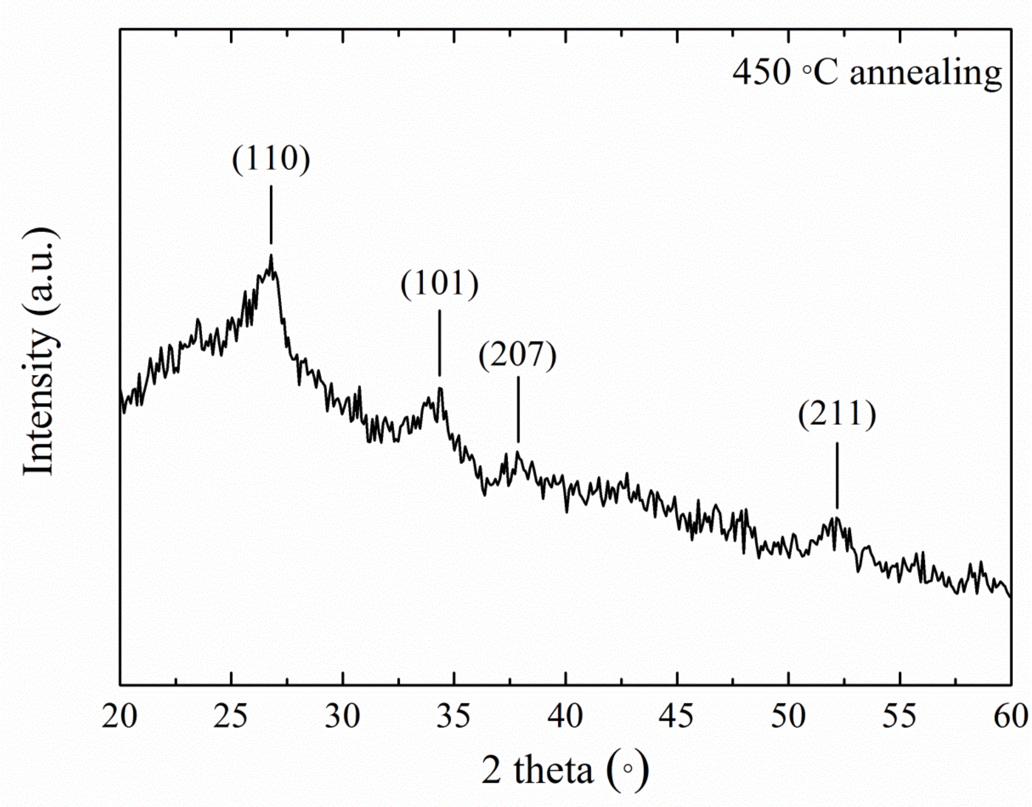

Figure 4.11. XRD spectra of the AlN-doped SnO_2 (14.65 mol% of Al and 1.94 mol% of N) thin films annealed in the N_2 ambient at 450 ºC for 30 min.

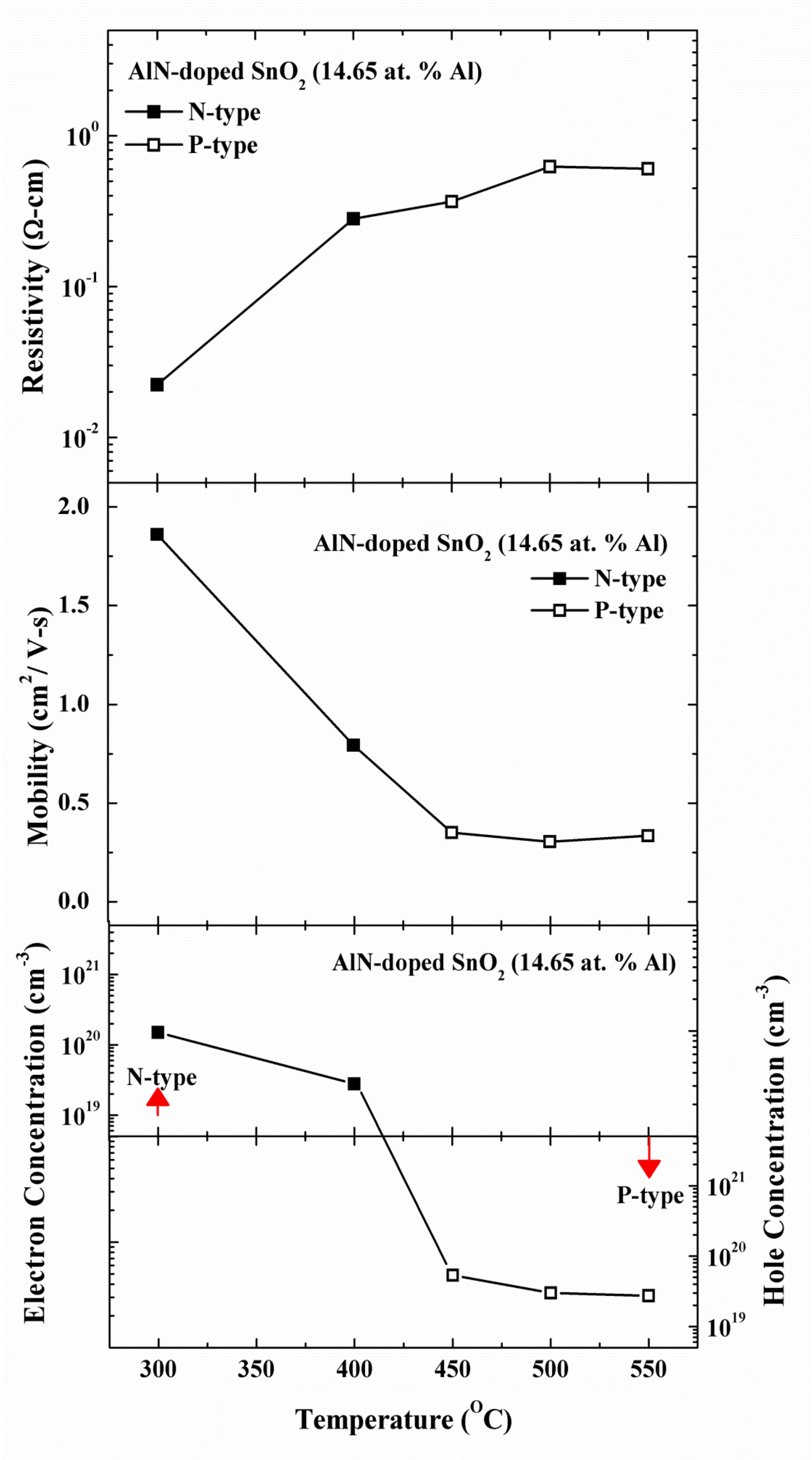

Figure 4.12. The Hall measurement results for electrical properties (carrier concentration, mobility and resistivity) of the AlN-doped SnO_2 (14.65 mol% of Al and 1.94 mol% of N) thin films against the annealing temperature.

Figure 4.12 shows the electrical properties (carrier concentration, mobility and resistivity) of the AlN-doped SnO_2 (14.65 mol% of Al and 1.94 mol% of N) thin films against the annealing temperature. The open and solid markers denote the carrier polarity (p-type or n-type) in the AlN-doped SnO_2 thin films, respectively. From the carrier concentration results shown in the figure, the n-type conduction of the AlN:SnO_2 thin films could be converted into the p-type conduction by annealing at higher temperature (450–550 °C). The tendency of the mobility change with the annealing temperature shown in the figure also confirms the change of carrier polarity from n-type to p-type. With the carrier polarity change to p-type, the mobility of hole carrier is much lower than electron carrier. The 450 °C-annealed p-type AlN-doped SnO_2 thin film has the lowest resistivity ($3.657 \times 10^{-1}\ \Omega \cdot \mathrm{cm}$).

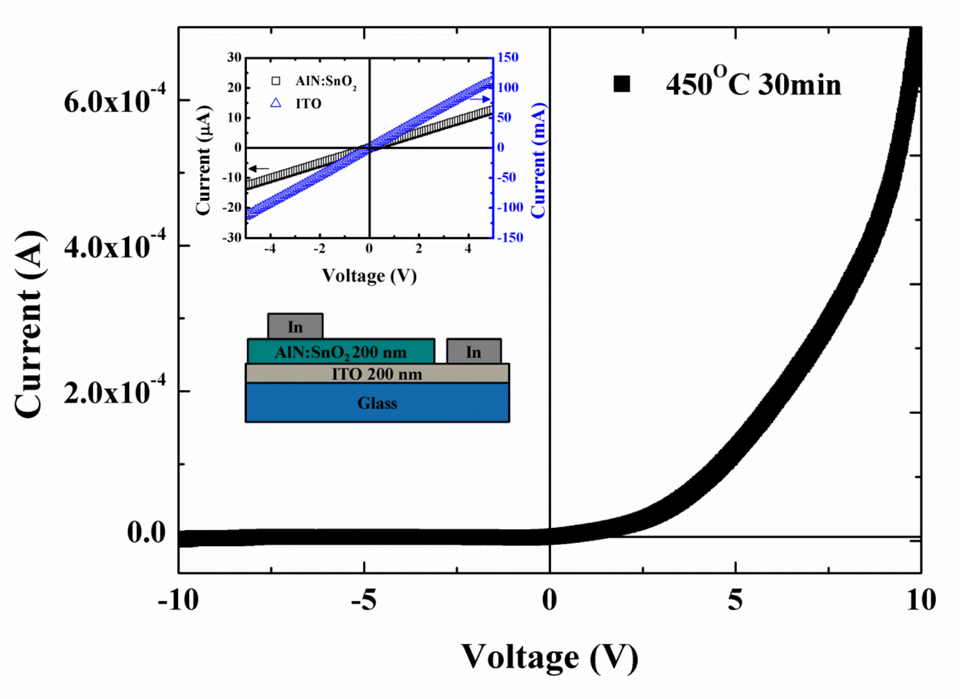

Figure 4.13. I–V curve of the p-type AlN-doped SnO_2/n-ITO p–n junction. The area of the p-type AlN:SnO_2 thin film were defined by the lithography processes.

The p-type AlN:SnO_2 thin films were employed to fabricate p–n junction structure sketched in Figure 4.13. The SnO_2:In_2O_3 thin film was deposited on glass substrate as n-type semiconductor. Both the SnO_2:In_2O_3 and AlN:SnO_2 thin films were deposited by sputter process as 200 nm thickness. A metallic (indium) contacts was deposited over both the n and p side of the junction. The contacts between the In metal and the p-type AlN:SnO_2 and n-type SnO_2:In_2O_3 thin films were confirmed through the ohmic behaviour (I–V curve) in the figure. The distance between the each In metal scheme is 200 μm for the measure of I–V curve shown in Figure 4.13 also shows I–V curve of the AlN:SnO_2/SnO_2:In_2O_3 p–n structure.

Table 4.6. The Seebeck coefficients of the AlN-doped SnO_2 thin films annealed at variety temperature in N_2 ambient for 30 min.

Temperature	**As-dep.**	**300 °C**	**400 °C**	**450 °C**	**500 °C**
S (μV/k)	-79.553	-77.524	-43.785	56.096	51.407

The Seebeck coefficients of the AlN-doped SnO_2 thin films were calculated by the slope of the plots of thermo-emf (E) vs. difference of temperature (T) between the hot and cold junctions at 28 °C. Table 4.6. shows the Seebeck coefficients of the AlN-doped SnO_2 thin films annealed at variety of temperatures in the N_2 ambient for 30 min. It can be observed that the Seebeck coefficient value changes from negative to positive when the annealing temperature is higher than 400 °C. This finding also are in line with the Hall measurement results.

4.4. Electronic properties of defected AGNRs

This section reports the changes underwent by the electrical and structural properties of eleven AGNRs as a distortion was added into the crystalline lattice of the nanoribbons. The study was carried out through a simple TB approach, detailed in Chapter 3.

In accordance with the general convention for AGNRs (Na-AGNR), their widths ($4 \leq N_a \leq 13$) were defined by the number of dimer lines, N_a, across the ribbon (shown in Figure 4.14a) (Son, Cohen et al. 2006, Wang, Ouyang et al. 2008). C atoms at the edges were passivated with H atoms to eliminate the dangling bonds and increase the stability in exchange of a slight change of their electronic properties. The disorder was introduced by placing a SW defect at one edge of each nanostructure (shown in Figure 4.14b). SW defects have been identified to be the most common defects in the sp^2 carbon allotropes due to their low binding energy (Rodrigues, Gonçalves et al. 2011). In order to maintain the crystalline system simple, no curvature[8] was allowed in the atomic structure as the SW transformation took place.

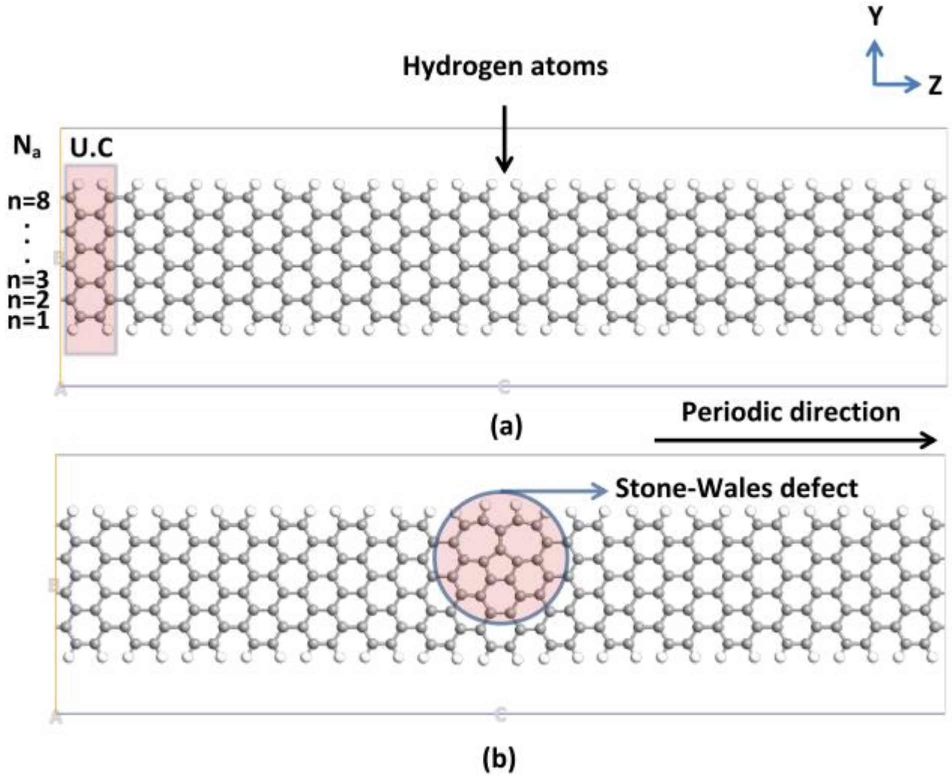

Figure 4.14. Illustrate the atomic structure of an 8-AGNR along with its unit cell repeated 15 times along the periodic direction: (a) pristine structure and (b) with a Stone-Wales defect (shaded region). Carbon atoms at both edges were passivated with H. Gray and white atoms denote C and H, respectively.

Due to quantum confinement[9], AGNRs acquired an E_g, which depends on N_a. These features (shown in Figure 4.15) for pristine ribbons are in good agreement with recently reported calculations (Hancock, Uppstu et al.). As a matter of good practice, to better understand the results, the E_g of the AGNRs were separated into three families: the points forming the envelope of the maxima of the oscillations (family N_a=3m+1), those forming the envelope of the minima of the oscillations (family N_a=3m-1), and the

---

[8] Curvatures in carbon allotropes have been pointed out to cause drastic (still not well known) changes in their electrical and magnetic properties.

[9] Cutting of the graphene sheet into quasi-one dimensional nanostructures with (in this case) armchair edges.

remaining intermediate points (family 3m). The maximum attained E_g (2.6 eV) was observed in a 4-atomic rows pristine AGNR (family 3m+1).

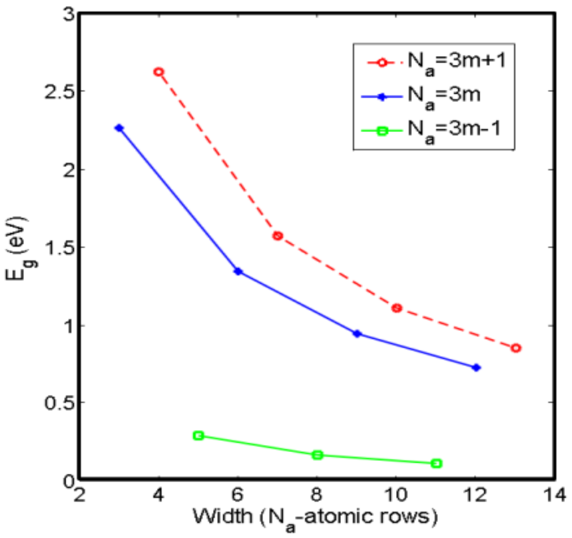

Figure 4.15. The energy gaps of 11 pristine. m is an integer number

The band gap of the AGNRs was calculated by measuring the energy difference between the top of the VB and the bottom of the CB of in the band structure of the AGNR. Figure 4.16 shows the band structure of three AGNRs (Na=5, 6, 7); each belonging to one of the aforementioned families.

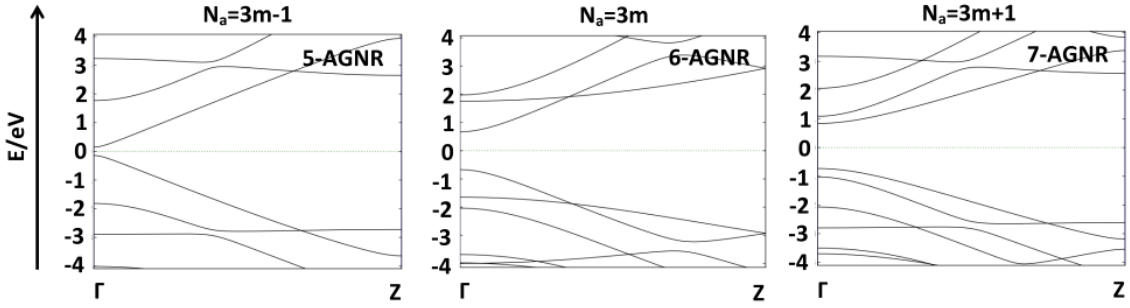

(a) (b) (c)

Figure 4.16. Energy band structure in the *Γ(0,0,0)* → *Z(0,0,1/2)* route for armchair nanoribbon of various widths: (a) $N_a=5$ (b) $N_a=6$ and (c) $N_a=7$. Correspondingly, these three ribbons belong to $N_a=3m-1$, $N_a=3m$, and $N_a=3m+1$ families.

After the introduction of the SW defect inside the AGNR lattices, the inverse relationship continued. Changes triggered by these defects are accounted independently as follows: (i) all ribbons in Na=3m-1 family underwent an increase in their gaps; (ii) families Na=3m+1 and Na=3m endured decrease in their gaps but only in the smallest ribbons (Na=3, 4, 6 and 7), from 10 atomic rows onward their gaps started to increase; (iii) it is also evident that the energy difference among the three families was scaled down; (iv) the maximum improvement achieved on the E_g after the defect insertion was of 53%. Summing up the available data, it is found that the energy gap of 45% of the ribbons increased, 18% remained the same, while 37% was reduced.

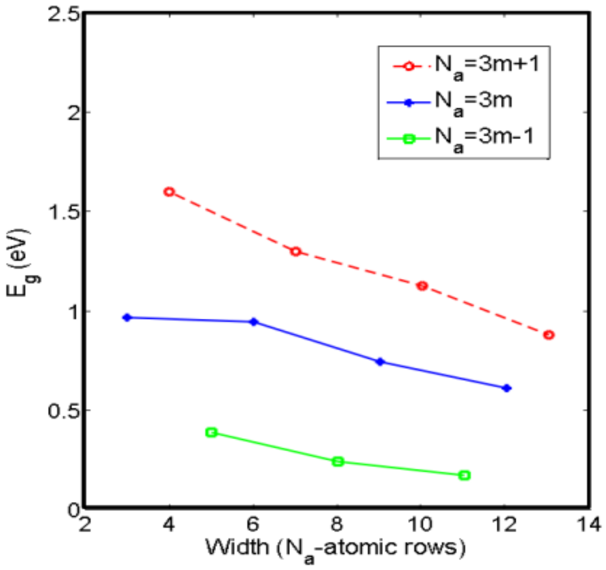

Figure 4.17. The energy gaps of 11 AGNRs structures modified at the edge by a SW defect.

4.5. The influence of multiple cleaning treatments on CVD transferred GFET devices

Although pristine graphene exhibits ambipolar electric field effect, it is sensitive to unintentional doping by species absorbed from the surroundings or residual polymers used during device fabrication (Liu, Liu et al.). This, in turns, causes degradation in the electrical properties of the graphene flake (Jang, Trung et al. 2014). In this section, it is presented a chemical cleaning route capable of clearing out the graphene flake, with only minimal degradation in the electronic properties of the GFET devices.

The GFET devices were fabricated[10] on SiO_2 (300 nm)/silicon wafer[11] following the simple back-gated structure illustrated in Figure 18a. In Figure 18b it is shown an optical image of the device layout; the light regions are Ti/Ag contacts and the dark region is the graphene flake used as bulk channel in the GFET. A detailed explanation of the manufacturing process (resist deposition, transference of the pattern, and contacts evaporation) can be found in Appendix B.

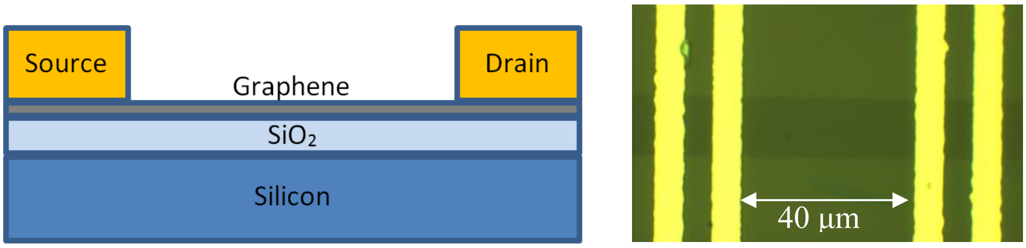

Figure 4.18. (a) Schematic cross section of back-gated GFET device, (b) optical micrograph of a GFET device (top); channel width is W ≈ 20 µm and channel length is L≈ 40 µm.

The cleaning process used on the GFET devices was the following:

Samples were immersed for 1 hour in a 40 ºC bath of 1165. Following, another 40 ºC bath of 1165 for 30 mins. Then, the samples were rinsed with acetone. Finally an IPA dried with N2. This process will be referred to as CCP in the rest of this disseratation.

The first hints toward demonstrating the capability of the cleaning process were obtained from the micrographic images (at 100 x magnification) shown in Figure 4.19. As one can notice, a big deal of debris was removed from the graphene surface after the cleaning process took place.

---

[10] The GFET devices were manufactured at the Tyndall National Institute (Ireland).

[11] Microfabrication of graphene devices used in many experimental studies currently relies on the fact that graphene crystallites can be visualized using optical microscopy if prepared on top of Si wafers with a certain thickness of SiO_2 Blake, P., E. Hill, A. C. Neto, K. Novoselov, D. Jiang, R. Yang, T. Booth and A. Geim (2007). "Making graphene visible." Applied Physics Letters **91**(6): 063124.. A 300nm layer is of common practice to use.

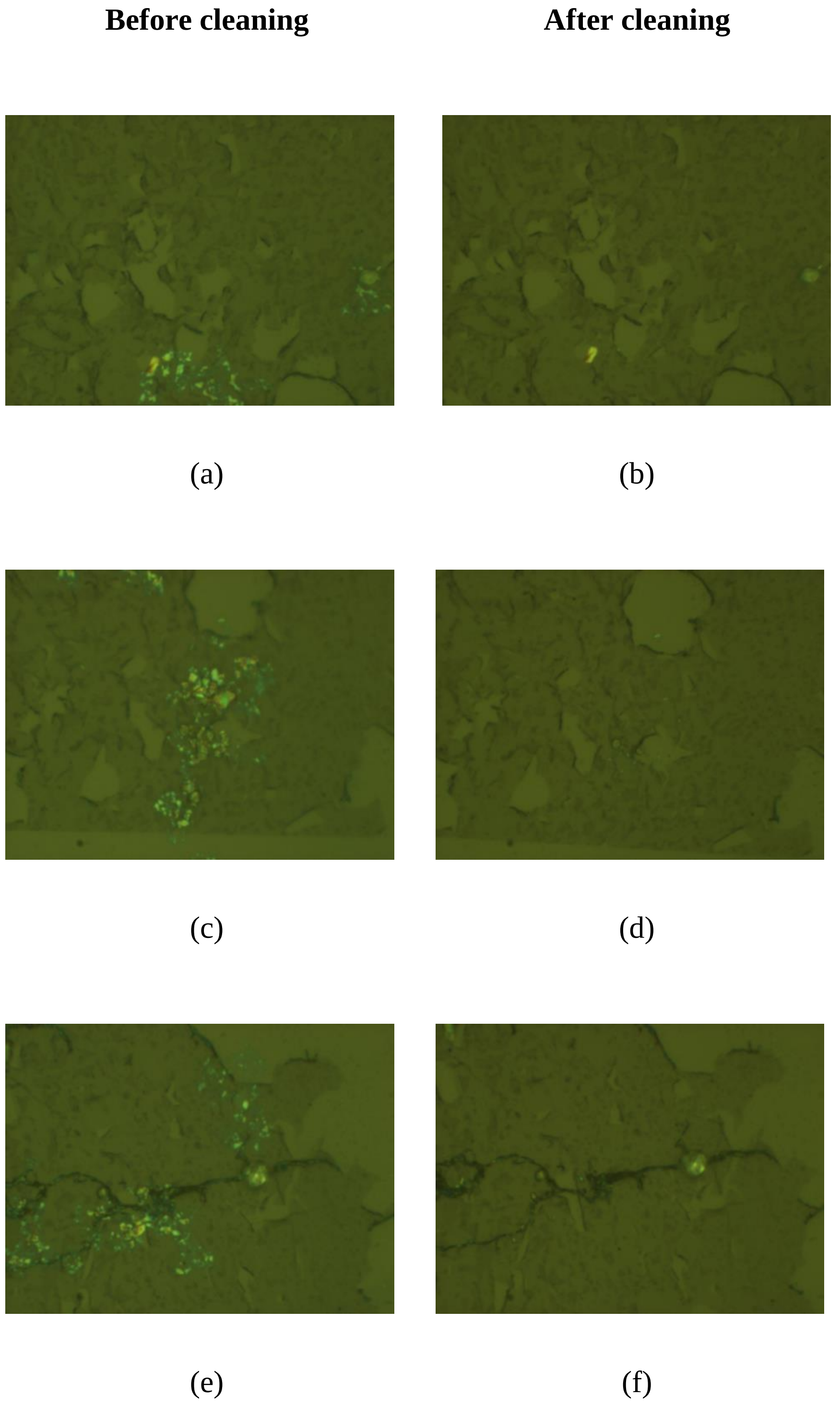

Figure 4.19. Tracks the changes endured by the graphene flake before (left column) and after (right column) applying the chemical cleaning process on the devices.

Following, Raman spectroscopy (Renishaw inVia Raman microscope, 532 nm laser wavelength, 100 × objective) was used to develop a qualitative analysis of the graphene inside the GFET devices. To do this, two spectra (Figure 4.20a) were taken at approximately the same spot before and after the samples were cleaned. The three peaks in the spectra ((i) the D peak (defects) around 1350 cm^{-1}, (ii) the G peak (in-plane vibration of sp^2 carbon atoms) around 1580 cm^{-1}, and (iii) the 2D peak (second harmonic of the D band) around 2685 cm^{-1}) indicated that graphene was monolayer. The AFM images (Veeco Dimension 3100), also taken at approximately the same spot, confirm this evidence (Figure 4.20b).

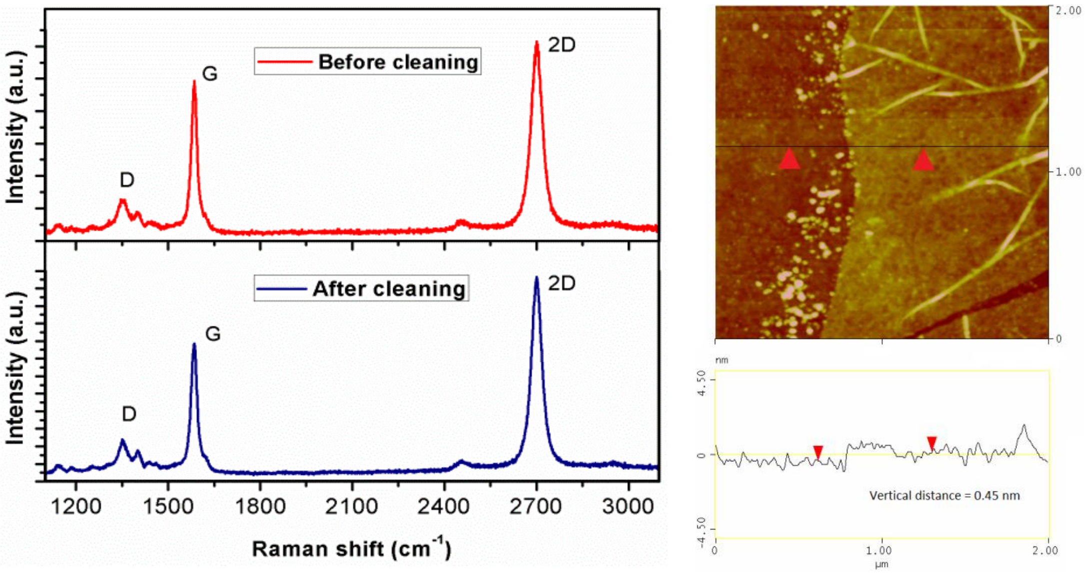

(a)

(b)

Figure 4.20. (a) Raman spectrum of graphene before (top) and after (bottom) the cleaning process. (b) AFM image (top) of the graphene inside the GFET structure and its line profile (bottom). The vertical distance of 0.45 nm indicates that graphene is monolayer.

Disorder in graphene was quantified by analyzing the intensity ratio between the disorder-induced D band and the Raman allowed G band (I_D/I_G); higher I_D/I_G values indicate more defects in graphene (Liang, Sperling et al. 2011, Liu, Notarianni et al. 2013). Table 4.7 lists the I_D/I_G ratio at four locations inside the wafer. Improvements of the graphene layer can be clearly appreciated by comparing values in both columns.

Table 4.7. I_D/I_G ratio which quantifies the disorder in the graphene layer before and after the surface was cleared up.

Location	Before	After
1	0,26	0,22
2	1,38	1,10
3	0,38	0,41
4	1,04	0,70

To further understand the effects of the cleaning process on the graphene layer, field-effect measurements were conducted. Three-terminal measurements were performed, with the Si substrate as the back-gate (B) and the metal electrodes as the source (S) and drain (D). All the measurements were performed in ultra-high vacuum (10^{-7} pascal) and at room temperature (300ºK) using a HP4140B semiconductor parameter analyzer. Back-gate voltage sweeps, in the interval (-15V, 15V), were performed at constant low drain bias (10 mV).

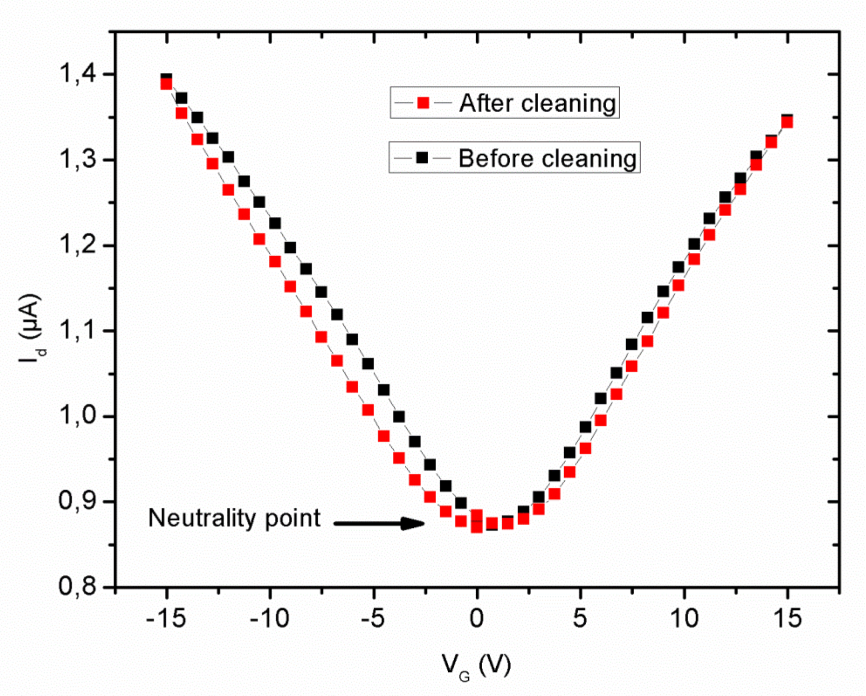

Figure 4.21. Transfer characteristic I_{DS}-V_{GS} of the device before and after the cleaning process took place. A minimum I_{DS} corresponds to the charge neutrality point or Dirac point (V_{GS}^{*}~0.75V)..

Figure 4.21 shows the transfer characteristic of one of the devices before and after the wafer was cleaned. This transfer characteristic is common to all GFET devices, in which, the minimum I_{DS}, corresponds to the charge neutrality point (NP). A positive charge NP indicates that the graphene is unintentionally p-doped[12]. Likewise, a negative charge NP indicates that the graphene is unintentionally n-doped. Only p-doped graphene appeared in the sample investigated here.

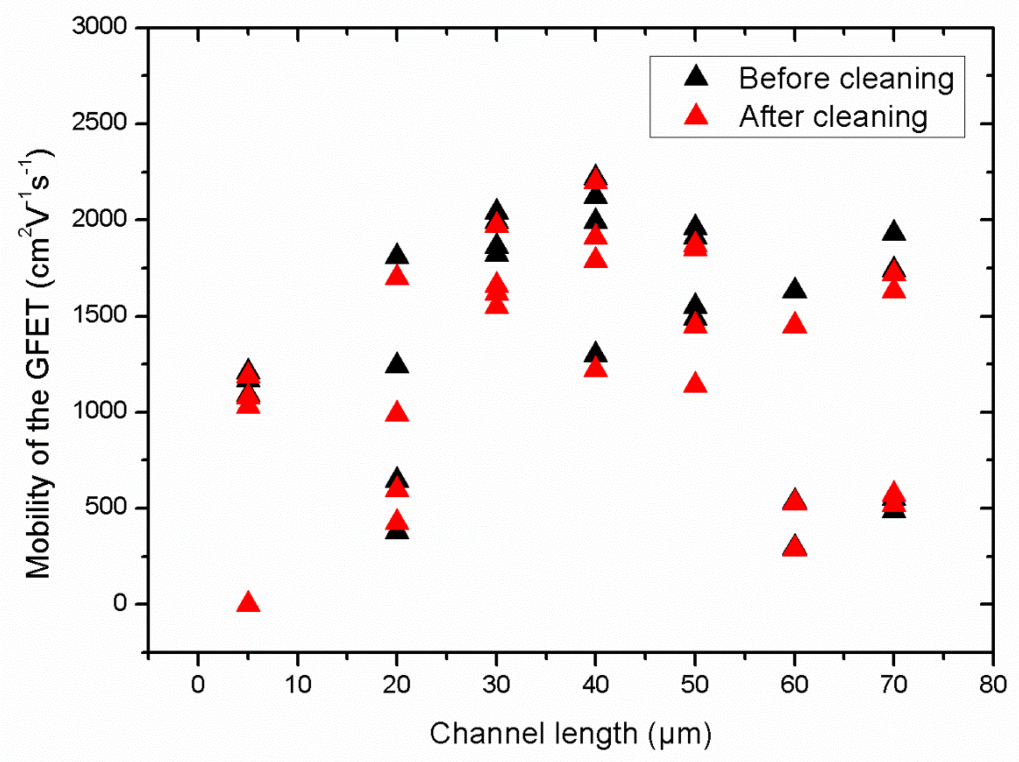

Figure 4.22. Mobility values for different GFET devices. Back-gate voltage sweeps, in the interval (-15V, 15V), were performed at constant low drain bias (10 mV). The widths of their channels were 20 um.

The relationship between the channel length and the electron mobility (μ) can be found in Figure 4.22. In order to render easier the analysis of the results, only the transistors whose widths were equal to 20 um were taken into account. Their channel

---

[12] The formation of weak C-O bonds between graphene and SiO_2 has been proven to support p-type conductivity in graphene by transfer of charge from the carbon in graphene to the oxygen of the SiO_2.

length ranged from 5 µ m to 70 µ m. The results indicate that the mobility values stayed over 1000 $cm^2V^{-1}s^{-1}$. The highest electron mobility value was 2200 $cm^2v^{-1}s^{-1}$ (40 um domain); this confirms the success of the chemical cleaning process used in this investigation.

Chapter 5. Summary and conclusions

5.1. Summary

In this dissertation, focus was laid on the electronic and structural properties of SnO_2 and graphene from the theoretical point of view. Figure 5.1 presents a diagram with a concise visual summary of the main topics addressed in this investigation. The two leftmost branches of the diagram account for the work done on the SnO_2 material; likewise, the two rightmost branches account for the work done on the graphene material. The experimental studies conducted, to a big extent, validated and/or boosted the theoretical findings.

On the one hand, the n-type and p-type conductivity in SnO_2 were reproduced through the DFT + *U* approach as it is implemented in the VASP. It was demonstrated that the n-type conductivity can be achieved through two different (and sometimes contradictory) schemes, involving oxygen vacancies, interstitial and substitutional atoms into the SnO_2 lattice. In particular, configurations SnO_2+V_O+Sn_i, SnO_2+V_O+H, and SnO_2+H were extensively studied. The n-to-p conductivity transition was obtained throughout the incorporation of low concentrations of nitrogen and aluminum atoms into the n-type SnO_2 lattice; nitrogen substitution onto an oxygen (1.56 mol%) atomic sites and Al substitution onto tin (12.48 mol%) atomic sites. Their experimental counterparts were 14.65 mol% and 1.94 mol%, respectively. Furthermore, fully transparent thin film transistors devices were fabricated and characterized through Hall-measurements, XRD, and XPS spectroscopy.

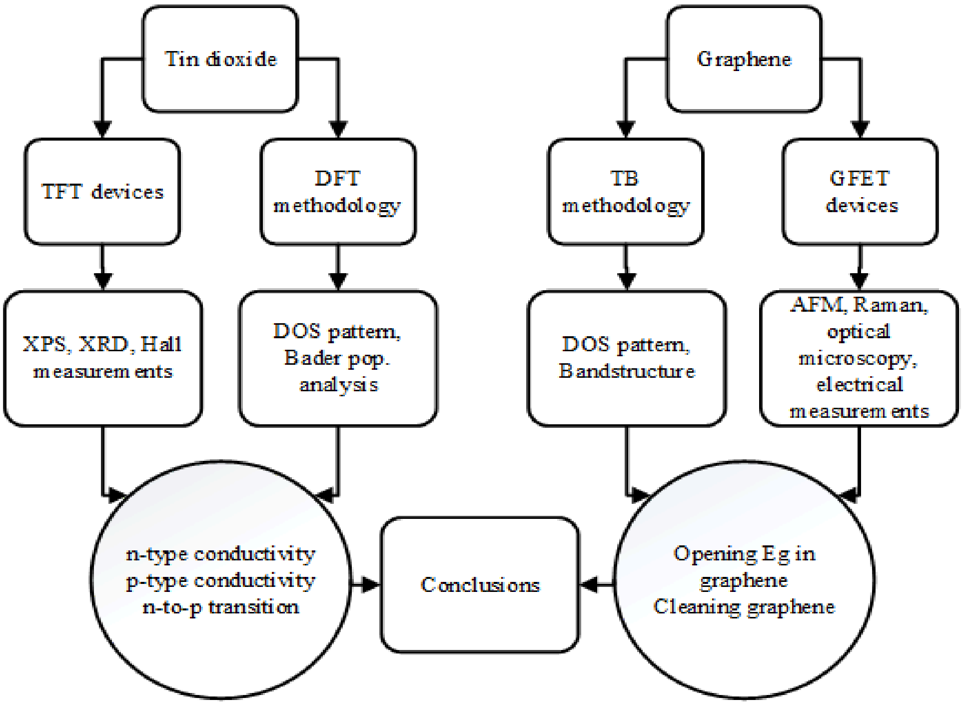

Figure 5.1. Block diagram which summarizes the research done in this dissertation.

On the other hand, the theoretical investigation on graphene was carried out (primarily) by using the TB approach as it is implemented in ATK. The changes were studied, which underwent by the electrical and structural properties of eleven AGNRs as distortions (in the form of SW defects) being introduced at the edges of the AGNR lattices. It was found that distortion at the edges of these nanoallotropes can cause an extra opening of the band gap, in addition to that of quantum confinement. From the experimental standpoint, a study of the influence of multiple cleaning treatments on CVD transferred GFET devices was also reported. Debris from residual polymers that appeared during device fabrication was swept off the graphene surface without significantly degrading the electronic properties of the graphene flake.

Bearing this in mind, I proceed to list the conclusions reached in this investigation.

5.2. Conclusions for SnO_2

From the theoretical point of view it can be concluded that: (i) oxygen vacancies in the SnO_2 structure do not generate by themselves free electrons in the material; (ii) the collective action of oxygen vacancies and tin interstitials are needed to create free electrons at the bottom of the CB and thus to produce the n-type conductivity in SnO_2; (iii) H atoms can also spark n-type conductivity in SnO_2 (iv) p-type conductivity can be achieved when the codoping of n-type material with Al and N impurities at specific concentrations.

From the experimental point of view it can be concluded that: (i) the broad width of N 1s core-level peak shows the formation of N–Sn, Sn–N–Al and N–Al–O chemical bonds; (ii) resistivies as low as 3.657 x10-1 Ω cm for p-type AlN-codoped SnO_2 (14.65 mol% of Al) thin film can be achieved with carrier concentration as high as 4.858 x 10^{19} cm^{-3}; and (iii) The I–V curve of p–n structure and Seebeck coefficients of the AlN-codoped SnO_2 thin films were both corresponding to the Hall measurement results.

5.3. Conclusions for graphene and AGNRs

From the theoretical point of view it can be concluded that: (i) the quantum confinement alone leads to a clear inverse dependence between the energy gap and the width of pristine nanoribbons, (ii) distortion at the edges of the ribbons produce an extra opening of the energy band value of the AGNRs, (iii) families Na=3m+1 and Na=3m endured decrease in their gaps but only in the smallest ribbons (Na=3, 4, 6 and 7), from 10 atomic rows onward their gaps started to increase.

From the experimental point of view it can be concluded that: (i) graphene inside a GFET structure displays ambipolar electric field effect, (ii) graphene inside a GFET structure is sensitive to unintentional doping by species absorbed from the surrounding or residual polymers used during device fabrication, which in turns causes degradation in the electrical properties of the graphene flake, (iii) the chemical cleaning process sweeps off the debris of the graphene surface without significantly degrading the electronic properties of the graphene flake; this was verified through: AFM, Raman, micrograph images and field effect measurements, and (iv) electron mobilities of up to 2200 $cm^2V^{-1}s^{-1}$ at room temperature can be obtained through the fabrication and cleaning process exploited here.

References

Ahmed, S. F., S. Khan, P. Ghosh, M. Mitra and K. Chattopadhyay (2006). "Effect of Al doping on the conductivity type inversion and electro-optical properties of SnO2 thin films synthesized by sol-gel technique." Journal of sol-gel science and technology **39**(3): 241-247.

áLe Blevennec, G. (1997). "First-principles investigations of the electronic, optical and chemical bonding properties of SnO_2." Journal of Materials Chemistry **7**(12): 2547-2550.

Allen, M. J., V. C. Tung and R. B. Kaner (2009). "Honeycomb carbon: a review of graphene." Chemical reviews **110**(1): 132-145.

Arlinghaus, F. (1974). "Energy bands in stannic oxide (SnO 2)." Journal of Physics and Chemistry of Solids **35**(8): 931-935.

Bagheri-Mohagheghi, M.-M. and M. Shokooh-Saremi (2004). "Electrical, optical and structural properties of Li-doped SnO2 transparent conducting films deposited by the spray pyrolysis technique: a carrier-type conversion study." Semiconductor science and technology **19**(6): 764.

Barone, V., O. Hod and G. E. Scuseria (2006). "Electronic structure and stability of semiconducting graphene nanoribbons." Nano letters **6**(12): 2748-2754.

Batlle, X., B. J. Hattink, A. Labarta, J. J. Åkerman, R. Escudero and I. K. Schuller (2002). "Quantitative x-ray photoelectron spectroscopy study of Al/AlOx bilayers." Journal of applied physics **91**(12): 10163-10168.

Blake, P., E. Hill, A. C. Neto, K. Novoselov, D. Jiang, R. Yang, T. Booth and A. Geim (2007). "Making graphene visible." Applied Physics Letters **91**(6): 063124.

Blöchl, P. E. (1994). "Projector augmented-wave method." Physical Review B **50**(24): 17953.

Borges, P. D., L. M. Scolfaro, H. W. L. Alves and E. F. da Silva Jr (2010). "DFT study of the electronic, vibrational, and optical properties of SnO2." Theoretical Chemistry Accounts **126**(1-2): 39-44.

Bruce, D. W., D. O'Hare and R. I. Walton (2011). Low-dimensional solids, John Wiley & Sons.

Cao, C., L. N. Chen, D. Zhang, W. R. Huang, S. S. Ma and H. Xu (2012). "Electronic properties and conductance suppression of defected and doped zigzag graphene nanoribbons." Solid State Communications **152**(1): 45-49.

Castro, E. V., K. Novoselov, S. Morozov, N. Peres, J. L. Dos Santos, J. Nilsson, F. Guinea, A. Geim and A. C. Neto (2007). "Biased bilayer graphene: semiconductor with a gap tunable by the electric field effect." Physical Review Letters **99**(21): 216802.

Charlier, J.-C., X. Blase and S. Roche (2007). "Electronic and transport properties of nanotubes." Reviews of modern physics **79**(2): 677.

Chauhan, J. and J. Guo (2010). Atomistic simulation of graphene nanoribbon tunneling transistors. Nanoelectronics Conference (INEC), 2010 3rd International, IEEE.

Chauhan, S. S., P. Srivastava and A. K. Shrivastava (2013). "Band gap engineering in doped graphene nanoribbons: An ab initio approach." Solid State Communications **154**: 69-71.

Chen, Y., D. Bagnall, H.-j. Koh, K.-t. Park, K. Hiraga, Z. Zhu and T. Yao (1998). "Plasma assisted molecular beam epitaxy of ZnO on c-plane sapphire: growth and characterization." Journal of Applied Physics **84**(7): 3912-3918.

Chen, Z., D. Pan, Z. Li, Z. Jiao, M. Wu, C.-H. Shek, C. L. Wu and J. K. Lai (2014). "Recent advances in tin Dioxide materials: some developments in thin films, nanowires, and nanorods." Chemical reviews **114**(15): 7442-7486.

Cheng, Z., Q. Li, Z. Li, Q. Zhou and Y. Fang (2010). "Suspended graphene sensors with improved signal and reduced noise." Nano letters **10**(5): 1864-1868.

Choi, Y.-J., I.-S. Hwang, J.-G. Park, K. J. Choi, J.-H. Park and J.-H. Lee (2008). "Novel fabrication of an SnO2 nanowire gas sensor with high sensitivity." Nanotechnology **19**(9): 095508.

Cooper, D. R., B. D’Anjou, N. Ghattamaneni, B. Harack, M. Hilke, A. Horth, N. Majlis, M. Massicotte, L. Vandsburger and E. Whiteway (2012). "Experimental review of graphene." ISRN Condensed Matter Physics **2012**.

Coutts, T. J., T. O. Mason, J. Perkins and D. S. Ginley (1999). Transparent conducting oxides: status and opportunities in basic research. Photovoltaics for the 21st Century: Proceedings of the International Symposium, The Electrochemical Society: Philadelphia, PA, USA.

Deepak, S., M. Manoharan and H. Mizuta (2011). Transport characteristics of nanoconstricted graphene with and with out point defects. International Conference on Nanoscience, Engineering and Technology (ICONSET 2011).

Dresselhaus, M. S. and P. T. Araujo (2010). "Perspectives on the 2010 Nobel Prize in physics for graphene." ACS nano **4**(11): 6297-6302.

Dubois, S.-M., Z. Zanolli, X. Declerck and J.-C. Charlier (2009). "Electronic properties and quantum transport in Graphene-based nanostructures." The European Physical Journal B **72**(1): 1-24.

Dubois, S. M. M., Z. Zanolli, X. Declerck and J. C. Charlier (2009). "Electronic properties and quantum transport in Graphene-based nanostructures." The European Physical Journal B **72**(1): 1-24.

Dumlich, H. and S. Reich (2010). "Chirality-dependent growth rate of carbon nanotubes: A theoretical study." Physical Review B **82**(8): 085421.

Dutta, S. and S. K. Pati (2010). "Novel properties of graphene nanoribbons: a review." Journal of Materials Chemistry **20**(38): 8207-8223.

Edwards, P. P., A. Porch, M. O. Jones, D. V. Morgan and R. M. Perks (2004). "Basic materials physics of transparent conducting oxides." Dalton transactions(19): 2995-3002.

Ellmer, K. (2012). "Past achievements and future challenges in the development of optically transparent electrodes." Nature Photonics **6**(12): 809-817.

Facchetti, A. and T. J. Marks (2010). "Transparent electronics." From Synthesis to Applications, Wiley, Chichester, UK.

Faez, R. and S. Barami (2013). Spin effect on band structure of zigzag and armchair graphene nanoribbones with Stone-Wales defect. Electrical Engineering (ICEE), 2013 21st Iranian Conference on, IEEE.

Fortunato, E., D. Ginley, H. Hosono and D. C. Paine (2007). "Transparent conducting oxides for photovoltaics." Mrs Bulletin **32**(03): 242-247.

Fujita, S. and A. Suzuki (2013). Electrical conduction in graphene and nanotubes, John Wiley & Sons.

Gamard, A., B. Jousseaume, T. Toupance and G. Campet (1999). "New fluorinated stannic compounds as precursors of F-doped SnO2 materials prepared by the sol-gel route." Inorganic chemistry **38**(21): 4671-4679.

Geim, A. K. and K. S. Novoselov (2007). "The rise of graphene." Nature materials **6**(3): 183-191.

Georgiou, T., R. Jalil, B. D. Belle, L. Britnell, R. V. Gorbachev, S. V. Morozov, Y.-J. Kim, A. Gholinia, S. J. Haigh and O. Makarovsky (2013). "Vertical field-effect transistor based on graphene-WS2 heterostructures for flexible and transparent electronics." Nature nanotechnology **8**(2): 100-103.

Glaeser, W. (1993). Alkaline batteries containing a zinc powder with indium and bismuth, Google Patents.

Godinho, K. G., A. Walsh and G. W. Watson (2008). "Energetic and electronic structure analysis of intrinsic defects in SnO2." The Journal of Physical Chemistry C **113**(1): 439-448.

Gordon, R. G. (2000). "Criteria for choosing transparent conductors." MRS bulletin **25**(08): 52-57.

Goyal, D., C. Agashe, B. Marathe, M. Takwale and V. Bhide (1993). "Effect of dopant incorporation on structural and electrical properties of sprayed SnO2: Sb films." Journal of applied physics **73**(11): 7520-7523.

Greiner, W. (1985). Quantum electrodynamics of strong fields, Springer.

Han, M. Y., B. Özyilmaz, Y. Zhang and P. Kim (2007). "Energy Band-Gap Engineering of Graphene Nanoribbons." Physical Review Letters **98**(20).

Hancock, Y. (2011). "The 2010 Nobel Prize in physics—ground-breaking experiments on graphene." Journal of Physics D: Applied Physics **44**(47): 473001.

Hancock, Y., A. Uppstu, K. Saloriutta, A. Harju and M. Puska (2010). "Generalized tight-binding transport model for graphene nanoribbon-based systems." Physical Review B **81**(24): 245402.

Harris, G. L., P. Zhou, M. He and J. B. Halpern (2001). Semiconductor and photoconductive GaN nanowires and nanotubes. Lasers and Electro-Optics, 2001. CLEO'01. Technical Digest. Summaries of papers presented at the Conference on, IEEE.

Henkelman, G., A. Arnaldsson and H. Jónsson (2006). "A fast and robust algorithm for Bader decomposition of charge density." Computational Materials Science **36**(3): 354-360.

Hirsch, A. (1994). The chemistry of the fullerenes, Wiley Online Library.

Hirsch, A. (2009). "Unzipping carbon nanotubes: a peeling method for the formation of graphene nanoribbons." Angewandte Chemie International Edition **48**(36): 6594-6596.

Hoel, C. A., T. O. Mason, J.-F. o. Gaillard and K. R. Poeppelmeier (2010). "Transparent Conducting Oxides in the ZnO-In2O3-SnO2System." Chemistry of Materials **22**(12): 3569-3579.

Hossain, M. A., J. R. Jennings, Z. Y. Koh and Q. Wang (2011). "Carrier generation and collection in CdS/CdSe-sensitized SnO2 solar cells exhibiting unprecedented photocurrent densities." Acs Nano **5**(4): 3172-3181.

Hu, C. (2010). Modern semiconductor devices for integrated circuits, Prentice Hall.

Huang, Y., Z. Ji and C. Chen (2007). "Preparation and characterization of p-type transparent conducting tin-gallium oxide films." Applied surface science **253**(11): 4819-4822.

Ismail, R., M. T. Ahmadi and S. Anwar (2012). Advanced nanoelectronics, CRC Press.

Jagadish, C. and S. J. Pearton (2011). Zinc oxide bulk, thin films and nanostructures: processing, properties, and applications, Elsevier.

Jang, M., T. Q. Trung, J.-H. Jung, B.-Y. Kim and N.-E. Lee (2014). "Improved performance and stability of field-effect transistors with polymeric residue-free graphene channel transferred by gold layer." Physical Chemistry Chemical Physics **16**(9): 4098-4105.

Jarzebski, Z. and J. Marton (1976). "Physical properties of SnO2 materials I. Preparation and defect structure." Journal of the electrochemical Society **123**(7): 199C-205C.

Jarzebski, Z. and J. Marton (1976). "Physical properties of SnO2 materials II. Electrical properties." Journal of the electrochemical Society **123**(9): 299C-310C.

Ji, Y. C., H. X. Zhang, X. H. Zhang and Z. Q. Li (2013). "Structures, optical properties, and electrical transport processes of SnO2 films with oxygen deficiencies." physica status solidi (b) **250**(10): 2145-2152.

Ji, Z., Z. He, Y. Song, K. Liu and Z. Ye (2003). "Fabrication and characterization of indium-doped p-type SnO 2 thin films." Journal of Crystal Growth **259**(3): 282-285.

Ji, Z., L. Zhao, Z. He, Q. Zhou and C. Chen (2006). "Transparent p-type conducting indium-doped SnO 2 thin films deposited by spray pyrolysis." Materials Letters **60**(11): 1387-1389.

Jorio, A., G. Dresselhaus and M. S. Dresselhaus (2007). Carbon nanotubes: advanced topics in the synthesis, structure, properties and applications, Springer Science & Business Media.

Kan, E., J. Yang and Z. Li (2011). Graphene nanoribbons: geometric, electronic, and magnetic Properties, INTECH Open Access Publisher.

Kawazoe, H., H. Yanagi, K. Ueda and H. Hosono (2000). "Transparent p-type conducting oxides: design and fabrication of pn heterojunctions." Mrs Bulletin **25**(08): 28-36.

Kılıç, Ç. and A. Zunger (2002). "Origins of coexistence of conductivity and transparency in SnO 2." Physical Review Letters **88**(9): 095501.

Kılıç, Ç. and A. Zunger (2002). "Origins of Coexistence of Conductivity and Transparency inSnO2." Physical Review Letters **88**(9).

Kobayashi, Y., K.-i. Fukui, T. Enoki, K. Kusakabe and Y. Kaburagi (2005). "Observation of zigzag and armchair edges of graphite using scanning tunneling microscopy and spectroscopy." Physical Review B **71**(19): 193406.

Kresse, G. and J. Furthmüller (1996). "Efficiency of ab-initio total energy calculations for metals and semiconductors using a plane-wave basis set." Computational Materials Science **6**(1): 15-50.

Kresse, G. and D. Joubert (1999). "From ultrasoft pseudopotentials to the projector augmented-wave method." Physical Review B **59**(3): 1758.

Landau, L. (1937). "Zur Theorie der phasenumwandlungen II." Phys. Z. Sowjetunion **11**: 26-35.

Leem, D.-S., J.-O. Song, H.-G. Hong, J. Kwak, Y. Park and T.-Y. Seong (2004). "Low resistance and highly reflective Sb-doped SnO2/Ag ohmic contacts to p-type GaN for flip-chip LEDs." Electrochemical and solid-state letters **7**(10): G219-G221.

Li, X., X. Wang, L. Zhang, S. Lee and H. Dai (2008). "Chemically derived, ultrasmooth graphene nanoribbon semiconductors." Science **319**(5867): 1229-1232.

Liang, G. (2008). Width Effects in ballistic graphene nanoribbon FETs. Nanoelectronics Conference, 2008. INEC 2008. 2nd IEEE International, IEEE.

Liang, X., B. A. Sperling, I. Calizo, G. Cheng, C. A. Hacker, Q. Zhang, Y. Obeng, K. Yan, H. Peng and Q. Li (2011). "Toward clean and crackless transfer of graphene." ACS nano **5**(11): 9144-9153.

Liu, H., Y. Liu and D. Zhu (2011). "Chemical doping of graphene." Journal of materials chemistry **21**(10): 3335-3345.

Liu, J., M. Notarianni, G. Will, V. T. Tiong, H. Wang and N. Motta (2013). "Electrochemically exfoliated graphene for electrode films: effect of graphene flake thickness on the sheet resistance and capacitive properties." Langmuir **29**(43): 13307-13314.

Liu, Y., C. Hsieh, Y. Wu, Y. Wei, P. Lee and C. Liu (2012). "Transparent p-type AlN: SnO2 and p-AlN: SnO2/n-SnO2: In2O3 pn junction fabrication." Applied Physics Letters **101**(12): 122107.

Liu, Y. S., C. I. Hsieh, Y. J. Wu, Y. S. Wei, P. M. Lee and C. Y. Liu (2012). "Transparent p-type AlN:SnO2 and p-AlN:SnO2/n-SnO2:In2O3 p-n junction fabrication." Applied Physics Letters **101**(12): 122107.

Lusk, M. T. and L. D. Carr (2008). "Nanoengineering defect structures on graphene." Physical review letters **100**(17): 175503.

Manifacier, J., M. De Murcia, J. Fillard and E. Vicario (1977). "Optical and electrical properties of SnO 2 thin films in relation to their stoichiometric deviation and their crystalline structure." Thin Solid Films **41**(2): 127-135.

Mao, Q., Z. Ji and L. Zhao (2010). "Mobility enhancement of p-type SnO2 by In–Ga co-doping." physica status solidi (b) **247**(2): 299-302.

Mideen, A. S., M. Ganesan, M. Anbukulandainathan, K. Sarangapani, V. Balaramachandran, V. Kapali and S. V. Iyer (1989). "Development of new alloys of commercial aluminium (2S) with zinc, indium, tin, and bismuth as anodes for alkaline batteries." Journal of Power Sources **27**(3): 235-244.

Minami, T. (2005). "Transparent conducting oxide semiconductors for transparent electrodes." Semiconductor Science and Technology **20**(4): S35-S44.

Minami, T. (2008). "Present status of transparent conducting oxide thin-film development for Indium-Tin-Oxide (ITO) substitutes." Thin Solid Films **516**(17): 5822-5828.

Minami, T. (2008). "Substitution of transparent conducting oxide thin films for indium tin oxide transparent electrode applications." Thin Solid Films **516**(7): 1314-1321.

Mishra, K., K. Johnson and P. Schmidt (1995). "Electronic structure of antimony-doped tin oxide." Physical Review B **51**(20): 13972.

Nagasawa, M. and S. Shionoya (1971). "Properties of oxidized SnO2 single crystals." Japanese Journal of Applied Physics **10**(6): 727.

Nakada, K., M. Fujita, G. Dresselhaus and M. S. Dresselhaus (1996). "Edge state in graphene ribbons: Nanometer size effect and edge shape dependence." Physical Review B **54**(24): 17954.

Neto, A. C., F. Guinea, N. Peres, K. S. Novoselov and A. K. Geim (2009). "The electronic properties of graphene." Reviews of modern physics **81**(1): 109.

Ni, J., X. Zhao, X. Zheng, J. Zhao and B. Liu (2009). "Electrical, structural, photoluminescence and optical properties of p-type conducting, antimony-doped SnO2 thin films." Acta Materialia **57**(1): 278-285.

Novoselov, K. S., A. K. Geim, S. Morozov, D. Jiang, Y. Zhang, S. a. Dubonos, I. Grigorieva and A. Firsov (2004). "Electric field effect in atomically thin carbon films." science **306**(5696): 666-669.

Obeng, Y. and P. Srinivasan (2011). "Graphene: Is it the future for semiconductors? An overview of the material, devices, and applications." Interface-Electrochemical Society **20**(1): 47.

Oviedo, J. and M. Gillan (2000). "Energetics and structure of stoichiometric SnO 2 surfaces studied by first-principles calculations." Surface Science **463**(2): 93-101.

Pan, S., C. Ye, X. Teng, H. Fan and G. Li (2006). "Preparation and characterization of nitrogen-incorporated SnO2 films." Applied Physics A **85**(1): 21-24.

Pati, S. K., T. Enoki and C. N. R. Rao (2011). Graphene and its fascinating attributes, World Scientific.

Perdew, J. P., K. Burke and M. Ernzerhof (1996). "Generalized gradient approximation made simple." Physical review letters **77**(18): 3865.

Profeta, G., M. Calandra and F. Mauri (2012). "Phonon-mediated superconductivity in graphene by lithium deposition." Nature physics **8**(2): 131-134.

Reich, S., J. Maultzsch, C. Thomsen and P. Ordejon (2002). "Tight-binding description of graphene." Physical Review B **66**(3): 035412.

Rodrigues, J. N. B., P. A. D. Gonçalves, N. F. G. Rodrigues, R. M. Ribeiro, J. M. B. Lopes dos Santos and N. M. R. Peres (2011). "Zigzag graphene nanoribbon edge reconstruction with Stone-Wales defects." Physical Review B **84**(15).

Rosenberger, L., R. Baird, E. McCullen, G. Auner and G. Shreve (2008). "XPS analysis of aluminum nitride films deposited by plasma source molecular beam epitaxy." Surface and Interface Analysis **40**(9): 1254-1261.

RotoMetals. (2015, July 2015). "Indium Metal." Retrieved 18 July, 2015, from http://www.rotometals.com/product-p/indiumingot.htm.

Sagar, A. S. (2011). "Graphene-based Field-effect Transistors."

Samadi, M. and R. Faez (2013). Effect of Stone-Wales defects on electronic properties of armchair graphene nanoribbons. Electrical Engineering (ICEE), 2013 21st Iranian Conference on, IEEE.

Samson, S. and C. Fonstad (1973). "Defect structure and electronic donor levels in stannic oxide crystals." Journal of Applied Physics **44**(10): 4618-4621.

Scanlon, D. O. and G. W. Watson (2012). "On the possibility of p-type SnO 2." Journal of Materials Chemistry **22**(48): 25236-25245.

Schwierz, F. (2010). "Graphene transistors." Nature nanotechnology **5**(7): 487-496.

Semenoff, G. W. (1984). "Condensed-matter simulation of a three-dimensional anomaly." Physical Review Letters **53**(26): 2449.

Simulator, Q. (2012). Atomistix ToolKit (ATK).

Singh, A. K., A. Janotti, M. Scheffler and C. G. Van de Walle (2008). "Sources of Electrical Conductivity inSnO2." Physical Review Letters **101**(5).

Son, Y.-W., M. L. Cohen and S. G. Louie (2006). "Energy gaps in graphene nanoribbons." Physical review letters **97**(21): 216803.

Stadler, A. (2012). "Transparent Conducting Oxides—An Up-To-Date Overview." Materials **5**(12): 661-683.

Stashans, A., P. Puchaicela and R. Rivera (2014). "DFT study of chromium-doped SnO2 materials." Journal of Materials Science **49**(7): 2904-2911.

Stefanov, P., G. Atanasova, E. Manolov, Z. Raicheva and V. Lazarova (2008). Preparation and characterization of SnO2 films for sensing applications. Journal of Physics: Conference Series, IOP Publishing.

Svane, A. and E. Antoncik (1987). "Electronic structure of rutile SnO 2, GeO 2 and TeO 2." Journal of Physics and Chemistry of Solids **48**(2): 171-180.

Terrones, M., A. R. Botello-Méndez, J. Campos-Delgado, F. López-Urías, Y. I. Vega-Cantú, F. J. Rodríguez-Macías, A. L. Elías, E. Muñoz-Sandoval, A. G. Cano-Márquez and J.-C. Charlier (2010). "Graphene and graphite nanoribbons: Morphology, properties, synthesis, defects and applications." Nano Today **5**(4): 351-372.

Toolkit, A. 11.2. 3, QuantumWise A/S.

Torres, L. E. F., S. Roche and J.-C. Charlier (2014). Introduction to graphene-based nanomaterials: from electronic structure to quantum transport, Cambridge University Press.

Uchoa, B. and A. C. Neto (2007). "Superconducting states of pure and doped graphene." Physical review letters **98**(14): 146801.

Uppstu, A. (2014). "Electronic properties of graphene from tight-binding simulations."

Varea, D. M. (2007). Crecimiento y caracterización mediante técnicas de microscopía, de nano-y microestructuras de SnO2 y TiO2, Universidad Complutense de Madrid.

Villamagua, L., A. Stashans, P.-M. Lee, Y.-S. Liu, C.-Y. Liu and M. Carini (2015). "Change in the electrical conductivity of SnO2 crystal from n-type to p-type conductivity." Chemical Physics **452**: 71-77.

Wager, J. F. (2003). "Transparent electronics." Science **300**(5623): 1245-1246.

Wallace, P. (1947). "The band structure of graphite." Phys. Rev **71**(9): 622-634.

Wang, X., Y. Ouyang, X. Li, H. Wang, J. Guo and H. Dai (2008). "Room-temperature all-semiconducting sub-10-nm graphene nanoribbon field-effect transistors." Physical review letters **100**(20): 206803.

Wang, X., L. Zhi and K. Müllen (2008). "Transparent, conductive graphene electrodes for dye-sensitized solar cells." Nano letters **8**(1): 323-327.

Wolf, E. L. (2014). Applications of Graphene: An Overview, Springer.

Wong, H.-S. P. and D. Akinwande (2011). Carbon nanotube and graphene device physics, Cambridge University Press.

woo Lee, S., Y.-W. Kim and H. Chena (2001). "Electrical properties of Ta-doped SnO2 thin films prepared by the metal–organic chemical-vapor deposition method." Applied Physics Letters **78**(3).

Wu, A., D. Yoo, J.-K. Lee and M. Rubner (1999). "Solid-state light-emitting devices based on the tris-chelated ruthenium (II) complex: 3. High efficiency devices via a layer-by-layer molecular-level blending approach." Journal of the American Chemical Society **121**(20): 4883-4891.

Wu, Y., Y. Liu, C. Hsieh, P. Lee, Y. Wei, C. Liao and C. Liu (2015). "Study of p-type AlN-doped SnO 2 thin films and its transparent devices." Applied Surface Science **328**: 262-268.

Wyckoff, R. W. G. and R. W. Wyckoff (1960). Crystal structures, Interscience New York.

Zhang, Y., Y.-W. Tan, H. L. Stormer and P. Kim (2005). "Experimental observation of the quantum Hall effect and Berry's phase in graphene." Nature **438**(7065): 201-204.

Appendices

Appendix A: POSCAR files

A.1. POSCAR n-doped SnO_2 (SnO_2+V_O+Sn_i)

POSCAR file which contains the lattice geometry and the ionic positions of n-type SnO_2. The lattice is relaxed together with the atomic coordinates.

```
Sn O : SnO2 + Vo + Sni
   1.0000000000000000
     9.4660987692140370   -0.0108492177421148   -0.0009239468513259
    -0.0100803292947478    9.4526101282417976   -0.0011316839478221
    -0.0013967636733983   -0.0014451787835266   12.6388499912347712
   Sn   O
    32    63
Direct
  0.7510620986688200  0.2522283722452569  0.6250136349287215
  0.9997692514887841  0.0024192319880572  0.9999381954876402
  0.2499058500846413  0.2525956622641167  0.1250031695457385
  0.4999331545955746  0.0025379911790795 -0.0000031682079472
  0.7500675123094680  0.2524711118009896  0.1250064599861216
 -0.0001607360290357  0.5025124116645068  0.0000121458826848
  0.2498667834898939  0.7526054978124130  0.1250053273975742
  0.5001868885184868  0.5027694852526434  0.0001077925273641
  0.7504979862571053  0.7531217565391570  0.1252559153471532
  0.9992046466261101  0.0018706923385200  0.2500860310766821
  0.2503747428922627  0.2530370520604204  0.3747551616563986
  0.4999420920345913  0.0028202336997688  0.2498953279670597
  0.7512485562865243  0.2525225026564208  0.3750476596273699
  0.0000358942976611  0.5025409565241893  0.2498594815400053
  0.2498877728297408  0.7538048376945825  0.3749788836043551
  0.5003707940351247  0.5029925281071522  0.2494250179529364
  0.7469373592242464  0.7495907268883997  0.3777370244165293
  0.0011503550983278  0.0036860877982039  0.4999579974002070
  0.2500616808233435  0.2526664195417327  0.6252434399455048
  0.4985402690215560  0.0046257385520907  0.5000022669632856
  0.0019770460510995  0.5012676801271662  0.5000227742688482
  0.2497335149706604  0.7533537855325144  0.6250073101847355
  0.5012267571094017  0.5038664622573429  0.5001456825226589
  0.7460403091501883  0.7488652776992653  0.6217702512518209
  0.9987630750601356  0.0012311014338380  0.7497112939132449
  0.2496413643530242  0.2522204988323214  0.8750774317635717
  0.4995343473012762  0.0024415986851489  0.7501251442488192
  0.7498451020462599  0.2521449709482848  0.8750461611597299
 -0.0001916601196573  0.5022682460179999  0.7501203616123343
  0.2495059244975705  0.7523577214804648  0.8751155808171101
  0.4999149044457100  0.5025536512669548  0.7507480027593221
  0.7502796020532050  0.7529283399090650  0.8744873812768374
  0.1531894125837852  0.1546441065358634  0.0000430720375070
  0.3462896179697243  0.3501271967276181  0.0000015747753288
  0.4036728120017847  0.1005285340034509  0.1249858261051326
  0.0966623738568573  0.4050477557606941  0.1250010277138422
  0.6534220668679283  0.1549237980202396 -0.0000524096231685
  0.8467949220573031  0.3496505054285824 -0.0000113913310516
  0.9028343311528461  0.0994349672592992  0.1250862036272620
  0.5967431518713806  0.4049071820956274  0.1248447249856597
  0.1532674670162841  0.6549090147481701  0.0001074343567588
```

```
 0.3461475032452173  0.8503992210679034 -0.0000745059890172
 0.4032880413728306  0.6002239557387148  0.1248479654289915
 0.0958535941591098  0.9044860724456498  0.1251185051999397
 0.6535493799614206  0.6554830274304259  0.9999579962564290
 0.8465430812505678  0.8500870847686914  0.9998362242438497
 0.9036927759860831  0.6002321197888256  0.1250193705440191
 0.5969414235203443  0.9056958417418041  0.1251032904940169
 0.1536118778455380  0.1550520805609968  0.2498912069656748
 0.3471326509359505  0.3510571468885506  0.2502263527678414
 0.4033830307454537  0.1012660677951758  0.3747402493951825
 0.0975090650316150  0.4049084778339593  0.3748044188185304
 0.6532690977207701  0.1555838901529088  0.2506147102775886
 0.8468150587051805  0.3500610132154359  0.2497731533035989
 0.9044570995373830  0.1011218252643063  0.3748731981817041
 0.5998777711003340  0.4084327880799377  0.3753742794940345
 0.1539395628200191  0.6547646117842011  0.2504935303880893
 0.3464656392332836  0.8505288168887565  0.2497933937260984
 0.4068771020524803  0.6037007184282825  0.3753546282651615
 0.0972023341865818  0.9057057913260272  0.3748958704905356
 0.6528886751643463  0.6546014482574700  0.2490793845534049
 0.8453874265335435  0.8488260692005151  0.2519168474720205
 0.9027894024484742  0.5976968841778073  0.3761167508068390
 0.5938719638254074  0.9042611215173838  0.3761159185889048
 0.1543283148927238  0.1557223282073784  0.4999593704356763
 0.3477285417038583  0.3512257619679605  0.5001073980831148
 0.4030831387728968  0.1010110700860254  0.6253048923695910
 0.0972423410522405  0.4044269921850303  0.6252984153751481
 0.6530515413392509  0.1561061720272512  0.4998905329349372
 0.8473678729507395  0.3497772869081463  0.5001317099069114
 0.9040429142833684  0.1008533396878627  0.6250506478591201
 0.5995719072372468  0.4078002854585464  0.6249087715064873
 0.1547118894176797  0.6544662790387078  0.5000170780668064
 0.3458106769465825  0.8511431759383179  0.5001122222488901
 0.4060227945451365  0.6030267435106268  0.6249036538107666
 0.0967891321192661  0.9054727840729184  0.6250406952160975
 0.8475403939559032  0.8517018823105369  0.4999438111306930
 0.9026666267502339  0.5974682117443953  0.6238614308171812
 0.5935358864364216  0.9041604853981919  0.6239251632192151
 0.1532533953938453  0.1544746538898968  0.7501196418388002
 0.3469263382428410  0.3503324094405653  0.7498578755577822
 0.4033503638081951  0.1002155844327014  0.8749873880960871
 0.0965842846786006  0.4049065743421595  0.8749970696028555
 0.6530246659647784  0.1552157489257242  0.7495591077173668
 0.8464585244045356  0.3500121162858502  0.7502902441716853
 0.9027840560347768  0.0992174089767628  0.8747002563939934
 0.5963304294470269  0.4045873792243576  0.8753130849777214
 0.1536711669221257  0.6544786021093030  0.7494949036984090
 0.3462525892195835  0.8499459170426543  0.7502746517930510
 0.4027657610987844  0.5998441790607674  0.8753523125268462
 0.0954311890317712  0.9040024737488443  0.8747049688087959
 0.6523945291912510  0.6541383457511176  0.7509802149781222
 0.8446468862138808  0.8485923063165220  0.7475762079446890
 0.9036677579922970  0.6002008593387437  0.8749018756311848
 0.5964810300918206  0.9052447692124094  0.8748506234280740
```

A.2. POSCAR pure SnO_2

POSCAR file which contains the lattice geometry and the ionic positions of pure SnO_2. The lattice is relaxed together with the atomic coordinates.

```
Sn O : Pure SnO2
   1.0000000000000000
     9.4568053375635301    0.0000000000000000    0.0000000000000000
     0.0000000000000000    9.4568053375635301    0.0000000000000000
     0.0000000000000000    0.0000000000000000   12.6424021315486659
   Sn   O
    32    64
Direct
  0.0000000000000000 -0.0000000000000000 -0.0000000000000000
  0.2500000010570815  0.2500000010570815  0.1250000034019010
  0.5000000000000000 -0.0000000000000000 -0.0000000000000000
  0.7500000010570815  0.2500000010570815  0.1250000034019010
  0.0000000000000000  0.5000000000000000  0.0000000000000000
  0.2500000010570815  0.7500000010570815  0.1250000034019010
  0.5000000000000000  0.5000000000000000  0.0000000000000000
  0.7500000010570815  0.7500000010570815  0.1250000034019010
  0.0000000000000000 -0.0000000000000000  0.2500000000000000
  0.2500000010570815  0.2500000010570815  0.3750000034019010
  0.5000000000000000 -0.0000000000000000  0.2500000000000000
  0.7500000010570815  0.2500000010570815  0.3750000034019010
  0.0000000000000000  0.5000000000000000  0.2500000000000000
  0.2500000010570815  0.7500000010570815  0.3750000034019010
  0.5000000000000000  0.5000000000000000  0.2500000000000000
  0.7500000010570815  0.7500000010570815  0.3750000034019010
  0.0000000000000000 -0.0000000000000000  0.5000000000000000
  0.2500000010570815  0.2500000010570815  0.6250000034019010
  0.5000000000000000 -0.0000000000000000  0.5000000000000000
  0.7500000010570815  0.2500000010570815  0.6250000034019010
  0.0000000000000000  0.5000000000000000  0.5000000000000000
  0.2500000010570815  0.7500000010570815  0.6250000034019010
  0.5000000000000000  0.5000000000000000  0.5000000000000000
  0.7500000010570815  0.7500000010570815  0.6250000034019010
  0.0000000000000000 -0.0000000000000000  0.7500000000000000
  0.2500000010570815  0.2500000010570815  0.8750000034019010
  0.5000000000000000 -0.0000000000000000  0.7500000000000000
  0.7500000010570815  0.2500000010570815  0.8750000034019010
  0.0000000000000000  0.5000000000000000  0.7500000000000000
  0.2500000010570815  0.7500000010570815  0.8750000034019010
  0.5000000000000000  0.5000000000000000  0.7500000000000000
  0.7500000010570815  0.7500000010570815  0.8750000034019010
  0.1529585088908939  0.1529585088908939  0.0000000000000000
  0.3470414931175618  0.3470414931175618 -0.0000000000000000
  0.4029585098422679  0.0970414921661877  0.1250000034019010
  0.0970414921661877  0.4029585098422679  0.1250000034019010
  0.6529585088908938  0.1529585088908939 -0.0000000000000000
  0.8470414931175618  0.3470414931175618  0.0000000000000000
  0.9029585098422679  0.0970414921661877  0.1250000034019010
  0.5970414921661877  0.4029585098422679  0.1250000034019010
  0.1529585088908939  0.6529585088908938 -0.0000000000000000
  0.3470414931175618  0.8470414931175618 -0.0000000000000000
  0.4029585098422679  0.5970414921661877  0.1250000034019010
  0.0970414921661877  0.9029585098422679  0.1250000034019010
```

```
0.6529585088908938  0.6529585088908938 -0.0000000000000000
0.8470414931175618  0.8470414931175618 -0.0000000000000000
0.9029585098422679  0.5970414921661877  0.1250000034019010
0.5970414921661877  0.9029585098422679  0.1250000034019010
0.1529585088908939  0.1529585088908939  0.2500000000000000
0.3470414931175618  0.3470414931175618  0.2500000000000000
0.4029585098422679  0.0970414921661877  0.3750000034019010
0.0970414921661877  0.4029585098422679  0.3750000034019010
0.6529585088908938  0.1529585088908939  0.2500000000000000
0.8470414931175618  0.3470414931175618  0.2500000000000000
0.9029585098422679  0.0970414921661877  0.3750000034019010
0.5970414921661877  0.4029585098422679  0.3750000034019010
0.1529585088908939  0.6529585088908938  0.2500000000000000
0.3470414931175618  0.8470414931175618  0.2500000000000000
0.4029585098422679  0.5970414921661877  0.3750000034019010
0.0970414921661877  0.9029585098422679  0.3750000034019010
0.6529585088908938  0.6529585088908938  0.2500000000000000
0.8470414931175618  0.8470414931175618  0.2500000000000000
0.9029585098422679  0.5970414921661877  0.3750000034019010
0.5970414921661877  0.9029585098422679  0.3750000034019010
0.1529585088908939  0.1529585088908939  0.5000000000000000
0.3470414931175618  0.3470414931175618  0.5000000000000000
0.4029585098422679  0.0970414921661877  0.6250000034019010
0.0970414921661877  0.4029585098422679  0.6250000034019010
0.6529585088908938  0.1529585088908939  0.5000000000000000
0.8470414931175618  0.3470414931175618  0.5000000000000000
0.9029585098422679  0.0970414921661877  0.6250000034019010
0.5970414921661877  0.4029585098422679  0.6250000034019010
0.1529585088908939  0.6529585088908938  0.5000000000000000
0.3470414931175618  0.8470414931175618  0.5000000000000000
0.4029585098422679  0.5970414921661877  0.6250000034019010
0.0970414921661877  0.9029585098422679  0.6250000034019010
0.6529585088908938  0.6529585088908938  0.5000000000000000
0.8470414931175618  0.8470414931175618  0.5000000000000000
0.9029585098422679  0.5970414921661877  0.6250000034019010
0.5970414921661877  0.9029585098422679  0.6250000034019010
0.1529585088908939  0.1529585088908939  0.7500000000000000
0.3470414931175618  0.3470414931175618  0.7500000000000000
0.4029585098422679  0.0970414921661877  0.8750000034019010
0.0970414921661877  0.4029585098422679  0.8750000034019010
0.6529585088908938  0.1529585088908939  0.7500000000000000
0.8470414931175618  0.3470414931175618  0.7500000000000000
0.9029585098422679  0.0970414921661877  0.8750000034019010
0.5970414921661877  0.4029585098422679  0.8750000034019010
0.1529585088908939  0.6529585088908938  0.7500000000000000
0.3470414931175618  0.8470414931175618  0.7500000000000000
0.4029585098422679  0.5970414921661877  0.8750000034019010
0.0970414921661877  0.9029585098422679  0.8750000034019010
0.6529585088908938  0.6529585088908938  0.7500000000000000
0.8470414931175618  0.8470414931175618  0.7500000000000000
0.9029585098422679  0.5970414921661877  0.8750000034019010
0.5970414921661877  0.9029585098422679  0.8750000034019010
```

A.3. POSCAR n-doped SnO_2 (SnO_2+V_O+H @ position V_O)

POSCAR file which contains the lattice geometry and the ionic positions of n-type SnO_2. The lattice is relaxed together with the atomic coordinates.

```
Sn O: SnO2+Vo
   1.0000000000000000
     9.4727264233294726    0.0077522866895504    0.0043613948238325
     0.0077522866895504    9.4727264233294726    0.0043613948238325
     0.0059275956936619    0.0059275956936619   12.6757758984596656
   H    Sn    O
     1    32    63
Direct
  0.6520326758320495  0.6520326758320495  0.4894894533199194
  0.0008410291360450  0.0008410291360450 -0.0003629891795310
  0.2501521807381143  0.2501521807381143  0.1237590081460330
  0.4996480346950874  0.0003604485079277 -0.0007717513187934
  0.7497156159916240  0.2497150128407746  0.1240663029534518
  0.0003604485079277  0.4996480346950874 -0.0007717513187934
  0.2497150128407746  0.7497156159916240  0.1240663029534518
  0.4999099087538498  0.4999099087538498 -0.0012472438924797
  0.7498943920100315  0.7498943920100315  0.1241055532365120
 -0.0005235118645412 -0.0005235118645412  0.2489224884458035
  0.2475382641891578  0.2475382641891578  0.3727943018800366
  0.4995533343716417 -0.0005851644593237  0.2487884012434572
  0.7503884910581339  0.2489473701272749  0.3739304041584625
 -0.0005851644593237  0.4995533343716417  0.2487884012434572
  0.2489473701272749  0.7503884910581339  0.3739304041584625
  0.4999206727021427  0.4999206727021427  0.2484275708319176
  0.7508718433701854  0.7508718433701854  0.3718750916758234
 -0.0000818458013942 -0.0000818458013942  0.4991984502505249
  0.2488587922376958  0.2488587922376958  0.6244865078257958
  0.4988322313439457  0.0004861740927153  0.4987849684581933
  0.7504218901313211  0.2496196212130989  0.6234401935500553
  0.0004861740927153  0.4988322313439457  0.4987849684581933
  0.2496196212130989  0.7504218901313211  0.6234401935500553
  0.4924509418466695  0.4924509418466695  0.4979716073739668
  0.7575035529410024  0.7575035529410024  0.6299510140137958
  0.0023899118877711  0.0023899118877711  0.7503365696938284
  0.2514950170121627  0.2514950170121627  0.8740660171691711
  0.4998213330047938 -0.0003290861962595  0.7492978177241987
  0.7500177776354134  0.2503736705651335  0.8738868144799856
 -0.0003290861962595  0.4998213330047938  0.7492978177241987
  0.2503736705651335  0.7500177776354134  0.8738868144799856
  0.5018272074844957  0.5018272074844957  0.7483690307417117
  0.7503501327887474  0.7503501327887474  0.8765023053532439
  0.1536811447601423  0.1536811447601423 -0.0010761904412499
  0.3475998310559388  0.3475998310559388 -0.0010047984135070
  0.4026192632652147  0.0969442026719174  0.1244519451832288
  0.0969442026719174  0.4026192632652147  0.1244519451832288
  0.6529761855603960  0.1529524402609850 -0.0010865267150298
  0.8467663309933443  0.3475957771796793 -0.0008645370825210
  0.9028841801865171  0.0972190518538950  0.1245390574912065
  0.5967485482021448  0.4027458911133247  0.1243222871088223
  0.1529524402609850  0.6529761855603960 -0.0010865267150298
  0.3475957771796793  0.8467663309933443 -0.0008645370825210
  0.4027458911133247  0.5967485482021448  0.1243222871088223
```

```
 0.0972190518538950  0.9028841801865171  0.1245390574912065
 0.6526028213202969  0.6526028213202969 -0.0001062359015990
 0.8476765278078355  0.8476765278078355 -0.0000063636727830
 0.9026279148721675  0.5969240146497691  0.1244736870688874
 0.5969240146497691  0.9026279148721675  0.1244736870688874
 0.1521785849776712  0.1521785849776712  0.2484655054546119
 0.3469783736383928  0.3469783736383928  0.2497803921064656
 0.4027896213261465  0.0965768904936723  0.3737843844837617
 0.0965768904936723  0.4027896213261464  0.3737843844837617
 0.6524287579565146  0.1524539881110938  0.2500238077246496
 0.8465323346683516  0.3466562342043060  0.2495985474537421
 0.9018530469490471  0.0949174255334889  0.3747063175604179
 0.5984384902855923  0.4051778047501782  0.3752238896494003
 0.1524539881110938  0.6524287579565146  0.2500238077246496
 0.3466562342043060  0.8465323346683516  0.2495985474537421
 0.4051778047501782  0.5984384902855923  0.3752238896494003
 0.0949174255334889  0.9018530469490471  0.3747063175604179
 0.6525839847957136  0.6525839847957136  0.2498987855554086
 0.8468183491465658  0.8468183491465658  0.2488690905255899
 0.8996073964065417  0.5957251045152657  0.3753074239094202
 0.5957251045152657  0.8996073964065417  0.3753074239094202
 0.1521412373128235  0.1521412373128235  0.4990642287745387
 0.3438218351816824  0.3438218351816824  0.4983615711249392
 0.4032726750585984  0.0961654826618360  0.6239469618700522
 0.0961654826618360  0.4032726750585984  0.6239469618700522
 0.6520493581048431  0.1528180631157917  0.4988902740596481
 0.8475358636765735  0.3460897638126498  0.4986623544997877
 0.9020028411246002  0.0949582014207312  0.6242293209588665
 0.6003703877357071  0.4080304582667389  0.6210093012347658
 0.1528180631157917  0.6520493581048431  0.4988902740596481
 0.3460897638126498  0.8475358636765735  0.4986623544997877
 0.4080304582667389  0.6003703877357071  0.6210093012347658
 0.0949582014207312  0.9020028411246002  0.6242293209588665
 0.8433555087879026  0.8433555087879026  0.4994636368278624
 0.8987595109725816  0.5970201301399513  0.6225012802705269
 0.5970201301399513  0.8987595109725816  0.6225012802705269
 0.1538355527534593  0.1538355527534593  0.7494175706649935
 0.3485502526703427  0.3485502526703427  0.7473303841626201
 0.4035077405074037  0.0978664553704184  0.8736080634899583
 0.0978664553704184  0.4035077405074037  0.8736080634899583
 0.6526587018065767  0.1530168790163985  0.7476263186272758
 0.8469226450393867  0.3470473682604139  0.7479292994460879
 0.9038942798542552  0.0984740902301575  0.8743633206890803
 0.5979760496737734  0.4041524519233025  0.8730541252798659
 0.1530168790163985  0.6526587018065767  0.7476263186272758
 0.3470473682604139  0.8469226450393867  0.7479292994460879
 0.4041524519233025  0.5979760496737734  0.8730541252798659
 0.0984740902301575  0.9038942798542552  0.8743633206890803
 0.6553735480838337  0.6553735480838337  0.7483847107211224
 0.8501158225835905  0.8501158225835905  0.7531092272394178
 0.9030707489509509  0.5974892344959524  0.8739779003274579
 0.5974892344959524  0.9030707489509509  0.8739779003274579
```

A.4. POSCAR p-doped SnO_2 (SnO_2+Vo+1N+4Al)

POSCAR file which contains the lattice geometry and the ionic positions of p-type SnO_2. The lattice is relaxed together with the atomic coordinates.

```
Sn O N Al: SnO2 + Vo + 1N + 4Al
   1.0000000000000000
     9.4025862543126326    0.0468576523900366   -0.0018286949848796
     0.0475646756943082    9.4010775725292710    0.0004572370607642
    -0.0025968589680437    0.0007030644137259   12.5303134207860882
   Sn    O     N    Al
    28    62     1     4
Direct
  0.7455709340100367  0.2558422338161824  0.6229047135844721
  0.0008030418495931  0.0032828501848868  0.0002301368982642
  0.2502397821776901  0.2575987789966662  0.1271871215099168
  0.4992813833741941  0.0037187477678970  0.0009575416734090
  0.7521489336411427  0.2567522003439044  0.1271187783960428
  0.0012250388678274  0.5018168733976111  0.0044231847965976
  0.2484409006398836  0.7489667481242771  0.1271051573386546
  0.7532275891834223  0.7495404107545934  0.1277880082446656
  0.0002860665101827  0.0029870447730036  0.2503054957700651
  0.2435031401355032  0.2526050487402910  0.3746739220554700
  0.7485573056522736  0.2587472258020581  0.3750336384574028
  0.2505227577864467  0.7459625499795403  0.3750186834830381
  0.5052116661628852  0.5078508922887452  0.2583010835363941
  0.5015027384829799  0.5040113191191037  0.0003892496030347
  0.9906540553608648  0.9935674020602510  0.4996500141872638
  0.2444374288230580  0.2484850267020374  0.6227844414014947
  0.5072141679486585  0.9945357404075816  0.4992648611374761
  0.9913048238735518  0.5102518991561238  0.4952317626766772
  0.2536363598468483  0.7486492092981742  0.6228836739784015
  0.5031680566558862 -0.0011395421255323  0.2522983616197951
  0.9996525093774424  0.0022030607639657  0.7496041544877611
  0.2505367048004004  0.2543130598904803  0.8749982321445412
  0.5038951230357234  0.9973339692153039  0.7475548187736781
  0.7488989952815538  0.2537023996133566  0.8749075114776732
  0.9947115092590190  0.5063749197024623  0.7473742160439343
  0.2515357656024744  0.7518400070780601  0.8748784863993360
  0.5092317752382476  0.5118079279259760  0.7417134651638998
  0.7512136242033424  0.7524759373683388  0.8741772332101341
  0.1535784873968856  0.1577667278311350  0.0009749597873502
  0.3482546633847099  0.3525832866359371  0.0017871251193137
  0.4026078567347369  0.0998073810796902  0.1272901999746141
  0.0944995569533473  0.4078626051491233  0.1330659586782250
  0.6514783952943833  0.1586796519070929  0.0015094203789525
  0.8474243662865539  0.3511642203625935  0.0004654352798756
  0.9038770066684706  0.1020404471923460  0.1254168094915594
  0.5993486431390641  0.4098979851870714  0.1290868341001823
  0.1550857374898496  0.6528962731385627  0.0003763365367603
  0.3474079272004292  0.8489579146732922  0.0015632897023622
  0.4061286460899874  0.6007290243747535  0.1289641145229839
  0.0981204616397386  0.9050831702534139  0.1255375391912332
  0.6551069337478843  0.6550790416650148  0.0012141034311921
  0.8490017263530085  0.8490606019849880  0.0011253946407477
  0.9061069685736511  0.5975955220798742  0.1322791894652960
  0.5990141836172932  0.9044806404414247  0.1255120748999064
```

```
0.1536343976739483  0.1529645928741382  0.2501760407986922
0.3505334630598146  0.3504518636200845  0.2535143337586223
0.4044041664528526  0.0965541846306605  0.3761327569559548
0.0895958827556209  0.4107867372535289  0.3690427254175440
0.6528271622490208  0.1574583470023940  0.2512672272727391
0.8502437697000677  0.3570831545156778  0.2519119835675624
0.8992168353943254  0.0980383821395876  0.3753008494833385
0.5951977354318536  0.4120111170319302  0.3870969758637971
0.1480421143702627  0.6492118583106231  0.2514295167740008
0.3477270994093066  0.8463387540236581  0.2517303500213611
0.4072626686332909  0.5964498295045501  0.3866813448146413
0.0939246139875468  0.9006788611979051  0.3754149429046644
0.6573640738391047  0.6624935561624828  0.2590466599636994
0.8482222756335260  0.8541979906634694  0.2505083059990364
0.8934172338721988  0.6062626875458212  0.3689046411221315
0.6059840915609234  0.8930519912154864  0.3755960302912312
0.1458630922997301  0.1509638685035444  0.4987228164492611
0.3397249013285908  0.3451408184187662  0.4981462238413684
0.4052207330373933  0.0952392139271693  0.6232982695614404
0.0917147807099854  0.4086461885021590  0.6221598565860168
0.6545271130644665  0.1523102224742619  0.4984401656106634
0.8492193844793581  0.3498647688883590  0.4995164127168480
0.8973439548534449  0.0963469818883739  0.6237215979100790
0.5960444548284667  0.4122131769522909  0.6114879917213614
0.1484219683779597  0.6558364426431914  0.4995623006121097
0.3460122702061095  0.8506271903369229  0.4983826626154578
0.4103066956479132  0.5994210931157412  0.6114432171333299
0.0944855360541402  0.9008008316915451  0.6235844833118807
0.8303255083584679  0.8304775466829835  0.4987777093433646
0.8908126290975041  0.6077811164883330  0.6221012133176629
0.6061587856263250  0.8934821780863792  0.6232964517330916
0.1499142893624464  0.1533494973626396  0.7494981866061283
0.4031434921399215  0.0982086061263326  0.8732923556649929
0.0949919421537882  0.4062982380254502  0.8741734952429415
0.6501315033453247  0.1570891675068093  0.7486315041229762
0.8440427030839366  0.3512313047284004  0.7481777715507458
0.9020639916245825  0.1005687068980329  0.8753283282975735
0.6001200427555501  0.4099074525745844  0.8729650626699074
0.1548514220581076  0.6530446953889025  0.7485317771365882
0.3490559725061206  0.8469952238696097  0.7481842473421398
0.4082545294183696  0.6035644954943951  0.8729903406068656
0.0988728449499281  0.9054225206733670  0.8752973260736786
0.6608362099709830  0.6625179048158797  0.7425282228370473
0.8501408715934673  0.8515772565132749  0.7498538345245017
0.9039594635931996  0.6005881094172089  0.8765753080517913
0.5988381080238404  0.9056900292957768  0.8758694787475737
0.3504674126297520  0.3539179782754270  0.7463786670673979
0.7676458613006694  0.7656902691269601  0.3635115019638335
0.4748442162798309  0.4776500183159538  0.4999444073818816
0.9969929127233477  0.5049912492927412  0.2513843057839850
0.7664389725137315  0.7677831872761915  0.6355612508956135
```

A.5. Spatial coordinates of the C of a defected GNR

POSCAR file which contains the lattice geometry and the ionic positions of AGNRs. The lattice is relaxed together with the atomic coordinates.

```
C H: Unit cell of an 8-AGNR
1.0
 10.000000000000   0.000000000000   0.000000000000
  0.000000000000  18.613505986500   0.000000000000
  0.000000000000   0.000000000000   4.262580000000
C H
 16   4
Selective dynamics
Direct
  0.500000000000   0.268622150153   0.666666666667  T T T
  0.500000000000   0.731377849847   0.166666666667  T T T
  0.500000000000   0.665269892748   0.333333333333  T T T
  0.500000000000   0.599161935649   0.166666666667  T T T
  0.500000000000   0.731377849847   0.833333333333  T T T
  0.500000000000   0.665269892748   0.666666666667  T T T
  0.500000000000   0.533053978550   0.333333333333  T T T
  0.500000000000   0.599161935649   0.833333333333  T T T
  0.500000000000   0.466946021450   0.166666666667  T T T
  0.500000000000   0.400838064351   0.333333333333  T T T
  0.500000000000   0.334730107252   0.166666666667  T T T
  0.500000000000   0.466946021450   0.833333333333  T T T
  0.500000000000   0.400838064351   0.666666666667  T T T
  0.500000000000   0.268622150153   0.333333333333  T T T
  0.500000000000   0.334730107252   0.833333333333  T T T
  0.500000000000   0.533053978550   0.666666666667  T T T
  0.500000000000   0.782091972328   0.705476504628  T T T
  0.500000000000   0.217908027672   0.794523495372  T T T
  0.500000000000   0.217908027672   0.205476504628  T T T
  0.500000000000   0.782091972328   0.294523495372  T T T
```

Appendix B: Fabrication of GFET devices

GFET devices were fabricated through a three-step lithographic procedure: (i) resist deposition, (ii) transference of the pattern, and (iii) contacts evaporation, shown in figure (and described) below.

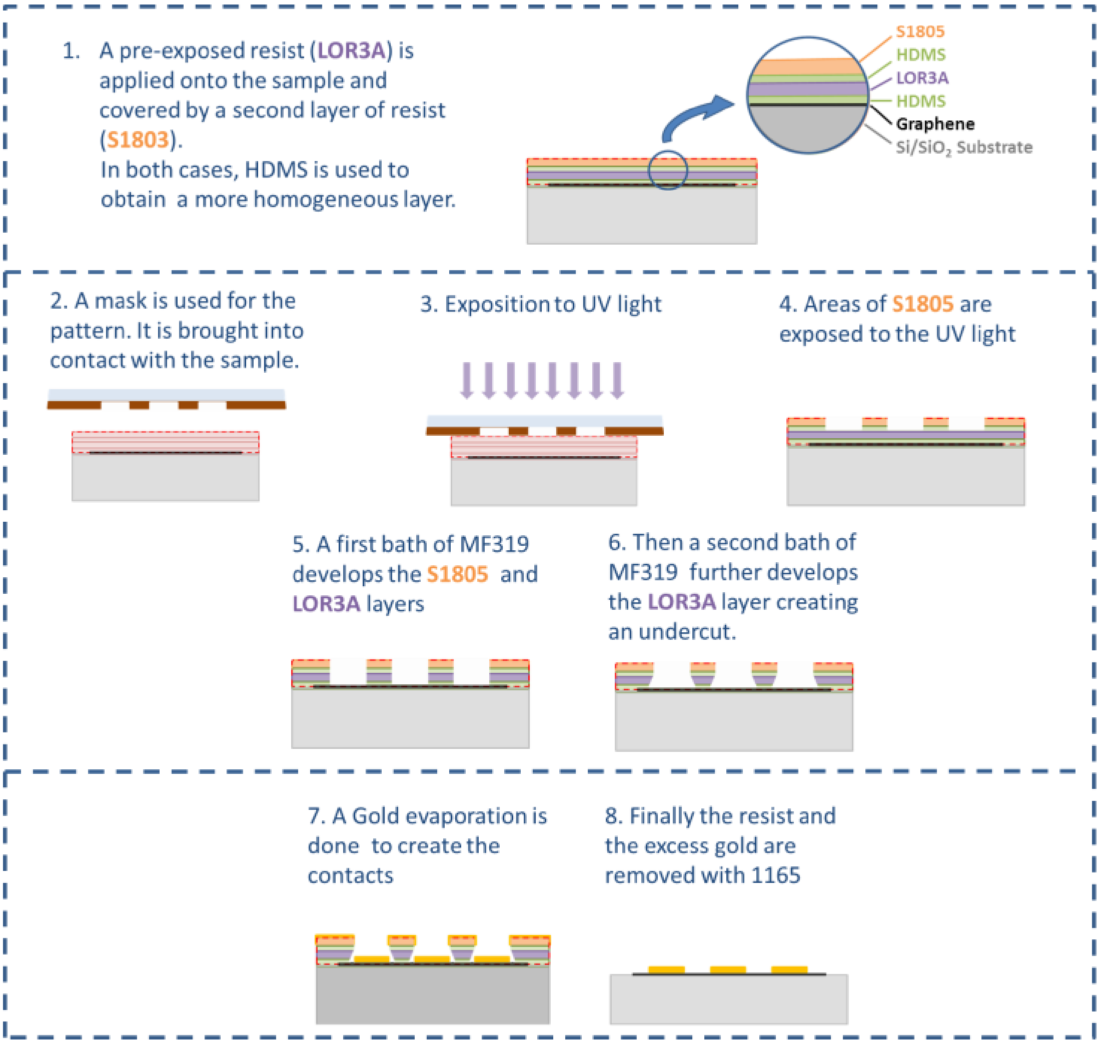

1. A pre-exposed resist (**LOR3A**) is applied onto the sample and covered by a second layer of resist (**S1803**). In both cases, HDMS is used to obtain a more homogeneous layer.

2. A mask is used for the pattern. It is brought into contact with the sample.

3. Exposition to UV light

4. Areas of **S1805** are exposed to the UV light

5. A first bath of MF319 develops the **S1805** and **LOR3A** layers

6. Then a second bath of MF319 further develops the **LOR3A** layer creating an undercut.

7. A Gold evaporation is done to create the contacts

8. Finally the resist and the excess gold are removed with 1165

B1. Photoresist deposition

Two different types of photoresist (or only resist) layers were used: *Lor3A* (300 nm) and *S1805* (500 nm). Only the first resist layer was pre-exposed to ultraviolet (UV) light. A layer of *HDMS* was applied before each resist to ensure proper adhesion.

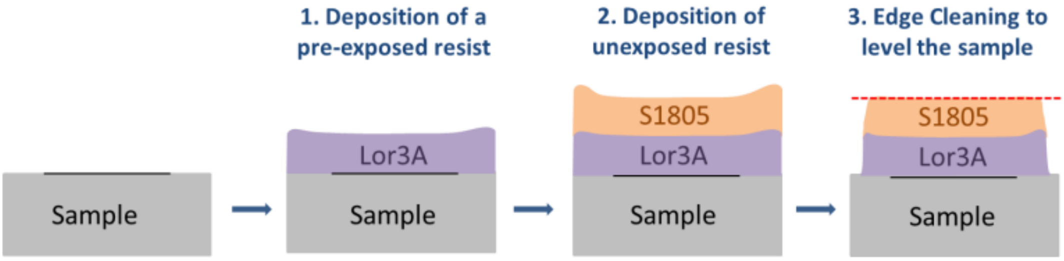

The samples were heated at 120ºC for 2 minutes in order to dehydrate the surface, which in turn ensures a homogeneous spread of the solution onto the substrate. Samples were placed inside the *spin coater* and then the *HMDS* was applied, following this scheme:

- 10s at 500 rpm (Acceleration of 1200)
- 60s at 4000 rpm (Acceleration of 1200)

The *Lor3A* layer also was prepared under the same scheme. Then the substrate was baked at 170ºC for 5 minutes. Following, *HDMS* and *S1805* were then spun on and baked at 115ºC for 2 minutes. Finally, the edges of the sample were cleaned using acetone.

B2. Transference of the pattern

In this step, the exposed spots to UV light were etched away, drawing the paths for the metallic contacts. This was done by bringing into contact the sample with the mask and exposing it to UV light for 4 s. The expected resolution was ~2 µm.

The exposed sections were immersed into *MF319* for 30 seconds. This developer, as abovementioned, only reacts with the resist pre-exposed to UV light, i.e., the *S1805* resist layer. In order to stop the reactions, the samples were cleaned with deionized (DI) water, and then baked at 120ºC for 5 minutes. *MF319* was used a second time for a deeper etch until *Lor3A* was reached. Cavities called *undercut* formed under the *S1805* layer. Once again the sample was dipped into DI water to stop the reaction.

B3. Contact evaporation

The contacts were created (under vacuum) by *metal evaporation*. The undercut were essential to ensure a split between the metals of the contacts (in the pattern) and the excess metals (on top of the resist). No undercut lead to a continuous layer of metals, meaning that it will not be removed during a lift off or could be ripped off entirely. 200 nm of gold was evaporated on top of 10 nm of titanium. The total thickness of the metals (as a matter of good practice) was left to be inferior to the thickness of the pre-exposed resist (300 nm with Lor3A). For the lift off, the samples were immersed (during at least 10 minutes) in a 40ºC bath of *1165*. Samples were then introduced in fresh *1165* at room temperature to finally rinse them in *Isopropanol* and DI wate*r*.

Appendix C: Publications in journals

C1.Published

Villamagua, L., Stashans, A., Lee, P. M., Liu, Y. S., Liu, C. Lui, Y., & Carini, M. (2015). Change in the electrical conductivity of SnO2 crystal from n-type to p-type conductivity. *Chemical Physics*, *452*, 71-77.

C2.Submitted

Villamagua, L., Stashans, A., Carini, M., & Maldonado, F. (2015). Hydrogen also can spark n-type conductivity in SnO_2: a microscopic analysis. **Submitted** to Mod. Phys. Lett. B. 01/09/2015.

Lee, P. M., Y. S., Liu, C. Liu, Y., **Villamagua, L**., Stashans, A., & Carini, M. Experimental observation and computer simulation of Al^{3+} -Sn^{4+} substitution in p-type AlN-doped SnO_2 thin film. **Submitted** to J. Phys. Chem. 04/11/2015.

C3.In preparation

Villamagua, L., Carini M. & Stashans, A. (2015). Band gap engineering of graphene through quantum confinement and edge distortion.

Appendix D: Conference talks

"Band gap engineering of graphene through quantum confinement and edge distortion (a tight-binding approach)", presented at IEEE NMDC2014.

"Band gap engineering of graphene through quantum confinement and edge distortion (a DFT approach)", presented at WASCON2015.

Appendix E: Conferences attended

IEEE Nanotechnology Materials and Devices Conference (IEEE NMDC2014), held in Aci Castello (Sicily, Italy), from 12th until 15th October 2014.

XVIII International Conference on WAVES AND STABILITY IN CONTINUOUS MEDIA (WASCON2015), held in Cetraro (Calabria, Italy), from 1st until 5th June 2015.

Appendix F: Summer schools attended

2DA ESCUELA DE QUÍMICA COMPUTACIONAL EN LAS AMÉRICAS, co-organized by the Programme Regional Fance - Amérique latine - Caraibe (PREFALC) and by the University of San Francisco de Quito (USFQ), held in the USFQ campus in Cumbayá (Pichincha, Ecuador) from 14th until 25th July 2014.

6th SINANO Summer School, co-organized by the ARCES Research Center of the University of Bologna and by the Italian Inter-University Consortium for Nanoelectronics (IUNET), held in Bertinoro (Forlì-Cesena, Italy) from 25th until 30th August 2014.

Appendix G: Internships and placements

G1. Internships

Universidad Técnica Particular de Loja (Loja, Ecuador)

Period: 6 months (01/03/2014 – 30/08/2014).
Motivation: Understanding the transition from n to p in the conductivity of SnO_2.
Work conducted: based on the results obtained from the DFT+U simulations, it was proposed an explanation for the switch of the conductivity from n-type to p-type in SnO_2.

G2. Placements

Tyndall National Institute (Cork, Ireland)

Period: 6 months (01/11/2014 – 30/04/2015).
Motivation: Understand the behaviour of graphene from the experiment standpoint.
Work conducted: We carried out the characterization (field-effect measurements, Raman and AFM) of 200 GFETs.